

Integrated Hydrological Model to Evaluate Water Resources of Boteti River sub-Basin, Botswana

WONDIMAGEGN ABEBE DEMISSIE

August 2022

SUPERVISORS:

Dr.Ir. Maciek W. Lubczynski

Dr.Ir. Roelof Rietbroek

ADVISORS:

T. L. MASAHA

M.G. Daoud



Integrated Hydrological Model to Evaluate Water Resources of Boteti River sub-Basin, Botswana

WONDIMAGEGN ABEBE DEMISSIE
Enschede, The Netherlands, July 2022

Thesis submitted to the Faculty of Geo-Information Science and Earth Observation of the University of Twente in partial fulfilment of the requirements for the degree of Master of Science in Geo-information Science and Earth Observation.

Specialization: Water Resource and Environmental Management (WREM)

SUPERVISORS:

Dr. Ir Maciek W. Lubczynski

Dr. Ir Roelof Rietbroek

THESIS ASSESSMENT BOARD:

Dr. Ir Christiaan van der Tol (Chair)

Dr. Jacek Gurwin (External Examiner, University of Wroclaw, Poland)

DISCLAIMER

This document describes work undertaken as part of a programme of study at the Faculty of Geo-Information Science and Earth Observation of the University of Twente. All views and opinions expressed therein remain the sole responsibility of the author, and do not necessarily represent those of the Faculty.

ABSTRACT

The Boteti River sub-Basin (BRB) is located in Botswana's northwest and central districts, spanning 26,204 km². BRB is located in a semi-arid to the arid region, with limited and highly variable rainfall and a high evapotranspiration rate, leading to limited surface water and groundwater resources. The Boteti River (BR) arises from the Okavango Delta overflow and stretches over 300 km to reach Lake Xau (LX). BR is characterized by erratic and unstable flow, which influences the downstream surface water resource (LX) and the groundwater resource. In this study, the basins water resource is quantitatively evaluated by developing an integrated hydrological model (IHM).

A steady state IHM was built for the long-term model period (10 years) starting from 1st October 2010 to 30th September 2020 to assess the water resource of BRB using MODFLOW-6 quantitatively. Three major tasks were set for developing the IHM: 1) developing a hydrogeological conceptual model of BRB for identifying the boundary condition and hydrostratigraphic units of the numerical model; 2) applying remote sensing assessment for preparing an input spatio-temporal input data such as precipitation, interception, potential evaporation, the lake area, volume, elevation and evaporation and 3) calibration of steady-state model using static water level and average stream discharge measurement.

The simulated and observed heads matched pretty well with a numerical error assessment value of 0.995, 0.76 m and 0.96 m for R2, MAE and RSME, respectively. At the same time, the calibrated stream discharge matched 51.2 % of the observed average discharge at Rakops station.

The calibrated model showed that the inflow precipitation (P) represented 69.87% of the total inflow to the system (528.10 mm yr⁻¹), lateral groundwater inflow (Q_{L.in}) 27.68 and stream inflow (q_{in}) 2.45%. Whereas groundwater evapotranspiration (ET_g) took 84.98% of the total outflow from the system (523.31 mm yr⁻¹), lateral groundwater outflow (Q_{L.out}) 12.91%, interception loss (E_I) 1.72% and lake evaporation (E_{LK}) 0.39%.

The calibrated model showed that gross recharge (R_g) represented 67.53% of the total groundwater input (522.64 mm yr⁻¹), lateral groundwater inflow (Q_{L.in}) 27.98%, and stream seepage to groundwater (q_{sg}) 4.20 % and lake (L_{LK.in}) leakage to groundwater 0.29%. Whereas groundwater evapotranspiration (ET_g) took 67.53% of the total groundwater outflow (522.64 mm yr⁻¹), groundwater exfiltration (E_{xf_{gw}}) 23.65%, lateral groundwater outflow (Q_{L.out}) 12.92 % and groundwater leakage to the stream (q_{gs}) 1.99%.

Overall, the simulated steady-state showed a net groundwater recharge of -91.79 mm yr⁻¹, which shows the area's arid climate where the ground evapotranspiration and exfiltration are by far greater than the gross recharge. This is due to annual average precipitation (P) of 369 mm yr⁻¹, which is far lower than the annual potential evapotranspiration rate of 2201 mm yr⁻¹ and annual interception loss of 9 mm yr⁻¹. The model also showed that the leakage from the surface water bodies is greater than the groundwater leakage to surface water bodies. The net leakage between stream and groundwater is +11.63 mm yr⁻¹ (i.e., BR recharge to groundwater), and the net leakage between lake and groundwater is +1.43 mm yr⁻¹ (i.e., LX recharge to groundwater)

Keywords: Boteti River sub-Basin, water resources, lake evaporation, integrated hydrological model

ACKNOWLEDGEMENTS

First and foremost, I would like to praise and thank God, the almighty, who has granted countless blessings, knowledge, and strength to start and accomplish my thesis.

I would like to thank the government of the Netherlands for giving me the Orange Knowledge Program (OKP) scholarship to study for my MSc degree at ITC (University of Twente).

Apart from my effort, the success of this thesis depends largely on the encouragement and guidelines of many others. I take this opportunity to express my gratitude to the people who have been instrumental in the successful completion of this thesis.

I would like to thank Dr. Maciek W.Lubczynski (1st supervisor) for his patience, guidance, encouragement, and advice through research and study time. I am also very thankful to Dr. Roelof Rietbroe (2nd supervisor) for his critical comments and expertise in developing python scripts which ease the data processing phase.

I would like to thank my advisors, Mr Tebogo L.Masaka and Mr Mostafa G.Daoud, for their invaluable discussion and technical support in the data preparation and modelling phase. I would also like to thank the former ITC PhD student Dr Moiteela Lekula, for his discussion during the modelling phase. I am also very grateful to Dr Ben Maathius, Dr Wim Timmemans and Mr Bas Retsios for helping with ILWIS-related coding. And I am very thankful to Mr Aron van Lieshout, the course director of the water resources and environmental management (WREM) department and all the staff members for their support and kindness during my study.

Special thanks to Dr Richard Winston of U.S.G.S for his help in solving the issue related to the ModelMuse while using the LAK package.

Deeply I am thankful for student affairs, Maeir-Chantal Met-Bekkers and Theresa Van den Boogaard for counselling during difficult times. I am very thankful to all my classmates and friends of ITC, especially Salar, Getch, Asrat and Ashu, for always motivating and encouraging me to do this work. I am also thankful to Mr Christiaan Elferink for teaching me the dutch language and culture. I would like to say, “Ik ben zeer vereerd je te kennen”.

Finally, I would like to thank my family, who always pray for me and encourage me to finish my studies.

TABLE OF CONTENTS

1.	Introduction.....	1
1.1.	Background of the study	1
1.2.	Literature review	2
1.2.1.	Review on different methods to study surface water and groundwater interactions.....	2
1.2.2.	Review on IHMs studies for simulation of surface water and groundwater interactions	2
1.2.3.	Previous work in Boteti River sub-Basin	3
1.3.	Problem definition	3
1.4.	Research settings.....	4
1.4.1.	Main objective	4
1.4.2.	Specific objectives	4
1.4.3.	Main research question	4
1.4.4.	Specific research questions	4
1.4.5.	Research hypothesis.....	5
1.4.6.	Research assumptions	5
1.4.7.	Research novelty	5
2.	Study Area.....	6
2.1.	Location of the study area	6
2.2.	Climate of the Boteti River sub-Basin	6
2.3.	Soil and vegetation cover	7
2.4.	Geology	8
2.5.	Hydrology	11
2.6.	Hydrogeology	11
2.7.	Monitoring networks	11
3.	Research Methods.....	14
3.1.	Methodology flowchart	14
3.2.	Data available and its sources.....	15
3.3.	Lake Xau (LX) assessment.....	15
3.3.1.	RS assessment of LX Area-Volume-Elevation (AVE)	15
3.3.2.	Lake evaporation.....	18
3.4.	Conceptual model.....	22
3.4.1.	System boundaries	22
3.4.2.	Defining hydrostratigraphic units.....	22
3.4.3.	Defining flow system pattern, direction, and flow rate	23
3.4.4.	Defining water budget components	24
3.5.	Numerical model	26
3.5.1.	General modelling setup	26
3.5.2.	Model forcing	28
3.5.3.	Effective precipitation (Infiltration rate).....	28
3.5.4.	Potential evapotranspiration	29
3.6.	System parametrization	29
3.6.1.	External boundary conditions.....	30
3.6.2.	Internal boundary conditions.....	31
3.6.3.	State variables	35
3.6.4.	Model calibration	35

3.6.5. Error assessment and sensitivity analysis.....	35
4. Results	36
4.1. Lake assessment result.....	36
4.1.1. RS-based assessment result of LX Area-Volume-Elevation (AVE).....	36
4.1.2. Lake evaporation.....	39
4.2. Conceptual model.....	41
4.2.1. Geological modelling and hydrostratigraphic units.....	41
4.2.2. 3-D hydrostratigraphic model and layer thickness map	43
4.2.3. Boundary condition of Boteti River sub-Basin.....	45
4.3. Numerical model	47
4.3.1. Model forcing.....	47
4.3.2. Steady-state model calibration	51
5. DISCUSSION	63
5.1. Hydrogeological conceptual model.....	63
5.2. Remote sensing contribution to IHM	63
5.3. Water resources in Boteti River sub-Basin	64
6. Conclusion and recommendation.....	66
6.1. Conclusion.....	66
6.2. Recommendations.....	67

LIST OF FIGURES

Figure 2-1 Study area of Boteti River sub-Basin (BRB)	6
Figure 2-2 Daily rainfall and mean air temperature of BRB (Source: http://www.okavangodata.ub.bw/) ...	7
Figure 2-3 LULC map of BRB (source: (Esri ,2020)).....	7
Figure 2-4 Geological map of BRB	8
Figure 2-5 Historical River flow record of BR	11
Figure 2-6 Groundwater potentiometric and flow direction map of BRB, where NFB (no flow boundary); GHB (general head boundary); RCH (recharge boundary); CHD(constant head boundary); and DRN(drain boundary).....	12
Figure 2-7 Location of all available in-situ monitoring network over BRB	13
Figure 2-8 Rainfall data availability in BRB.....	13
Figure 3-1 Methodology flow chart.....	14
Figure 3-2 Lake Xau (LX) location map.....	16
Figure 3-3 Lake Xau a)Before and b) after SLC.....	17
Figure 3-4 Combined DEM and GSW image of LX in November 2012.....	18
Figure 3-5 Temporal variability area of LX obtained from Landsat images.....	19
Figure 3-6 Temporal variability of WST in the middle of LX.....	20
Figure 3-7 Conceptualized Lake interaction with groundwater a) receive groundwater inflow; b) lose water as seepage to groundwater; and c) receive and lose groundwater at the same time d) disconnected lake and groundwater interaction source: (Winter et al., 1998).....	23
Figure 3-8 Conceptualize streamflow and groundwater interaction in BRB; a) gaining; b) losing; c) losing and gaining; d) disconnected losing (Woessner, 2000).....	24
Figure 3-9 Schematization of the system zones and components.....	24
Figure 3-10 Example of quadtree model refinement, source: (Langevin et al., 2022).....	27
Figure 3-11 Daily rainfall at ORC vs uncorrected CHIRPS measurement Source: (Mitiku 2019)	28
Figure 4-1 a) DEM within maximum extent of LX; combined with DEM b) hypsographic curves of cumulative lake volume and lake area versus lake stage.....	36
Figure 4-2 Daily volume variability of LX b) daily surface area variability of LX	37
Figure 4-3 Daily discharge of BR at Rakops station vs daily volume of LX.....	38
Figure 4-4 Lake Xau areal extent over time; November months are compared as these are yearly periods of typical maximum flows.....	38
Figure 4-5 a) Surface area b) water surface temperature (WST) c) net radiation (Rn) d) evaporation rate of LX (E _{L,K}) on November 1st, 2012	39
Figure 4-6 a) Daily WST variability in the middle of LX b) daily temporal variability of LX surface area, of evaporation rate and of volume evaporated water.....	40
Figure 4-7 a) Monthly average of surface area variability b) daily average evaporation rate c) daily average evaporated volume of water.....	40
Figure 4-8 Spatial distribution of boreholes used in Rockworks and location of 5 selected hydrostratigraphic cross-sections in BRB.....	41
Figure 4-9 Hydrostratigraphic cross-sections locations presented in Figure 4-8 over BRB	42
Figure 4-10 3-D-hydrostratigraphic model of BRB	43
Figure 4-11 Hydrostratigraphic unit layer thickness distribution over BRB.....	44
Figure 4-12 Active steady-state model boundary condition of the a) KSU b) SBA and c) LA+EA layer...	45
Figure 4-13 Schematic diagram of the hydrogeological conceptual model and numerical model schematization.....	46

Figure 4-14 Dry and wet average annual interception rate of BRB units(mm yr^{-1}).....47

Figure 4-15 Average daily rainfall of BRB between 2010 to 2020 units (mm yr^{-1}).....48

Figure 4-16 Annual rainfall rate over BRB.....48

Figure 4-18 Annual precipitation(P), interception(E_i), and effective precipitation(P_e) units (mm yr^{-1})49

Figure 4-17 Annual precipitation(P), inteception (E_i) and effecive effective precipitation (P_e) in dry year of 2015 and wet year of 2017 units (mm yr^{-1}).....49

Figure 4-19 Average daily PET from 1st October 2010 to 30th September 2020 units (mm yr^{-1})50

Figure 4-20 Monthly average minimum, maximum and average PET of BRB50

Figure 4-21 Steady state observed vs simulated heads51

Figure 4-22 Residual frequency of observation points on steady-state model.....51

Figure 4-23 Groundwater potentiometric and groundwater table depth map after steady-state model calibration53

Figure 4-24 Horizontal hydraulic conductivity of a) KSU layer, b) SBA layer, and c) LA+EA layer unit (m day^{-1})54

Figure 4-25 Spatially variable maps of a) groundwater recharge (R_g), b) groundwater evapotranspiration (ET_g), and c) groundwater exfiltration (Exf_{gw}) for steady-state IHM in BRB units (mm yr^{-1})56

Figure 4-26 Spatial distribution of net groundwater (R_n) units (mm yr^{-1})57

Figure 4-27 Distribution of lake seepage units (mm day^{-1}).....60

Figure 4-28 Schematic block diagram of water balance exchange between layers within BRB, presented in mm yr^{-1} as 10-year average steady-state IHM presents61

Figure 4-29 Effect of changing K_h on simulated heads62

Figure 4-30 Effect of changing lakebed leakance on simulated heads62

Figure 4-31 Effect of changing streambed K_h on simulated heads.....62

Figure 5-1 Spatial distribution of PET- P map of BRB65

LIST OF TABLES

Table 2-1 Stratigraphy and lithological description of BRB Source: (Carney et al, 1994)	10
Table 2-2 Available groundwater observation sites	12
Table 2-3 Available stream gauges in BR.....	13
Table 3-1 Satellite imagery used for the study	15
Table 3-2 System parametrization of BRB for NPF, where L are literature-based information and S is a spatially variable distribution	30
Table 3-3 Initial parameters for the SFR package	32
Table 3-4 UZF initial parameters	33
Table 4-1 Error assessment of heads after steady-state model calibration in BRB	52
Table 4-2 Calibrated model parameters	55
Table 4-3 Total water balance of BRB at steady-state IHM.....	58
Table 4-4 Water balance of land surface and unsaturated zone.....	58
Table 4-5 Water balance of groundwater (saturated) zone	59
Table 4-6 Water balance of Lake Xau at steady-state IHM.....	59
Table 4-7 KSU aquifer (layer-1) groundwater budget	60
Table 4-8 SBA aquitard (layer-2) groundwater budget.....	61
Table 4-9 LA+EA aquifer (layer-3) groundwater budget	61
Table 4-10 Changing K_h with factor.....	62
Table 4-11 Changing leakance with factor	62
Table 4-12 Changing streambed K_h with factor	62

LIST OF SYMBOLS AND ABBREVIATIONS

1-D	one-dimension
2-D	two-dimension
3-D	three-dimension
α	Solar elevation angle
β	Flow partitioning factor of the MVR package
A_L	area of lake
ALOS PALSAR	Advanced Land Observation Satellite Phased Array L-band Synthetic Aperture Radar
AVE	area, volume and elevation
BGI	Botswana Geoscience Institute
BR	Boteti River
BRA	Boteti River Area
BRB	Boteti River sub-Basin
C	conductance of drain/of general head boundary/of lakebed
CHD	constant head package
CHIRPS	Climate Hazards Infrared Precipitation with Stations
DEM	digital elevation model
d_{ext}	extinction depth
DRN	drain package
DS	Damara Supergroup
d_{surf}	surface depth
DWS	Botswana Department of Water and Sanitation
ε	Brooks-Corey exponent
EA	Ecwa Aquifer
ε_a	apparent atmospheric emissivity
e_a	atmospheric level emissivity
E_l	interception loss
$E_{LK}=E_{24}$	daily evaporated lake water
e_o	surface level emissivity
ET	total evapotranspiration
ET_g	groundwater evapotranspiration
ET_{LD}	land surface evapotranspiration
ET_{ss}	subsurface evapotranspiration
ET_{uz}	unsaturated one evapotranspiration
Exf_{gw}	groundwater exfiltration
Exf_{gw}^s	groundwater exfiltration routed to streams
G	soil heat flux
GA	Ghanzi Aquifer (impermeable layer)
GEE	Google Earth Engine
GHB	general head boundary package
GMS	Groundwater Modeling System
GSFLOW	Groundwater and Surface FLOW
GSW	Global Surface Water
H	sensible heat flux
HCM	Hydrogeological Conceptual Model

h_L	lake stage
H_{obs}	observed heads
H_{sim}	simulated heads
IHM	Integrated Hydrological Model
$K/\Delta x$	leakance
K_h	horizontal hydraulic conductivity
K_{Lb}	hydraulic conductivity of lake bed
KS	Karoo Supergroup
K_{Sb}	streambed hydraulic conductivity
KSU	Kalahari Sand Unit
KW	kinematic wave
LA	Lebung Aquifer
LA+EA	Lebung and Ecca Aquifer
LAK	lake package
L_{hbot}	bottom elevation of the lake
L_{hint}	initial elevation of the lake
L_{htop}	top elevation of the lake
L_{LK}	lake leakage to groundwater/groundwater leakage to lake
L_{LKnet}	net leakage between lake and groundwater
L_N	long wave radiation
$L_{N,24}$	daily longwave radiation
LST	Land Surface Temperature
L_{thk}	lakebed thickness
LULC	land use land cover
LX	Lake Xau
m a.s.l	meters above sea level
m b.g.s	meters below ground surface
Ma	million annum
MAE	mean absolute error
MCM	million cubic meters
ME	mean error
MODFLOW	modular groundwater flow model
MODIS	Moderate Resolution Imaging Spectroradiometer
MVR	water mover package
NFB	no flow boundary
ORC	Okavango Research Center
P	precipitation
P_e	effective precipitation
PET	potential evapotranspiration
θ	volumetric water content
q_B	base flow
Q_{CHD}	groundwater flow across the constant head boundary
Q_{DRN}	groundwater flow across drain boundary
θ_{ext}	extinction water content
Q_{GHB}	lateral groundwater flow across the general head boundary

q_{gs}	groundwater leakage into streams
θ_i	initial water content
q_{in}	stream inflow
Q_L	lateral groundwater flow
q_L	stream outflow (lake inflow)
Q_{RCH}	lateral groundwater Q =constant flow boundary
θ_{resid}	residual water content
θ_{sat}	saturated water content
q_{sg}	streams leakage into groundwater
q_v	vertical groundwater leakage between layers
RCH	recharge package
R_g	gross recharge
RI^s	rejected infiltration to streams
RMSE	root mean square error
R_N	net radiation
R_n	net groundwater recharge
$R_{N,24}$	daily net radiation
ρ_o	surface albedo
$\rho_{o,24}$	daily surface albedo
RS	Remote Sensing
R_{sin}	incoming short wave radiation
σ	Stefan-Boltzmann constant
I_s	gradient of stream
SBA	Stormberg Basalt Aquitard
S_{exo}	exo-atmospheric evaporation
$S_{exo, 24}$	daily exo-atmospheric evaporation
SFR	stream flow routing
SLC	scan line correction
S_N	short wave incoming radiation
$S_{N,24}$	daily shortwave incoming radiation
SREs	Satellite-based Rainfall Estimates
S_{thk}	streambed thickness
S_{top}	streambed top
SW-GW	surface water and groundwater
τ	atmospheric transmissivity
T_0	instantaneous daytime LST
τ_{24}	daily atmospheric transmissivity
T_{max}	maximum day time LST
T_{min}	minimum day time LST
TR	Tamalakane River
U.S.G.S	United State Geological Survey
UZF	unsaturated zone flow
W	stream width
WST	Water Surface Temperature
Δx	distance between lake bottom and centre of overlaying aquifer

λ	latent heat of vaporization
Λ_{24}	daily evaporative fraction index
Λ_i	instantaneous evaporative fraction in

1. INTRODUCTION

1.1. Background of the study

Groundwater and surface water are the primary sources of fresh water supply for different domestic and agricultural uses. Groundwater and surface water resources play an essential role in maintaining a healthy balance in the ecosystem (Yang et al., 2020). Although fresh water is essential for daily human life, its availability is constrained by the supply source, quality, and quantity. As a result, water resource managers are facing such limits while developing management plans and strategies. Many water resource studies show groundwater is a vital and sustainable water supply in many arid and semi-arid regions (Howard et al., 2010), where surface water resources are scarce, and groundwater recharge is possible. This is due to high evaporation and low rainfall rates in such regions, resulting in a scarcity of surface water (Heyns et al., 2009; Roussouw et al., 2018). Despite the importance of groundwater in arid and semi-arid regions, excessive groundwater abstraction can result in aquifer dewatering or irreversible problems such as salinization from seawater and deeper saline water aquifers. Therefore a comprehensive analysis and evaluation of the water resources elements and their interaction are required.

Quantitatively assessing water resource elements (surface water and groundwater (SW-GW)) is a complex physical process (Sophocleous, 2002). The main complexity is behavioural differences in water resource elements. For example, surface water has a relatively high flow speed over time since the flow medium is open, while groundwater flow is slower due to the porous soil medium, which retards its speed. Therefore, it is crucial to consider system behaviour while evaluating water resources. Nowadays, the advancement in hydrological models enables the coupling of water resource elements

The previous traditional water resource modellers focused on stand-alone models, as hydrogeologists focused on groundwater models, which only simulated the saturated zone with externally predefined recharge rates (Winter et al., 1998). Likewise, the surface water modellers mainly focus on quantitatively estimating surface runoff using different models such as HEC-RAS, HSFP, and HBV. However, the previously mentioned modelling methods cannot assess the system's water resources quantitatively. Instead, it assesses groundwater resources and surface water resources individually. Therefore, a more advanced hydrological model is required to assess and quantify the system's water resource components.

Integrated Hydrological Model (IHM) is the most realistic and advanced model for representing and quantitatively assessing the water resource components (Spanoudaki et al., 2009) Since IHMs account for all hydrological components (such as precipitation, recharge, and evapotranspiration) in the surface, unsaturated, and saturated zones to assess and quantify the water resource components (Guerink et al., 2006). A few recent studies by Daoud et al. (2022), El-Zehairy et al. (2018); Hassan et al. (2014); and Lekula and Lubczynski, (2019) showed the application of IHM in quantitatively evaluating the water resources of catchments and basins. As a result, the IHM contribute to a better understanding of the water resources of catchments and basins, thereby improving water resources management.

1.2. Literature review

1.2.1. Review on different methods to study surface water and groundwater interactions

The study of SW-GW interaction can be categorized into three major sections depending on the method used to investigate and characterize the SW-GW interactions (Winter, 1995); (1) analytical, (2) field & chemical, and (3) numerical methods.

- 1) Analytical methods: - According to many oldest literatures analytical methods were used primarily to estimate stream interaction with groundwater by analyzing the 1-D groundwater flow of groundwater to streams (Winter, 1995). The groundwater recharge from streams can be estimated using the hydrograph separation (base-flow characteristic) method as described in Nelms et al. (1995). The issue of groundwater levels fluctuating in tandem with variations in stream flow has also been investigated using the statistical analytic model. (Adamowski and Feluch, 2011; Winter, 1995).
- 2) Field and chemical methods: - This method requires the installation of instruments to monitor the SW-GW interaction. For instance, to identify and quantify the interaction between SW-GW Anibas et al. (2011) employed a “thermal method”, which uses field-based temperature measurements. As a result, the “thermal method” was able to estimate the flux exchange between SW-GW in summer and winter. However, the method limits estimating the fluxes during season transition periods such as autumn and spring. Different organic chemistry researchers used the chemical method to assess the quality and quantity of the SW-GW interactions using isotopes. For example, Modie et al. (2022) used natural stable isotopes to trace the infiltration of stream water into the surrounding groundwater.
- 3) Numerical methods: - Since the middle of the 1960s, numerical modelling has been the main method for analyzing how groundwater and surface water interact. Most numerical models still use the simple Darcy formula, the relationship between hydraulic conductivity, hydraulic gradient, and cross-sectional area is what determines discharge. The numerical model determines how much water seeps through stream sediments based on the head difference between surface water, groundwater, and stream cross-section (Winter, 1995). Recently, after the development of the powerful SW-GW simulation module MODFLOW (modular groundwater flow model) by McDonald and Harbaugh (1988), many researchers used the MODFLOW code to develop a numerical model which quantifies the interaction between SW-GW as well as the solute transport modelling. For example, El-Zehairy et al. (2018) developed an IHM that simulates the interaction between surface water (lake and stream) and groundwater using MODFLOW NWT. As a result, the numerical model produced a realistic estimation of SW-GW interaction in transient state numerical model conditions.

1.2.2. Review on IHMs studies for simulation of surface water and groundwater interactions

Hydrological system components of the arid and semi-arid regions are highly dependent on the interaction between SW-GW (Hassan et al., 2014; Newman et al., 2006). However, IHMs are essential for understanding the exchange of water between the SW-GW components, which helps to address the crucial difficulties in water resource management (Newman et al., 2006).

Previously numerous IHM studies were developed to simulate SW-GW interactions on catchment and basin scales. For instance, Hassan et al. (2014) used GSFLOW (Groundwater and surface FLOW) with a kinematic wave (KW) approximation (i.e., neglecting the negative potential gradient flow) to model the SW-GW interaction dynamic in hard rocks system (HRSs), focusing on the stream drainage beds. As a result, a

long-term IHMs was developed, which enables the quantification of the hydrological components in the study area, especially the use of GSFLOW enables the simulation of groundwater exfiltration better than the earlier version of MODFLOW (MODFLOW 2005)

In the same study area as Hassan et al. (2014), the recent study by Daoud et al. (2022) also used MODFLOW-6 (Langevin et al., 2022) to simulate SW-GW interaction with an emphasis on applying cascade routing and infiltration concept to improve the stream flow simulation and the overall water balance of the study area. With the help of developed IHM, it was possible to quantify hydrological components of the study area. In particular, the cascade routing and infiltration concept reshaped the water balance equation as well as improved the water balance result.

This study will also use the latest MODFLOW 6 code to assess and quantify the water resources of BRB by developing representative IHM for the study area.

1.2.3. Previous work in Boteti River sub-Basin

Previously, a few studies have been conducted in the study area and surrounding areas, focusing on groundwater flow modelling, groundwater resource investigation, and surface groundwater interaction. For example, airborne electromagnetic modelling of an aquifer in the Boteti River area (BRA) by Sattel and Kgotlhang (2003) investigated and mapped the possible freshwater locations with the respective lithologies and structures containing fresh water in BRA. As a result of the investigation, fresh water in BRA was found in shallow Kalahari beds following the BR alluvium deposit. Moreover, the study has identified subsurface lithological units, hydrogeological properties, as well as geophysical properties of BRA.

The recent study by Lekula and Lubczynski (2019) modelled the surface- groundwater flow of the Central Kalahari Basin (i.e., the western side of the study area) by coupling the long-term remote sensing data with in-situ measurements using an IHM numerical modelling approach. The numerical model consists of six-layered hydrostratigraphic units distributed across the study area. The model result showed that groundwater is found in all hydrostratigraphic units except the Stormberg basalt aquitard layer, which has very high resistivity, low yield, and low hydraulic conductivity. The model also shows that for the modelling period of 2002–2014, subsurface evaporation had a higher impact on gross recharge than groundwater recharge. The yearly gross median groundwater recharge over the study was -1.5 mm yr^{-1} .

Mitiku (2019) studied the BRA SW-GW interaction using IHM, focusing on the BR interaction with groundwater. The study used a one-layer hydrostratigraphic unit of the Kalahari aquifer as a focus to model the transient state numerical model for a model period from 2014 to 2017. The model result showed that the net groundwater recharge was -100 mm yr^{-1} in the dry year of 2016 and 130 mm yr^{-1} in the wet year of 2017.

1.3. Problem definition

The study area of Boteti River sub-Basin (BRB) shown in Figure 2-1 is characterized by the presence of surface water and groundwater resources. The Boteti River (BR) is the main surface water resource in the study area, serving as a recharge source for the groundwater and an inflow source for the Lake Xau (LX), located downstream of the BR. However, the amount of groundwater resource is highly affected by the amount of surface water bodies (i.e., BR and LX), thereby affecting the groundwater replenishment by influencing the amount of groundwater recharge. As a result, research focusing on the basin's water resources using IHM is imperative to assess and quantify the amount of exchange between surface water and groundwater. Nevertheless, such studies are limited in the study area.

A few studies, such as Mitiku (2019), highlight the importance of IHM in quantifying the flux exchange between surface water and groundwater, focusing on the BR area (BRA). The study demonstrates that the net average groundwater discharge to the BR during the dry year of 2016 was 14.55 mm yr⁻¹ and the wet year of 2017 was 14.84 mm yr⁻¹. However, this study hypothesised that the surface water discharge to groundwater exceeds the aquifer discharging to the river. The study report shows that running a representative IHMs model is difficult due to a constraint in ground-based measurements (i.e., rainfall, stream flow, weather data, and groundwater level records). Furthermore, due to oversimplification, the study's conceptual model did not completely describe the hydrogeological setting of the area. As a result, the resultant numerical model was unsatisfactory.

Moreover, none of the previous studies has investigated the impact of BR flow on the LX volume, area, and level fluctuations over time or the lake's interaction with groundwater. Therefore, this study will use IHMs to assess the water resources of BRB. However, there are challenges to developing IHM in BRB, and the following are the primary ones.

- 1) Finding a spatio-temporal climatic monitoring system is challenging for developing a representative IHM for BRB. The BRB has a limited rainfall station within the study area and no weather station for measuring the meteorological variables for calculating the area's potential evapotranspiration (PET). Only the neighbouring weather stations are available for comparison. Therefore, this study will use open-source remote sensing products as an input for IHM to produce an IHMs of BRB.
- 2) Limited knowledge of the conceptual hydrological model of the BRB: - Previous conceptual model studies do not fully cover the BRB. They are limited to specific study areas (Lekula et al., 2018; Linn et al., 2003; Sattel and Kgotlhang, 2003; VanderPost and McFarlane, 2007). Therefore, developing a full representative conceptual model will give a clear description of the model setup.
- 3) A lack of modelling over BRB based on long-term data:- long-term data-based modelling is required to identify the surface water resource's effect on BRB groundwater. However, the previous studies on the area mainly focused on groundwater resource investigations (Rahm et al., 2006; VanderPost and McFarlane, 2007; Water Surveys Botswana (Pty) Ltd, 2006) and modelled for a shorter period Mitiku (2019) also developed a three-year transient SW-GW interaction model.

1.4. Research settings

1.4.1. Main objective

This research's main objective is to evaluate BRB's water resources quantitatively.

1.4.2. Specific objectives

- ❖ Make a quantitative assessment of the temporal LX variability of the: i) stages; ii) area extent; iii) volume.
- ❖ Develop and calibrate the integrated hydrological model of the BRB.
- ❖ Define the water balance of the BRB.

1.4.3. Main research question

What effect do surface water resources (i.e., BR and LX) have on BRB groundwater resources?

1.4.4. Specific research questions

- ❖ What is the relation between BR flow and seasonal changes of LX stages, area extent and volume?

- ❖ Which conceptual and numerical model setup can most realistically simulate the water resources of BRB?
- ❖ What are the main hydrological components of BRB water balance?

1.4.5. Research hypothesis

- ❖ The recharge of the surface water bodies to groundwater is greater than groundwater discharge to surface water bodies.
- ❖ The maximum LX stage (so also area extent and volume) occurs during the high flooding seasons of BR.
- ❖ Evapotranspiration has a large impact on the dryness of LX.

1.4.6. Research assumptions

- ❖ The leakage into the bottom aquifer (Ghanzi aquifer) has a negligible impact on the flux exchange between the surface water and the upper modelling aquifers. This study considers the Ghanzi a model bottom boundary (impermeable layer).
- ❖ The surface water use and groundwater abstraction have negligible impacts on the surface and groundwater interactions.
- ❖ The surface water of BR and LX are hydraulically connected with groundwater.

1.4.7. Research novelty

This study's novelty is that remote sensing (RS) will be used as input data for the first time to assess and quantify the interaction of LX with surrounding groundwater. Moreover, this study will be the first to develop a conceptual hydrostratigraphic model of BRB by investigating the available boreholes in the study area, enabling users to develop a realistic groundwater numerical model over BRB.

2. STUDY AREA

2.1. Location of the study area

The BRB study area is located in Botswana's northwest and central districts, spanning 26,204 km². The BRB is part of the Okavango River Basin located southeast of the Okavango Delta at geographical coordinates of 19°30' to 21°30' south and 23°00' to 25°00' east. The study area is a relatively flat terrain with an elevation range between 1023 m a.s.l in the northwest to 898 m a.s.l in the southeast. The BR is the main surface water source of the BRB, beginning at the Thamalakane River (TR), the outflow river from the Okavango Delta. The BR travels southeast to reach LX by stretching around 300 km.

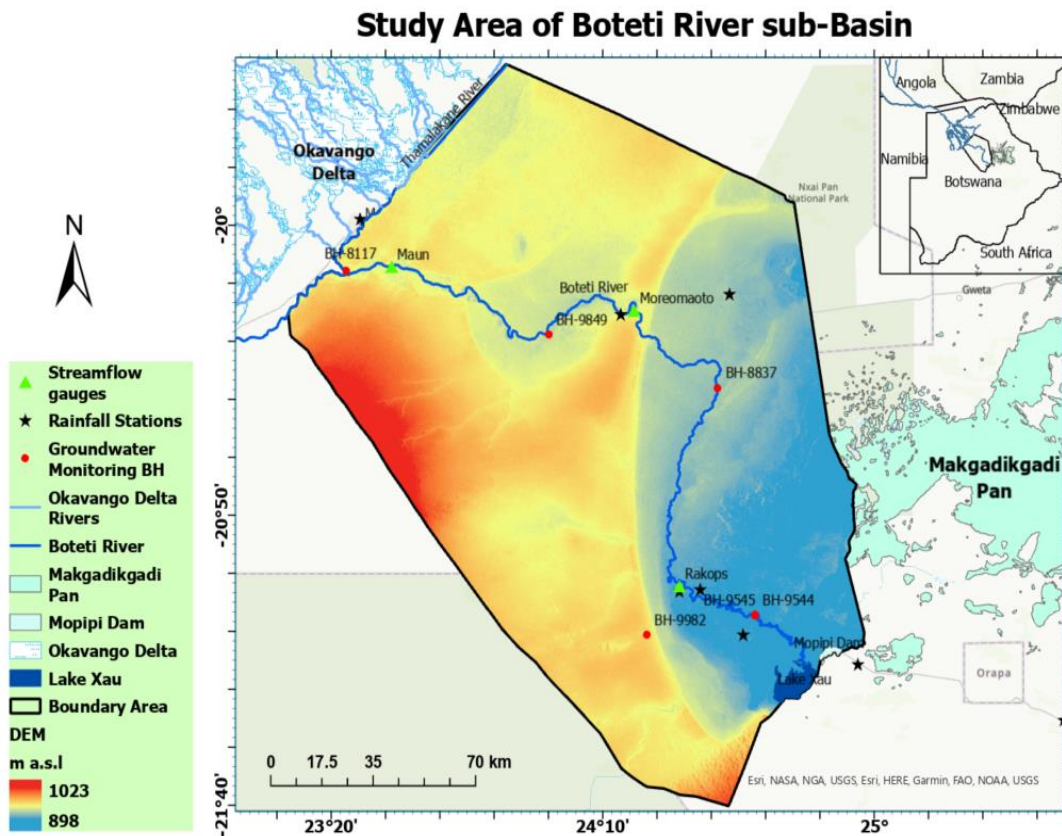


Figure 2-1 Study area of Boteti River sub-Basin (BRB)

2.2. Climate of the Boteti River sub-Basin

The climate in the study area is semi-arid, characterized by highly variable and limited rainfall and a high evapotranspiration rate. The average annual rainfall of the study area ranges between 350-450 mm yr⁻¹ (Swatuk and Motsholapheko, 2008). The highest evapotranspiration rate in the region accounts for 85-90% of all the rainfall, either due to direct evaporation or through transpiration (Mphinyane et al., 2018; Swatuk and Motsholapheko, 2008; Vanderpost, 1995). The temperature in the study area ranges between 35 °C in the summer and 10 °C in the winter, as shown in Figure 2-2 below.

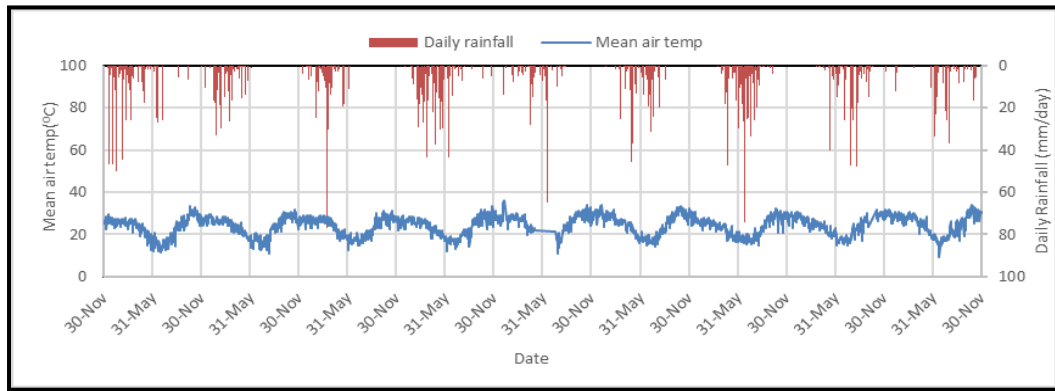


Figure 2-2 Daily rainfall and mean air temperature of BRB (Source: <http://www.okavangodata.ub.bw/>)

2.3. Soil and vegetation cover

The previous studies by De Wit and Nachtergaele (1990) and Carney et al. (1994) indicate that the study area's principal soil types consist of arenosols away from the BR and fluvisols alongside the BR. The arenosols are deep sandy soils characterized by low organic matter concentration and poor fertility due to a paucity of clay (Swatuk and Motsholapheko, 2008). As a result, arenosols are not suitable for farming. In contrast, fluvisols are favourable for aerated agricultural use because of their high-water holding capacity characteristics (Breyer, 1983; Nicholson and Farrar, 1994).

Bare pan surfaces cover the study area with small vegetation covers of naturally occurring savannah grassland, small trees (shrubs), and open grasslands with a riverine acacia tree along the belt of BR (Weare and Yalala, 1971). The current land use land cover (LULC) map with 10 m resolution from Esri shown below also suggests that a large part of the study area is covered with shrubs and small trees (Esri, 2020).

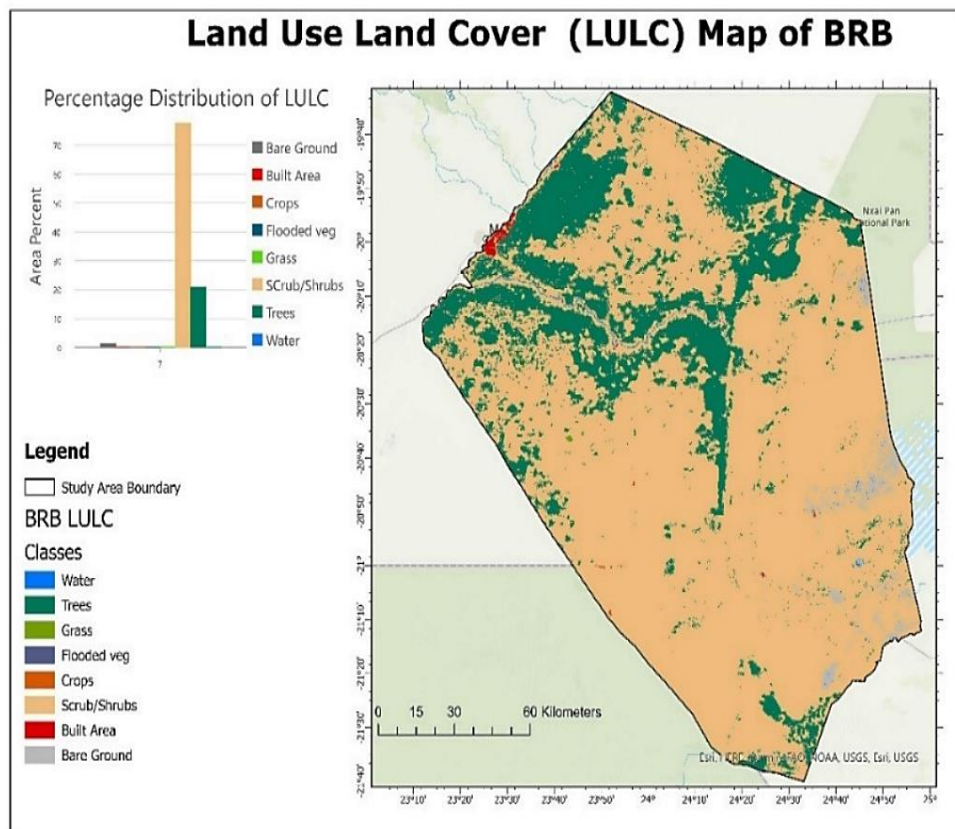


Figure 2-3 LULC map of BRB (source: (Esri ,2020))

2.4. Geology

The geology of the study area is characterized by thick layered Kalahari Group sediments (post-Karoo) overlying the Karoo Supergroup (KS) and Damara Supergroup (DS) (Sattel and Kgotlhang, 2003), as shown in Figure 2-4. The KS consists of Stormberg Lava, Lebung, and Ecca Groups. The DS underlies the KS and includes the Ghanzi Group meta-sediments. Some parts of the area lie above the Pre-Karoo Archaean basement rocks. Figure 2-4 shows the Pre-Kalahari geology and the Kalahari sediment thickness distribution across the BRB.

The earlier geological study of Botswana by Carney et al. (1994) refined the lithological studies of Smith (1984) to produce a stratigraphic geological sequence of Botswana.

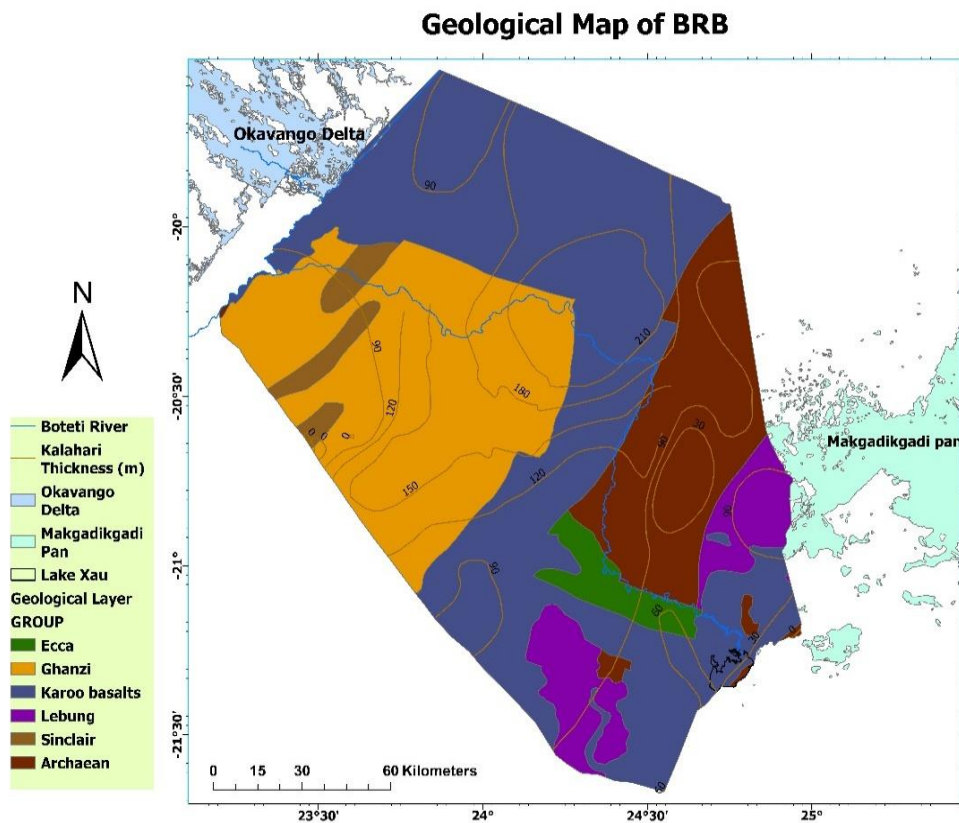


Figure 2-4 Geological map of BRB

Kalahari Group (Kalahari Sand)

Throughout the study area, the Kalahari Group almost obscured all the underlying Karoo and pre-Karoo bedrocks with variable thicknesses ranging from 2 to more than 200 m, as indicated in the Kalahari thickness contour in Figure 2-4. The Kalahari Group mainly comprises aeolian (alluvial) sediment far away from the riverside and fluvisol (lacustrine) sediments along the side of BR (Carney et al., 1994).

Stormberg Lava Group

This group forms the uppermost volcanic Basalt Lava sheets & intrusive (Doleritic dykes and sills) of the Kalahari Karoo supergroup. It consists of tholeiitic continental basalt with an extensive thickness of > 100 m, as indicated in the neighbouring study of Lekula et al. (2018).

Lebung Group

This group lies within the Beaufort Group, consisting of a two-unit formation of the Mosolotsane formation and Ntane Sandstone formation. The Mosolotsane formation comprised the red-brown colour of sandstone, mudstone, and siltstone. The Ntane sandstone formation comprises aeolian members overlaying the fluvial members. The Fluvial member is characterized by coarse-grained, gritty cross-bedded sandstone coloured white to cream-brown. On the other hand, the aeolian member is characterized by uniform, rounded grains coloured orange to pink.

Ecca Group

The Ecca Group is classified into two units based on formation, Thaliana and Mae Arkose formations. The Thlapanana formation comprises dark grey carbonaceous mudstones and coal. In contrast, the Mae Arkose formation comprises fluvio-deltaic white-pinkish sandstones and siltstone.

Ghanzi Group

The Ghanzi Group unconformably has sedimentary and volcanic rock types under the Kalahari sand. It is mainly found in the highly elevated northwest corner of the study area. The formation of the Ghanzi group is subdivided into three-unit members: Ngwango (purple arkosic mudstone), D'ka (green arkosic sandstone, siltstone, and mudstone), and Mamuno (purple red arkosic sandstone, limestone, and siltstone).

Sinclair Group

This group is a volcano-sediment of the Kgwebe formation found below the Ghanzi groups in the northwest part of the study area.

Molopo Farms Complex

The Molopo Farms Complex is mainly found in the fold basin. The rocks include various intrusive rocks such as gabbro and gabbro-norite.

Pre-Karoo (Archean Basement)

The information about this borehole in the study area is limited due to the limited borehole depth. The rocks are of the Proterozoic age, mainly gneisses of granitic and granodioritic composition.

Table 2-1 Stratigraphy and lithological description of BRB Source: (Carney et al, 1994))

AGE	STRATIGRAPHIC UNIT			LITHOLOGICAL DESCRIPTION
	Supergroup	Group	Formation	
Tertiary to Recent (0-65Ma)	Kalahari Beds	Kalahari	Upper	Alluvial sediments, aeolian sands, calcrete & silcrete
			Middle	Green or pink silcrete, friable sandstone, siltstone & clay
			Lower	Dark green, highly calcareous quartzose siltstones & conglomerate
Late Carboniferous to Early Jurassic (180-300Ma)	Karoo	Stormberg Lava		Basalt lava sheets & intrusive (dolerite dykes and sills)
		Lebung	Ntane Sandstone	A fine red and pink sandstone, grey green when reduced
			Mosolotsane	Sandstones, usually red (Mosu Sandstone, upper member). Siltstones & mudstones (red to black, lower member). Northern Belt of Central The Karoo.
		Beaufort	Ngwasha and Pandamatenga	Sandstones, siltstones, and mudstones, grey to green. Northeast Karoo
		Ecca	Thlapana	Dark grey carbonaceous mudstones & coal
			Mea Arkose	Fluvio-deltaic white-pinkish sandstone and siltstone
Late Proterozoic 300 - 415 Ma	Damara	Ghanzi	Ngwango	Purple arkosic mudstone
			D'kar	Green arkosic sandstone, siltstone & mudstone
			Mamuno	Purple red arkosic sandstone, limestone & siltstone
		Sinclair	Kgwebe	Grey, green, and pink volcano-sediments
Early Proterozoic 415 - 570 Ma		Molopo Farms Complex		Basic and ultra-basic intrusive
Archaean Basement				Unexposed metamorphosed rocks of uncertain lithology.

2.5. Hydrology

BR is the primary surface water source for society's livelihood in the study area. Previous research, however, classified BR flow as non-perennial due to erratic and unreliable flow from 1990 to 2009 (Sebego et al., 2017; VanderPost and McFarlane, 2007). However, after 2009, due to the high rainfall upstream of BR, the river became a perennial river, reaching up to LX. Figure 2-5 below shows the historical river flow record at Samedupe upstream and Rakops downstream of gauge stations.

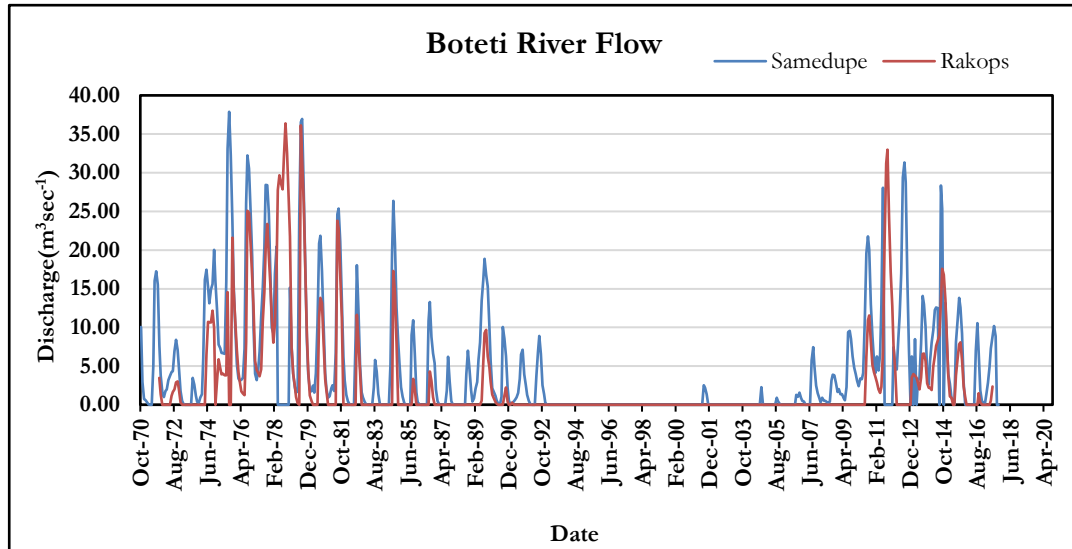


Figure 2-5 Historical River flow record of BR

2.6. Hydrogeology

The groundwater in the BRB is found in all stratigraphic units. However, the distribution amount and groundwater quality are highly variable (Water Surveys Botswana (Pty) Ltd, 2006). There are two main groundwater inflows to BRB. The primary ones come from the northwest side of the study area, following the BR. Previous studies by McCarthy (2006) suggested a possible unknown amount of groundwater outflow through 'Thamalakane faults' fracture parallel to BR flow. The second inflow comes from the western side. It flows to the eastern side of the study area following elevation terrain (i.e., from the higher elevation in the west to the low areas of the Makgadikgadi Pans in the east) (Lekula and Lubczynski, 2019). In this study, the potentiometric map in Figure 2-6 is created to show the regional groundwater flow of the BRB using the Monitoring networks

2.7. Monitoring networks

In the BRB, the monitoring network was set up for monitoring the groundwater level, meteorological data, and stream discharge, as shown in Figure 2-7. There are six daily groundwater level observation loggers (BH-8117, BH-9849, BH9982, BH-8837, BH-9544, and BH9545) were used as groundwater level control points while developing the IHM model. The data availability and the measuring device type are described in Table 2-2. There are also 11 rainfall gauging stations with different recording periods. However, the rainfall stations are compared with satellite products since the stations have a data gap, as shown in Figure 2-8. Two stream measurement gauges are located in BR. The first is in Samedupe (Maun Bridge) station, and the second is in Rakops station, 50 km before the LX. The recording length and type are shown in Table 2-3 below.

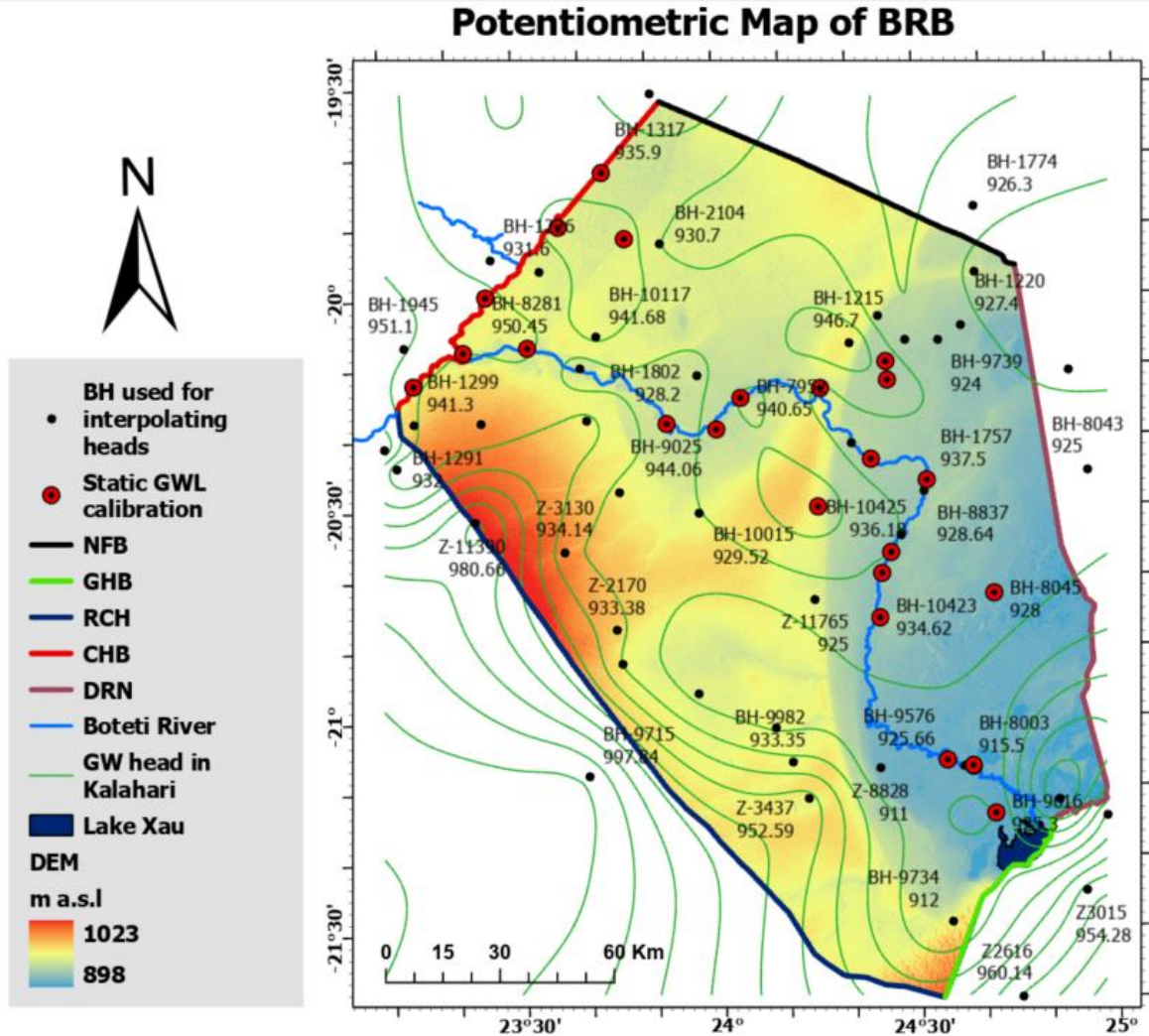


Figure 2-6 Groundwater potentiometric and flow direction map of BRB, where NFB (no flow boundary); GHB (general head boundary); RCH (recharge boundary); CHD(constant head boundary); and DRN(drain boundary)

Table 2-2 Available groundwater observation sites

ID-number	location	Lat	Long	Recording period	Time step	Type
BH8117	Thamalakane	-20.128	23.377	30/09/2018 to 01/03/2021	daily	New with logger
BH8837	Khumaga	-20.446	24.517	1/10/2018 and 25/01/2019	two days	Single time record
BH9544	Toromoja	-21.119	24.632	1/10/2018 to 24/01/2019	daily	New with logger
BH9545	Toromoja	-21.118	24.631	1/10/2018 to 13/12/2018	daily	New with logger
BH9849	Mkalamabedi	-20.312	23.998	3/10/2018 and 29/01/2019	two days	Single time record
BH9982	Garube	-21.176	24.299	1/10/2018 to 26/01/2019	daily	New with logger

3. RESEARCH METHODS

3.1. Methodology flowchart

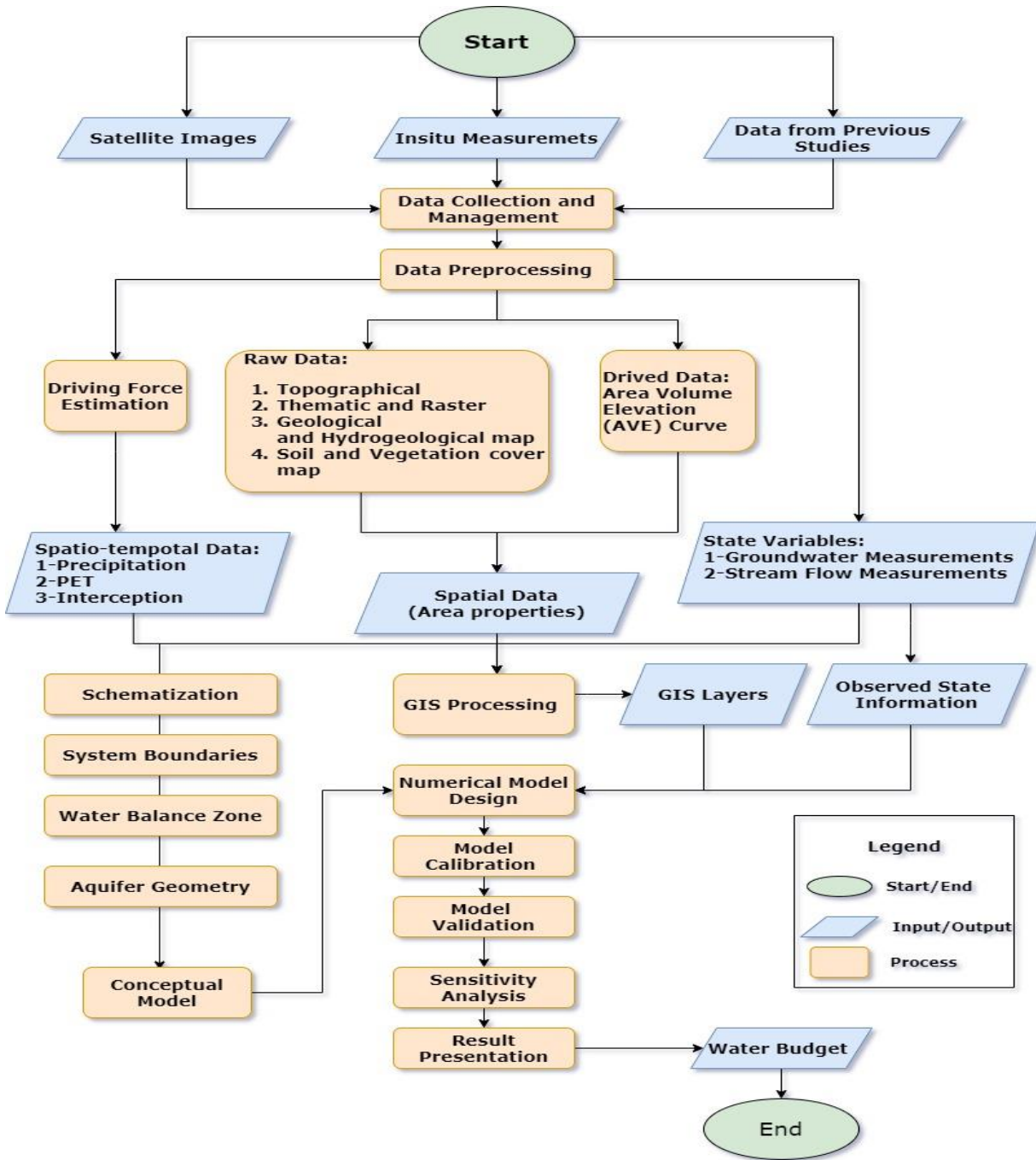


Figure 3-1 Methodology flow chart

3.2. Data available and its sources

For this study, three primary input data sources were used as indicated in the flow chart (in-situ measurements, satellite images, and data from the previous studies in the BRB area).

- I. In-situ measurements: - the daily groundwater level measurements were used for the model calibration. The data from the meteorological station were compared to the data from satellite images. The borehole data was also used to develop the conceptual hydrological model of BRB.
- II. Satellite imagery: - this study used mainly remote sensing (RS) products for different purposes
 - ❖ To derive the area volume and elevation (AVE) relationship curve for LX.
 - ❖ To obtain spatio-temporal variability of driving forces such as rainfall, interception, potential evaporation (PET), and lake evaporation.
- III. A previous study in BRB: - the previous study results in the study area will be used as reference data for developing the IHM of BRB.

Table 3-1 Satellite imagery used for the study

Satellite images	Retrieved Period	Purpose	Source
Landsat 5,7 and 8	1 st October 2010 to 30 th September 2020	AVE curve of LX	https://earthexplorer.usgs.gov/
CHIRPS	1 st October 2010 to 30 th September 2020	Daily Spatio-temporal rainfall	https://www.chc.ucsb.edu/data/chirps
MOD16A2 V006 8-day PET	1 st October 2010 to 30 th September 2020	Daily Spatio-temporal PET	https://appears.earthdatacloud.nasa.gov/
WaPOR Interception (Decadal)	1 st October 2010 to 30 th September 2020	Daily Spatio-temporal Interception	https://wapor.apps.fao.org/
MOD11A1 V006 Daily LST	1 st October 2010 to 30 th September 2020	Daily LX evaporation rate	https://appears.earthdatacloud.nasa.gov/

3.3. Lake Xau (LX) assessment

The lake assessment was done mainly for two reasons 1) to prepare input data for the IHM so that there will be a reliable estimate of water balance for the IHM and 2) to retrieve the long-term history of the lake, which shows the temporal variability of the lake volume, elevation and area.

3.3.1. RS assessment of LX Area-Volume-Elevation (AVE)

Stagnant water bodies such as lakes, reservoirs, and ponds play an important role in providing a sufficient water supply for the water-scarce area. However, the difficulties in measuring the physical properties of these water bodies lead to complex water resource management. A particular estimation mechanism, such as the Area-Volume-Elevation (AVE) curve, provides vital information to monitor the storage variation in lakes and reservoirs using satellite imageries (El-Zehairy et al., 2018; Li et al., 2021).

Generally, the AVE curves provide the storage capacity (volume) and areal extent variability with respect to the stage variability of the acquired stagnant water body. Many studies have developed different approaches to generate AVE curves of lakes and reservoirs. The most popular AVE curves are surveys, simulations, and remote sensing-based methods. However, remote sensing-based technologies are a frequently utilized method (Li et al., 2021; Yue and Liu, 2019). Since the essential input (i.e., remote sensing (RS) optical imageries and digital elevation models (DEM)) data are open-source data.

Previous studies have utilized the RS-based method to monitor the lakes and reservoir changes over time. For example, Gao et al. (2012) used MODIS images with radar altimetry observations, and Li et al. (2019) used Landsat images with lidar tracks to estimate the AVE curve. Similarly, Li et al. (2021) and Yue and Liu (2019) used DEM to obtain elevation and area information to develop the AVE curve of lakes and reservoirs. In this study, the RS-based technologies will be utilized to develop the spatio-temporal AVE curve for LX from 1st October 2010 to 30th September 2020.

Lake Xau (LX) is a non-permanent lake in the BRB terminal. In the 1970s, the BR was diverted to bypass LX to bring water to Mopipi Dam (Figure 3-2), located 8 km in LX's northeast direction, as shown in Figure 3-2. However, in late 2000, the diversion structure was removed, and subsequently, due to high rainfall upstream of BR in 2009, the BR started to reach LX at the end of 2010 (Sebego et al., 2017). According to Global Surface Water (GSW), the maximum estimated extent of LX is ~ 100 km² with an elevation range of 913 to 934 m a.s.l. The geological and soil map of the study area suggested that the lake overlays above the Kalahari sand and Karoo basalt, as shown in Figure 2-4. The Kedia and Mopipi station (Figure 3-2) records indicate that the area has an average rainfall of 190 mm yr⁻¹ and a temperature range of 20 to 35 °C.

The GSW provides the maximum water extent and the monthly surface water record based on the long-term Landsat 5, 7, and 8 measurements from 1984 to 2021. For LX, the monthly historical record is acquired by modifying the code provided by Pekel et al. (2016) on the Google Earth Engine (GEE) code editor tool, as shown in Appendix-1.

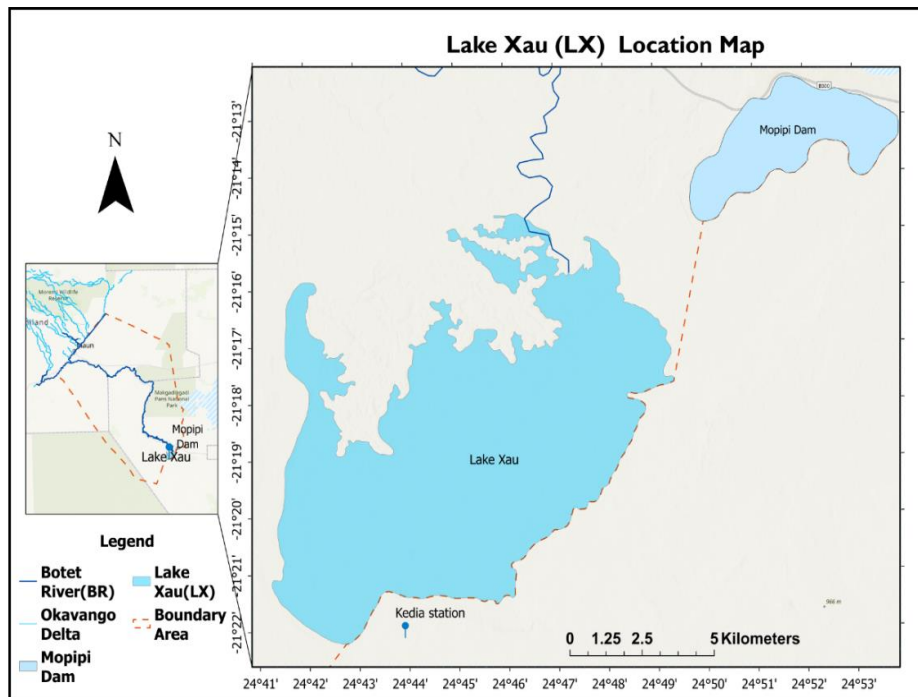


Figure 3-2 Lake Xau (LX) location map

Considering the LX-DEM, the ALOS PALSAR (Advanced Land Observation Satellite Phased Array L-band Synthetic Aperture Radar) provided a 12.5 m spatial resolution DEM from 2006 to 2011. The data can be obtained from <https://search.asf.alaska.edu/>.

The RS-based AVE curve method is composed of two main steps.

Step 1: - Data pre-processing: - in this step, the obtained dataset was pre-processed to attain the input data for the python script. The main tasks are described as follows: -

- I. Scan-Line Correction (SLC): - According to Scaramuzza et al. (2019), the Landsat 7 ETM+ loses approximately 22% of its image data due to scan line error. In this study, SLC is required to fill in the missing data using the Landsat Toolbox. This process is performed for all Landsat 7 ETM+ based GSW products with scan line errors. Below is a selected month (November 2012) before and after SLC.

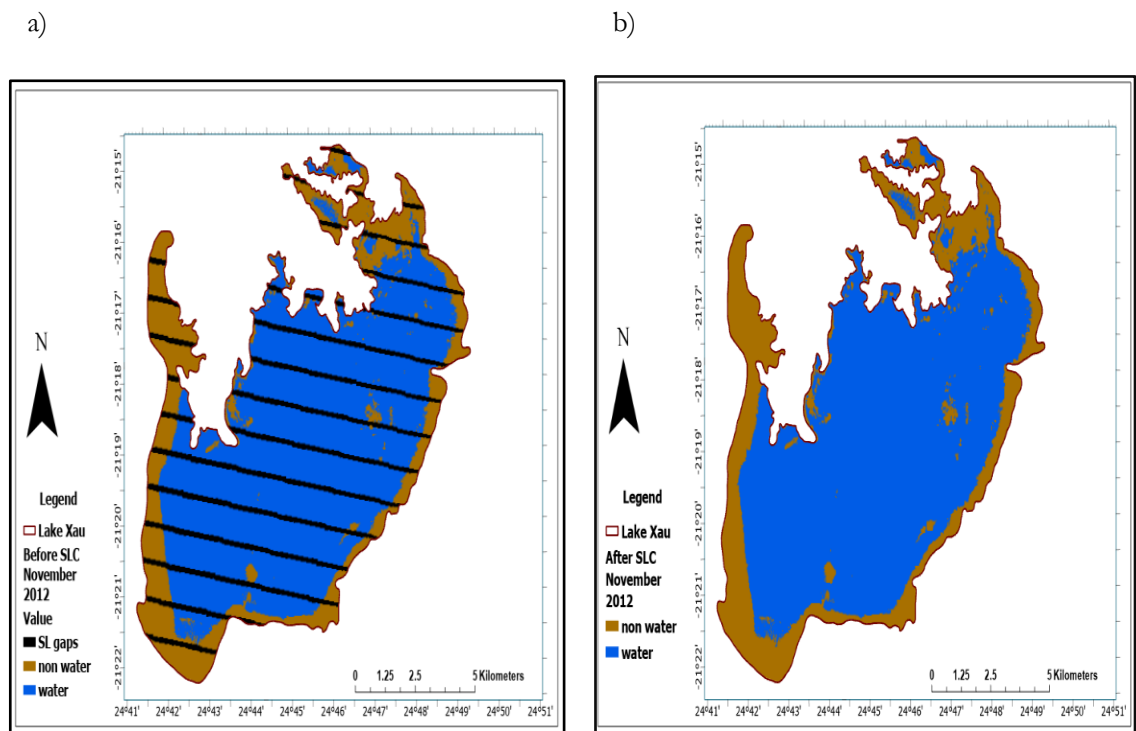


Figure 3-3 Lake Xau a)Before and b) after SLC

- II. Combining the GSW with ALOS PALSAR DEM: - At this point, ALOS PALSAR DEM was merged with 120 monthly water extent images of LX to prepare input data for the python script, which contains dual information of the monthly area and the respective elevation of the lake. The entire procedure was carried out using the model builder tool in the ESRI ArcGIS Pro software, which speeds up processing. Figure 3-4 shows LX's combined GSW and DEM for the selected month (November 2012).

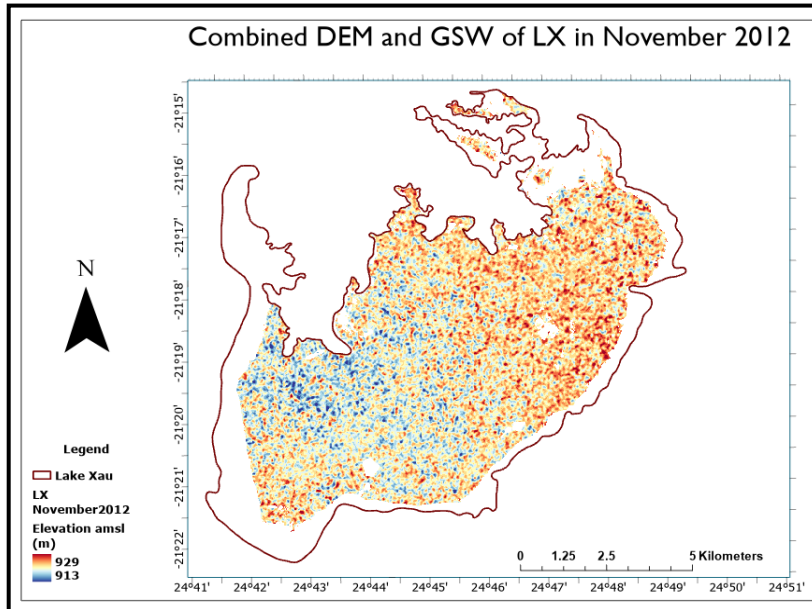


Figure 3-4 Combined DEM and GSW image of LX in November 2012

Step 2: - Estimating volume using python

A python script was used to convert the combined GSW and DEM products into an AVE curve using pixel-based volume calculation following the Li et al. (2021) approach. The following equation was used by Li et al. (2021) to calculate the cumulative volume storage related to DEM.

$$V_n = \sum_{i=1}^{n-1} \frac{(h_{i+1} - h_i)(A_{i+1} + A_i)}{2} \quad \text{Equation 3-1}$$

where A_i is the complete water surface area covered by the i^{th} elevation, which corresponds to the elevation height of h_i , and n is the number of elevation range gaps, the maximum in this study is 16 m (i.e., 929-913). Thus, the volume for each elevation was obtained. Therefore, the above equation will be calculated using the python script provided in Appendix-2.

3.3.2. Lake evaporation

In arid and semi-arid countries such as Botswana, evaporation is one of the major components of the water cycle since the potential evaporation rate is higher than the rainfall rate (Farquharson et al., 1990). Quantification of evaporation rate from open water bodies such as lakes and reservoirs are relatively challenging and complex due to the paucity of in-situ measurement (Mokgedi et al., 2019). Many previous global studies followed different approaches to estimate the evaporation rate from open water bodies by using direct measurement, assumptions, and mathematical equations (Bastiaanssen et al., 2005; Mokgedi et al., 2019). However, most of the direct assumption and mathematical methods, such as the Penman method (Penman, 1948), Simplified Penman method (Villa Nova et al., 2006), and Bowen-ratio method (Todd et al., 2000), require many inputs of in-situ measurements. After the development of satellite missions, different remote sensing (RS) based approaches have been developed through time to estimate the evaporation rate in the data-scarce area such as SEBAL (Bastiaanssen et al., 1998), SSEBS (Senay et al., 2007), and DATTUTDUT (Timmermans et al., 2016).

This study quantified the LX evaporation using a remote sensing-based approach called DATTUTDUT (Deriving Atmosphere Turbulent Transport Useful To Dummies Using Temperature). The DATTUTDUT

is a simple RS-based model for monitoring the evaporation rate of water from the earth's surface (Timmermans et al., 2016). The DATTUTDUT model was selected for this study because the study area has no in-situ measurements for obtaining the daily evaporation rate of the lake. Therefore, the DATTUDUT model can be utilized to quantify the daily evaporation rate of the lake by using land surface temperature (LST) products such as MODIS and Landsat thermal images.

MODIS is a satellite sensor instrument that provides vital information about global dynamics on the earth's surface and surroundings. The MOD11A1 version 6 provides the daily LST and emissivity data with a 1 km spatial resolution (Wan, 2013).

There are three main stages for estimating the daily evaporated volume of LX

I. Data collection for volumetric evaporation calculation

The primary input datasets for calculating LX's temporally variable volumetric evaporation are MOD11-A1 daytime LST and temporally variable lake extent. The daily daytime MOD11-A1 LST can be obtained from <https://appears.earthdatacloud.nasa.gov/> with a spatial resolution of 1 km. Figure 3-5 provides the temporal variability of the areal extent of the lake, which can be used to extract the lake's water surface temperature (WST) from MOD11A1 LST. The WST is a MODIS LST over a water body (Zhao et al., 2020).

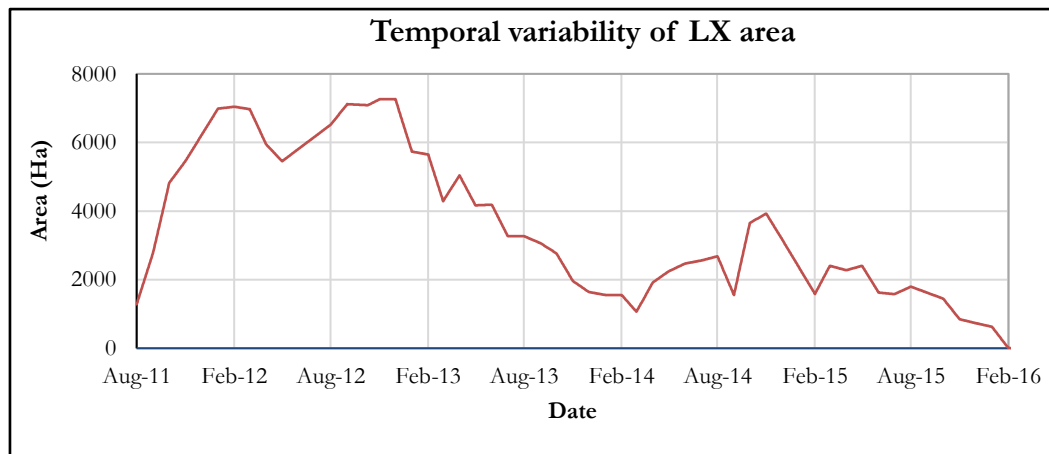


Figure 3-5 Temporal variability area of LX obtained from Landsat images

II. Calculating evaporation of LX rate time series using the DATTUDAT model

This stage has two main primary steps

Step 1: - Scaling and quality assessment of MOD11-A1 daily WST product

In this step, the retrieved daily WST will be rescaled with a scale factor of 0.02 to convert it to a daily WST raster image (K). The quality assessment report for MOD11-A1 will be used to filter cloud-covered images from non-cloud-covered WST images. In this study, good data quality images (average LST error of $\leq 3K$) were taken for the analysis. Figure 3-6 depicts the temporal variability of WST at a representative point in the middle of the lake (21°31'S, 24°56'E).

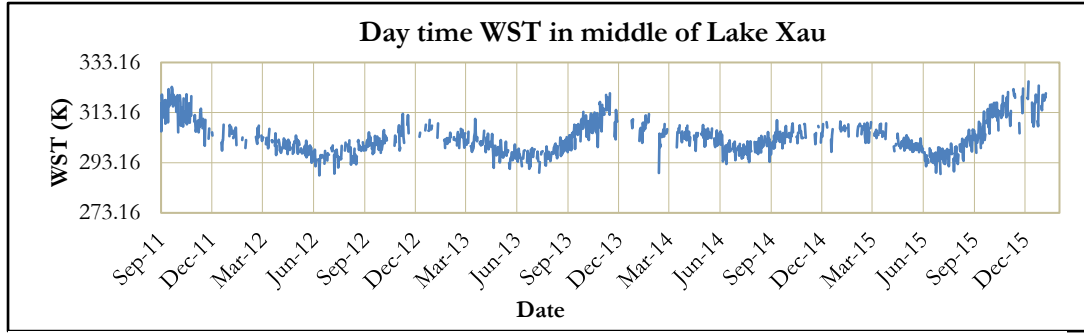


Figure 3-6 Temporal variability of WST in the middle of LX

Step 2: - Calculating the instantaneous fluxes and daily estimates

The instantaneous flux can be calculated using instantaneous daytime LST as input to calculate the instantaneous net radiation (R_N), change of heat flux (G), sensible heat flux (H) and latent heat (λE), all measured in (Wm^{-2}). The instantaneous energy balance can be calculated by the equation below, as Timmermans et al. (2016) suggested.

$$R_N = G + H + \lambda E \quad \text{Equation 3-2}$$

where λ is the latent heat of vaporization (Jkg^{-1}), and E is the evaporated water (kg). As described in the equations below, the net radiation results from the balance between net shortwave radiation (S_N) and longwave radiation (L_N).

$$R_N = S_N + L_N \quad \text{Equation 3-3}$$

$$R_N = (1 - \rho_0) * R_s^\downarrow + \varepsilon_0 * \varepsilon_a * \sigma * T_a^4 - \varepsilon_0 * \sigma * T_s^4 \quad \text{Equation 3-4}$$

where ρ_0 is the surface albedo (-), R_s^\downarrow incoming shortwave radiation (Wm^{-2}), ε_0 and ε_a are the surface and atmospheric level emissivity (-), σ Stefan-Boltzmann constant ($5.6697 \times 10^{-8} Wm^{-2}K^{-4}$) and T_a and T_s are the surface temperature and air temperature (K). The DATTUDUT model parametrizes all the input components based on the LST (T_o) and the T_{min} and T_{max} values of LST in (K) during the daytime. The surface albedo ranges from 0.05 to 0.25, calculated by the equation below.

$$\rho_0 = 0.05 + \left(\frac{T_o - T_{min}}{T_{max} - T_{min}} \right) * 0.2 \quad \text{Equation 3-5}$$

Incoming shortwave radiation is calculated using a simplified formula that is a multiplication product of shortwave atmospheric transmissivity (-) and S_{exo} is exo-atmospheric evaporation ($1367 Wm^{-2}$), both of which are affected by the sun-earth geometry (Campbell and Norman, 1998; Monteith and Unsworth, 1990; Timmermans et al., 2016).

$$R_s^\downarrow = \tau * S_{exo} \quad \text{Equation 3-6}$$

The atmospheric transmissivity (τ) can be obtained by following the equation below (Burridge and Gadd, 1974; Timmermans et al., 2016).

$$\tau = 0.6 + 0.2 * \sin(\alpha) \quad \text{Equation 3-7}$$

where α represents the solar elevation angle (rad). For this study, since the area is small, a constant value of 0.7 was taken as the atmospheric transmissivity value, following the suggestion of Timmermans et al. (2016). Therefore the apparent atmospheric emissivity (ϵ_a) can be obtained following the approximation by Bastiaanssen et al. (1998),

$$\epsilon_a = 1.08 * (-\ln \tau)^{0.265} \quad \text{Equation 3-8}$$

The instantaneous daytime LST was adopted to represent the daily evaporative fraction index (Λ_{24}). The soil heat flux and sensible heat flux on Equation 3-2 were assumed to be neglected in daily estimation, as suggested by Timmermans et al. (2016). The following equations were adopted from Timmermans et al. (2016) to calculate the instantaneous evaporative fraction index (Λ_i) and daily evaporative fraction index (Λ_{24}).

$$\Lambda_i = \frac{T_{\max} - T_0}{T_{\max} - T_{\min}} \quad \text{Equation 3-9}$$

$$\Lambda_i = \Lambda_{24} = \frac{\lambda E_{24}}{R_{N,24}} \quad \text{Equation 3-10}$$

where T_{\max} is the hottest pixel in an instantaneous LST image (K), whereas T_{\min} is the coldest pixel on an instantaneous LST image (K). The amount of net radiation was calculated by Equation 2; however, the following equations are needed to obtain the daily net radiation ($R_{N,24}$ in MJm^{-2}).

$$R_{N,24} = S_{N,24} + L_{N,24} \quad \text{Equation 3-11}$$

$$S_{N,24} = (1 - \rho_{0,24}) * \tau_{24} * S_{\text{exo},24} \quad \text{Equation 3-12}$$

$$L_{N,24-\text{avg}} = -110 * \tau_{24} \quad \text{Equation 3-13}$$

where $S_{N,24}$ is the daily net shortwave radiation in MJm^{-2} , whereas the $L_{N,24}$ is measured in W m^{-2} to change it to the daily estimate; it is needed to be multiplied by day length. The rest of the parameters, such as τ_{24} daily average transmissivity (-) and $\rho_{0,24}$ daily average surface albedo, were taken as the instantaneous value for simplification. The instantaneous value ρ_0 can be calculated by Equation 3-5, and the $S_{\text{exo},24}$ is calculated by integrating the exo-atmospheric radiation from sunrise to sunset as suggested by Timmermans et al. (2016). Finally, the daily evaporated lake water, $E_{24}=E_{\text{LK}}$ (kg m^{-2}), was calculated by Equation 3-14, and the latent heat of vaporization, $\lambda(\text{MJ Kg}^{-1})$, was also calculated by Equation 3-15.

$$E_{24} = \frac{\Lambda_{24} * R_{N,24}}{\lambda} \quad \text{Equation 3-14}$$

$$\lambda = 2.501 - 0.002361 * (T_{\min} - 273.15) \quad \text{Equation 3-15}$$

To calculate the temporal variability of the lake's daily evaporation, batch processing software such as ILWIS and the Esri ArcGIS model builder were used to calculate the temporal variability of the LX evaporation rate. The ILWIS script used for calculating the daily evaporation using the DATTUTUDT model is in Appendix-3.

III. Calculating volumetric evaporation

After calculating the temporally variable evaporation rate, the volumetric water evaporation can be calculated by multiplying the evaporation rate by the lake's surface area, as suggested by (Zhao et al., 2020), as shown in the equation below.

$$V_E = E_{LK} * A \quad \text{Equation 3-16}$$

where V_E is the volume of evaporated water (km^3), A is the enhanced surface area of the lake (km^2), and E_{LK} is the daily rate of lake evaporation (mm day^{-1}).

3.4. Conceptual model

A conceptual model is a descriptive representation of the system regime. Anderson et al. (2015) state that "*conceptual model is a qualitative representation of a groundwater system that conforms to hydrological principles and is based on geological, geophysical, hydrological, hydrogeochemical, and other ancillary information*" (p-29). The conceptual model offers a broad foundation for creating a numerical model based on the region's early hydrogeological knowledge (Anderson et al., 2015). According to Anderson et al. (2015), there are four main steps in defining the conceptual model for groundwater flow modelling, which are: 1) defining system boundaries; 2) defining hydrostratigraphic and hydrogeologic properties; 3) defining flow system pattern, direction, and flow rates; and 4) defining preliminary water balance. The following section describes the steps in developing the conceptual model and the previous knowledge in the study area.

3.4.1. System boundaries

The conceptual model's boundary conditions can be physical or hydraulic features. The conceptual model boundaries and hydrological conditions are the key inputs for the mathematical boundary conditions of the numerical groundwater model (Anderson et al., 2015). The previous study on the area by Mitiku (2019) identified the lateral boundary condition of the study area (i.e., the BR area) using a potentiometric map by analyzing the borehole groundwater level data from the Botswana Department of Water and Sanitation (DWS) and Botswana Geoscience Institute (BGI). According to his findings, the study area has a constant head boundary (CHD) to the northwest, no flow boundary to the north, a general head boundary to the southeast, and a recharge boundary (RCH) to the west. In the southwest direction of the study area, a study by Lekula and Lubczynski, (2019) characterized a flow head boundary in the direction of Makgadikgadi Pans. Therefore, a regional system boundary map was defined by combining the mentioned studies and the available borehole data from DWS, as shown in Figure 2-6.

3.4.2. Defining hydrostratigraphic units

According to Seaber (1988), "*a hydrostratigraphic unit is a body of rock distinguished and characterized by its porosity and permeability*" (p-14). The previous studies on the area and surroundings have refined the earlier lithostratigraphy study (Carney et al., 1994) for identifying the rock's ability to store and transmit water by subdividing into the respective hydrostratigraphic units (Lekula et al., 2018; VanderPost and McFarlane, 2007; Water Surveys Botswana (Pty) Ltd, 2006). According to Anderson et al. (2015), hydrostratigraphic can be obtained by combining several stratigraphical formations with similar hydraulic properties. In this study, the stratigraphical formations have been defined by analyzing the previous studies of the area, such as (Carney et al., 1994; Lekula et al., 2018; Water Surveys Botswana (Pty) Ltd, 2006) and using the in-situ borehole data.

Previous studies on the area classified and identified the hydrostratigraphic units differently; for example, a study on the western boundary of BRB by Lekula et al. (2018) classified the Central Kalahari Basin into six hydrostratigraphic units. Naming Kalahari Sand Unit (KSU), Stormberg Basalt Aquitard (SBA), Lebung Aquifer (LA), Inter-Karoo Aquifer (IKA), Ecqa Aquifer (EA) and Ghanzi Aquifer (GA). In contrast, a study in the southeastern part of BRB by Water Surveys Botswana (Pty) Ltd (2006) identified groundwater in all stratigraphic units. However, the amount and quality of the water are very variable throughout the study area. According to Water Surveys Botswana (Pty) Ltd (2006), the main hydrostratigraphic units are the Kalahari Group Aquifer, Kalahari Through Aquifer, Karoo Aquifers, and Ecqa Group Aquifer.

This study uses the above information and in-situ borehole data to develop a hydrostratigraphic model using RockWorks-17 (RockWorks) software. RockWorks software is a comprehensive program that enables users to create, manage, and visualize different geological diagrams (i.e., 2-D, 3-D, and cross-sections) of subsurface geology and hydrostratigraphy (Trabelsi et al., 2013). A 500 x 500 m spaced grid and an inverse distance interpolation method were used to create a 3-D hydrostratigraphic model of BRB.

A five-layer hydrostratigraphic unit, namely Kalahari Sand, Stormberg Lava, Lebung, Ecqa, and Ghanzi, has been identified as a hydrostratigraphic unit. However, based on the neighbouring study by Lekula and Lubczynski (2019), the bottom hydrostratigraphic unit of the Ghanzi aquifer is a stable aquifer with negligible groundwater interaction with the overlying aquifers. The Ecqa and Lebung aquifers were merged since they have relatively identical hydraulic properties. Finally, a three-layer hydrostratigraphic model was used where the three thickness map (KSU, SBA and LA+EA) was generated by exporting each unit of the 3-D grid file to ASCII XYZ file format and further imported and processed in the ArcGIS.

3.4.3. Defining flow system pattern, direction, and flow rate

The groundwater flow direction within the study area of the conceptualized model boundary is mainly indicated using arrows in the available potentiometric map or hydrogeological cross-sections. Anderson et al. (2015) state that the general flow direction can be determined using different available information such as contour maps of groundwater level, potentiometric surface, boundary lines and location of recharge and discharge. For this study, the groundwater flow pattern has been indicated in Figure 2-6 by arrows in the potentiometric map using the available previous studies on the area (Lekula et al., 2018; Mitiku, 2019; Water Surveys Botswana (Pty) Ltd, 2006).

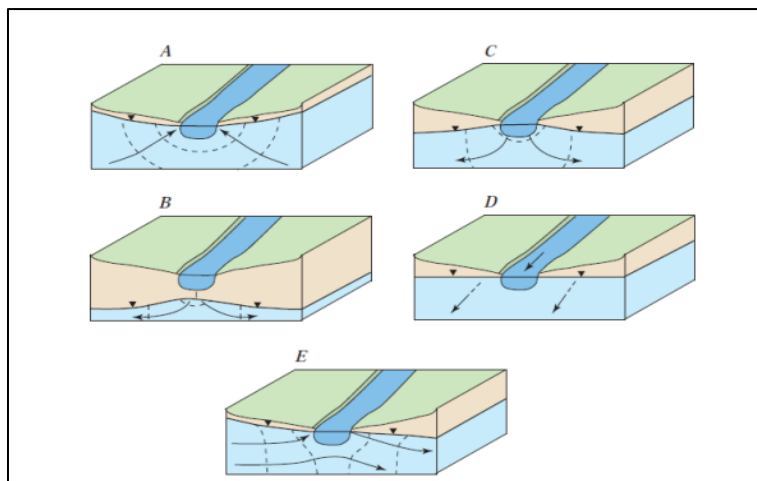


Figure 3-7 Conceptualized streamflow with groundwater a) receive groundwater inflow; b) disconnected and loses water to groundwater; and c) connected and loses water to groundwater d) zero interaction and e) groundwater pass through the stream: (Winter et al., 1998)

The quantitative assessment of SW-GW interaction using IHMs representing the water exchange rate between surface water and groundwater is crucial (Anderson et al., 2015). The study area's arid climate conditions have influenced the surface water's interaction with groundwater, resulting in unsaturated hydraulic property-dependent interactions between groundwater and surface water (Water Surveys Botswana (Pty) Ltd, 2006). The BR's interaction with groundwater is complex to conceptualize due to the BR's erratic and unstable flow characteristics. According to Woessner (2000), there are five possible river and groundwater interaction combinations. This study conceptualized five types of interaction between BR and groundwater following the groundwater head and the river stage location.

The LX interaction with groundwater is also crucial for developing the full conceptual model of BRB. According to Winter et al. (1998), the lake's interaction with groundwater is mainly classified into four basic conditions depending on the lake level and groundwater level positions. Figure 3-8 (d) below conceptualises this study's LX interaction with groundwater.

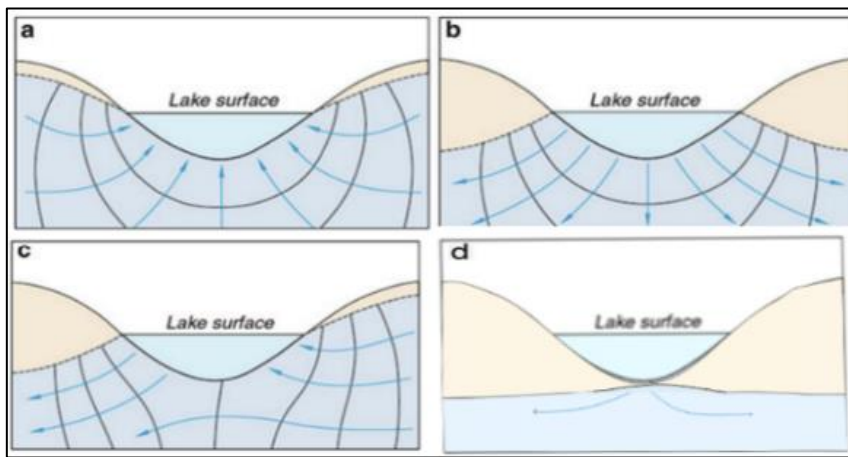


Figure 3-8 Conceptualize lake and groundwater interaction in BRB; a) gaining; b) losing; c) losing and gaining; d) disconnected losing (Woessner, 2000)

3.4.4. Defining water budget components

The water balance of the entire sub-basin steady-state model domain (26,204 km²) can be represented by the following equations

$$\text{Inflow} - \text{Outflow} = 0 \quad \text{Equation 3-17}$$

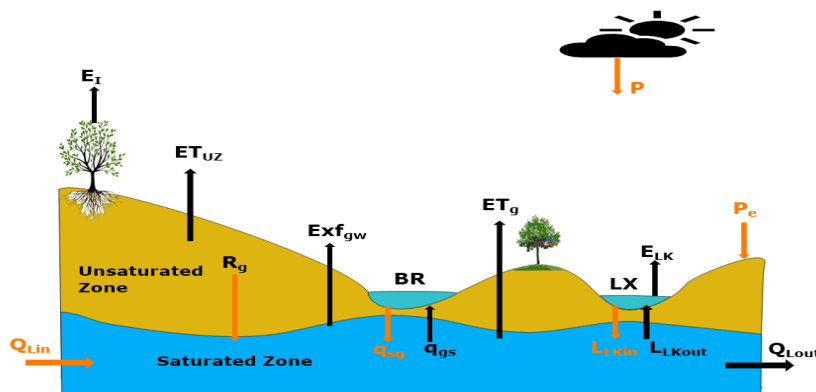


Figure 3-9 Schematization of the system zones and components

The system consists of two zones, the unsaturated zone overlaying the saturated zone. The total water balance of the entire basin can be expressed as follows. For the reason of simplicity (different reference areas of the lake and terrestrial area), the Equation 3-18 is solved in $[L^3T^{-1}]$ in contrast to all other equations are resolved in $[LT^{-1}]$

$$P + q_{in} + Q_{Lin} = ET + Q_{Lout} \quad \text{Equation 3-18}$$

where P is the precipitation rate over all the study area, q_{in} is the stream flow at the inlet of the modelled area, which can be found by in-situ measurement (Maun station), q_{Lin} is the lateral groundwater inflow to modelled area, and q_{Lout} is the lateral groundwater outflow from the modelled area, ET is total evapotranspiration consisting of land surface evapotranspiration (ET_{LD}) and lake evaporation (E_{LK}).

$$ET = ET_{LD} + ET_{LK} = E_I + ET_{uz} + ET_g + E_{LK} \quad \text{Equation 3-19}$$

where E_I is the canopy interception rate, ET_{uz} is unsaturated zone evapotranspiration (not calculated by the steady-state model), and ET_g is groundwater evapotranspiration, equal to ET_{ss} in the steady-state model.

The lateral inflow and outflow from the modelled area can be calculated using Equation 3-20 and 3-21, respectively.

$$Q_{Lin} = Q_{GHBin} + Q_{RCHin} + Q_{CHDin} \quad \text{Equation 3-20}$$

$$Q_{Lout} = Q_{GHBout} + Q_{CHDout} + Q_{DRNout} \quad \text{Equation 3-21}$$

The Q_{GHB} , Q_{CHD} , Q_{DRN} , and Q_{RCH} are the boundary lateral groundwater inflow and outflow, as presented in Figure 2-6.

The stream outflow from the Boteti River, which is also the inflow into Lake Xau (q_L), can be calculated using Equation 3-23 below.

$$q_L = RI^s + Exf_{gw}^s + q_B \quad \text{Equation 3-22}$$

where q_B is a base flow, RI^s is the rejected infiltration routed to streams, and Exf_{gw}^s is groundwater exfiltration routed to streams.

The land surface and unsaturated zone water balance can be calculated as

$$P_e = RI + ET_{uz} + R_g \quad \text{Equation 3-23}$$

where P_e is effective precipitation which can be found by subtracting interception loss (E_I) from precipitation (P), ET_u is unsaturated zone evapotranspiration (not simulated in steady state), and R_g is the gross recharge.

The lake-water balance extracted from the lake package output file can be expressed as follows the surface area of the lake (A_L) was used to convert the volumetric output of the model to $[LT^{-1}]$

$$P + q_L + L_{LKin} = E_{LK} + L_{LKout} \quad \text{Equation 3-24}$$

where P is precipitation on the lake, q_L is stream inflow at the lake's inlet, and L_{LKin} and L_{LKout} are lake leakage to groundwater and groundwater leakage to the lake, respectively.

The saturated zone groundwater budget can be calculated by

$$R_g + q_{sg} + L_{Lkin} + Q_{Lin} = Exf_{gw} + L_{LKout} + ET_g + q_{gs} + Q_{Lout} \quad \text{Equation 3-25}$$

where q_{sg} is stream leakage to groundwater, q_{gs} is groundwater leakage to streams, and Exf_{gw} is groundwater exfiltration.

The net groundwater recharge (R_n) in BRB can be calculated by subtracting the groundwater exfiltration and groundwater evapotranspiration from gross recharge.

$$R_n = R_g - Exf_{gw} - ET_g \quad \text{Equation 3-26}$$

3.5. Numerical model

3.5.1. General modelling setup

The MODFLOW-6 is a 3D control-volume finite-difference (CVFD) model developed by USGS. MODFLOW-6 can be supported by various user interfaces, including Model Muse, GMS, and Python packages (FloPy). The MODFLOW-6 can simulate groundwater flow (GWF) in both steady and transient states. The governing equation in MODFLOW-6 is developed by McDonald and Harbaugh (1988), as indicated in Equation 3-27.

$$\frac{\partial}{\partial x} \left(K_x \cdot \frac{\partial h}{\partial x} \right) + \frac{\partial}{\partial y} \left(K_y \cdot \frac{\partial h}{\partial y} \right) + \frac{\partial}{\partial z} \left(K_z \cdot \frac{\partial h}{\partial z} \right) + W = 0 \quad \text{Equation 3-27}$$

where K_x , K_y and K_z are the value of hydraulic conductivity along x, y and z directions [L/T], h is the groundwater head [L], W is a volumetric flux per unit volume representing sink/source of water with $W < 0$ for sink and $W > 0$ for the source [$L T^{-1}$], and t is time [T].

A three-layer system was used to simulate the groundwater flow (GWF) through the upper unconfined aquifer of Kalahari Sand, the lower semiconfined aquifer of merged Lebung and Ecqa, and with a middle aquitard layer of Stormberg Basalt, following the hydrogeological conceptual model. In this study, the latest version of MODFLOW (modular finite-difference flow model), MODFLOW-6, was selected to model the groundwater flow of BRB. The MODFLOW-6 was selected due to its ability to handle the complex problem involving water-table conditions using the controlled-volume finite-difference (CVFD) method under Newton Raphson's formulation. Moreover, MODFLOW-6 is selected due to its ability to support alternative grid discretization packages such as Discretize by Vertices (DISV) and Unstructured Discretization (DISU) than the regular squared grid (DIS) package. The flexibility of grid design by DISV and DISU enables users to increase the resolution around focus areas such as streams, lakes, and groundwater observation areas (Langevin et al., 2022).

This study first used a DIS grid of 1000 x 1000 m for all three layers under the ModelMuse (ModelMuse version 5.0.18) interface in WGS 84 UTM Zone 35S (epsg-32375) coordinate system. Later, a local refinement was applied around interest areas of lakes, streams, and groundwater level monitoring boreholes

with the DISV package of Quadtree refinement. Finally, 68762 active cells were set, ranging from 250 x250 m to 1000 x 1000 m.

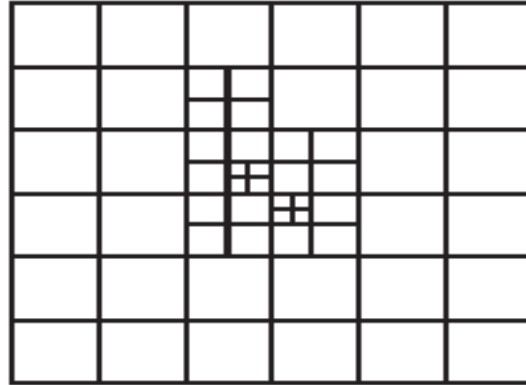


Figure 3-10 Example of quadtree model refinement, source: (Langevin et al., 2022)

Considering discretization in the vertical direction, three active layers and one additional inactive layer were used to simulate the GWF of BRB. The three active layers were imported following the thickness map produced in the hydrogeological conceptual model. The additional non-active layer was set to simulate the LX interaction with the groundwater by applying the MODFLOW Lake7 package (Merritt and Konikow, 2000) following the study of El-Zehairy et al. (2018).

The model top elevation is defined using the ALOS PALSAR DEM. The rest of the model elevations were defined according to the equation below.

$$\text{Layer1} = \text{Model Top} - \text{Thickness1} \quad \text{Equation 3-28}$$

$$\text{Layer2} = \text{Layer1} - \text{Thickness2} \quad \text{Equation 3-29}$$

$$\text{Layer3} = \text{Layer2} - \text{Thickness3} \quad \text{Equation 3-30}$$

where:

Model Top is the top elevation of the model defined by DEM (m a.s.l)

Thickness 1 thickness of the upper aquifer (m)

Layer 1 is the bottom elevation of the upper aquifer (m a.s.l)

Thickness 2 thickness of middle aquitard (m)

Layer 2 is the bottom elevation of the middle aquitard (m a.s.l)

Thickness 3 thickness of the lower aquifer (m)

Layer 3 is the bottom elevation of the lower aquifer (m a.s.l)

The additional non-active layer elevation was set 1 m above the model top outside the lake area and maximum lake stage elevation in the lake area.

The model units were set in meters for all length measurements and days for all time measurements. The 10-year hydrological period from 1st October 2010 to 30th September 2020 was selected for steady-state simulation. The average input driving forces and state variables were defined for a steady state.

3.5.2. Model forcing

Developing a representative IHM model requires two crucial model forcing, effective precipitation (P_e) and potential evapotranspiration (PET).

3.5.3. Effective precipitation (Infiltration rate)

To find the daily spatiotemporally variable effective precipitation (P_e), the daily interception rate is subtracted from the daily precipitation (rainfall) rate.

3.5.3.1. Precipitation

This study uses Satellite-based Rainfall Estimates (SREs) since SREs are alternative rainfall estimation mechanisms in sparsely distributed rainfall stations. Through time there has been a development in SREs products such as the Global Precipitation Climatology Project (GCP), Tropical Applications of Meteorology using Satellite and ground-based observations (TAMSAT) and Climate Hazards Infrared Precipitation with Stations (CHIRPS). However, each of the SREs products has a different spatial and temporal resolution and coverage. For this study, the daily SREs product of CHIRPS was used as the main input for the IHM model.

This study used the raw daily CHIRPS product because it is a moderate resolution (0.05°) Cold Cloud Duration (CCD) based data set with a long rainfall observation record from 1981 to the present with global coverage blended with in-situ rainfall stations (Funk et al., 2015).

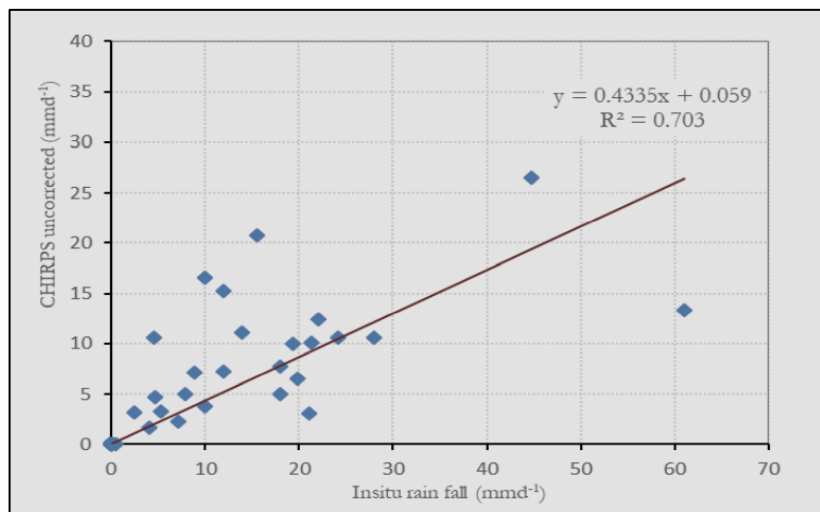


Figure 3-11 Daily rainfall at ORC vs uncorrected CHIRPS measurement Source: (Mitiku 2019)

3.5.3.2. Interception

Interception (E_i) is a process in which precipitation is caught by a vegetative canopy and redistributed to the ground, atmosphere, or plant. The amount of precipitation returned to the atmosphere by evaporation from plant surfaces or absorbed by plants is called interception loss (Merriam, 1960).

Interception loss mainly depends on the type of vegetation cover of the area and the duration and intensity of rainfall (Gash, 1979 & Maitre et al., 1999). This study uses the FAO-WaPOR average decadal interception product for each 10-day interval with 250 m spatial resolution. The FAO-WaPOR estimates the interception loss E_i (mm day⁻¹) by combining the precipitation (P), coefficient of vegetation cover and LAI (leaf area index), as shown in Equation 3-31 below (FAO, 2020). The interception loss mainly depends on LAI and the amount of rainfall (i.e., interception is very high with a small amount of rainfall, but as rainfall increases,

the fraction intercepted decreases quickly). Equation 3-32. The second step is calculating the I_{lai} using the coefficient of vegetation cover C_{veg} using Equation 3-33.

$$E_i = 0.2I_{lai} \left[1 - \frac{1}{1 + \frac{C_{veg} P}{0.2I_{lai}}} \right] \quad \text{Equation 3-31}$$

I_{lai} is the LAI (m^2m^{-2}) calculated in two steps: first, the coefficient vegetation cover C_{veg} using NDVI (normalized vegetation index) by

$$\begin{cases} C_{veg} = 0 & \dots \dots \dots I_{ndvi} \leq 0.125 \\ C_{veg} = 1 - \left(\frac{0.8 - I_{ndvi}}{0.8 - 0.125} \right)^{0.7} & \dots \dots \dots 0.125 < I_{ndvi} < 0.8 \\ C_{veg} = 1 & \dots \dots \dots I_{ndvi} \geq 0.8 \end{cases} \quad \text{Equation 3-32}$$

$$\begin{cases} I_{lai} = 0 & \dots \dots \dots I_{ndvi} \leq 0.125 \\ I_{lai} = \frac{\ln(-(C_{veg} - 1))}{-0.45} & \dots \dots \dots 0.125 < I_{ndvi} \leq 0.795 \\ I_{lai} = 7.63 & \dots \dots \dots I_{ndvi} > 0.795 \end{cases} \quad \text{Equation 3-33}$$

The following processing steps were followed to obtain a daily spatio-temporal variability of interception loss rate from 1st October 2010 to 30th September 2020.

- I. Download the decadal (each 10-day) temporal resolution and 250 m spatial resolution interception rate from WaPOR and rescale the download interception rate by multiplying with a scale factor of 0.1 to change the units into $mm \text{ day}^{-1}$.
- II. Resampling of the rescaled daily raster to 1x1 km spatial resolution raster.

3.5.4. Potential evapotranspiration

The MODIS 8 days lumped 500 m spatial resolution evapotranspiration (PET) was used as spatio-temporal PET data. The MODIS PET is selected for this study because the area has a scarcity of in-situ measurements. Moreover, the study area has low spatial variability PET since the spatial distribution of land cover is insignificant to vary the effect of crop factor for calculating PET (i.e., above 95% is covered with small trees and shrubs) (Lekula and Lubczynski, 2019).

The MODIS 8-day 500 m resolution PET product was retrieved and downscaled from lumped days; days to daily values by dividing with the respective lumped day range to get the daily spatio-temporal variability of PET.

3.6. System parametrization

In MODFLOW-6, the NPF package defines the hydraulic conductance of the aquifer and manages the aquifer wetting and drying conditions by assigning individual intercell conductance values. The initial horizontal (K_h) and vertical ($K_v=K_z$) hydraulic conductivity of this study was assigned based on the literature review and available pumping test data in the study area. The table below presents the initial parameters used for the NPF package; initial values were adopted from the literature (Lekula and Lubczynski, 2019; Water Surveys Botswana (Pty) Ltd, 2006).

Table 3-2 System parametrization of BRB for NPF, where L are literature-based information and S is a spatially variable distribution

MODFLOW-6 packages	Parameters	Min-value	Max-value	Units	Source	Variability	Remarks
NPF	K_h (layer1)	0.001	40	m day ⁻¹	L	S	calibrated
	K_h (layer2)	3.1E-05	0.009	m day ⁻¹	L	S	calibrated
	K_h (layer3)	0.132	0.95	m day ⁻¹	L	S	calibrated

3.6.1. External boundary conditions

This study defined five types of boundary conditions based on the regional groundwater flow direction as described in Figure 2-6. The general head flow (GHB), recharge (RCH) and drain (DRN) boundaries were assigned based on the incoming or outgoing groundwater flow, respectively, whereas the no-flow (NFB) and constant head boundaries (CHD) were assigned by looking at physical features (river, topographic divided and faults) and the groundwater contour lines.

3.6.1.1. General head boundary (GHB)

Figure 2-6 shows the GHB was assigned in the southwestern part of the study area, where groundwater flow was uncertain. The required initial parameters for hydraulic conductance of the first and third layer GHB boundary were as assigned as 1.25 m²day⁻¹ and 40 m²day⁻¹, respectively.

3.6.1.2. Recharge boundary (RCH)

The recharge package (RCH) in MODFLOW-6 was used to assign a specified flow from the western boundary of the study area, as shown in Figure 2-6. The neighbouring study by Lekula and Lubczynski (2019) identified a groundwater outflow from the CKB to Makgadikgadi Pan crossing the BRB from west to east. Two boreholes, BH9715 and Z8829, with groundwater levels 997.84 and 917 m.a.m.a.l, located 35 km apart, are taken to calculate the gradient of groundwater flow. The hydraulic conductivity was assumed as 12.5 m day⁻¹, and the layer's average thickness was 50 m. Therefore, the estimated lateral groundwater inflow (recharge) of 0.3 m day⁻¹ was applied to 205 cells located in the western boundaries shown in Figure 2-6.

3.6.1.3. Drain boundary (DRN)

The DRN boundary in the study area was assigned for groundwater outflow cells along the eastern side of the study area, as indicated in Figure 2-6. The drain cells were assigned for layers 1 and 3 to simulate the groundwater outflow from the system. The initial drain hydraulic conductance value of 0.5 m² day⁻¹.and 40 m² day⁻¹ was assigned for the first and third layer, respectively.

3.6.1.4. No-flow boundary

The no-flow boundary is mainly assigned for the topographic divided areas and areas where physical flow barriers exist, such as faults. The northeast part of the study area was assigned as a no-flow boundary, as shown in Figure 2-6.

3.6.1.5. Constant head flow (CHD)

The CHD boundaries assigned to the head were constant throughout the model simulation or for the head specified for each simulation time. For this study, 954 m a.s.l was assigned by averaging stream bed level records obtained from Maun station. The location of the boundary is shown in Figure 2-6.

3.6.2. Internal boundary conditions

3.6.2.1. Lake simulation (LAK)

The MODFLOW-6 contains the different advanced packages that help stimulate the head-dependent flux exchange. Lake package (LAK) is one of the advanced packages that help estimate the seepage amount between the lakebed and the aquifer. The LAK uses Darcy's Law to calculate the head difference between lake stage and groundwater level (GWL) through seepage and uses a continuity equation to solve the water balance equation.

This study uses the LAK to simulate the seepage (interaction) between the LX and the overlying aquifer. Using Darcy's Law, the seepage can be estimated. The seepage depends on the lake stage, GWL, and groundwater conductance between the lake and aquifer.

$$q = K_{Lb} \frac{h_L - h}{\Delta x} \quad \text{Equation 3-34}$$

where q is specified discharge [LT^{-1}], K_{Lb} hydraulic conductivity of lakebed [LT^{-1}]; h_L is lake stage [L]; h is the GWL [L], and Δx is the distance between the lake bottom to centre of connected overlaying active aquifer [L].

To quantify the amount of volumetric flux exchange (Q) [L^3T^{-1}] between the lake and aquifer, the wetted area of the lake (A_L) should be multiplied with specified discharge (q) as follow.

$$Q = q A_L = \frac{KA_L}{\Delta x} (h_L - h) = C(h_L - h) \quad \text{Equation 3-35}$$

where C is the conductance of lakebed material [L^2T^{-1}], and $K/\Delta x$ is the leakance of the lakebed [T^{-1}]. In this study, the lake-aquifer interaction area was assumed to be a vertical connection (lake saturation = 1); it is hypothesized that the lake is losing water to groundwater.

The lake water budget and leakage rate between the lake and the connected aquifer are computed for each time step (iterations). The following equations calculate the volumetric flux and lake stage water balance, as El-Zehairy et al. (2018) simplified.

$$h_L^n = h_L^{n-1} + \Delta_t \frac{P - E_{LK} + L_{LKnet} + q_L}{A_L} \quad \text{Equation 3-36}$$

where h_L^n and h_L^{n-1} are the lake stages [L] in consecutive time, Δ_t is the time step [T]. Whereas P , E_{LK} , q_L , and L_{LKnet} are precipitation, evaporation, incoming stream flow to the lake, and net lake leakage between lake leakage to groundwater and groundwater leakage to the lake [L^3T^{-1}], respectively.

There are many lake property input parameters for simulating the LAK package in MODFLOW-6, such as surface depression depth (d_{surf}), lakebed thickness (L_{thk}), lakebed hydraulic conductivity (K_{Lb}), connection length ($connlen=L_{con}$), a top elevation of the lake ($telev=L_{htop}$), and bottom elevation ($belev=L_{hbot}$), initial lake stage elevation ($strt=L_{hint}$) values were assigned as 0.2 m, 0.005 m, 0.05 m, 0 m and 927, 913, 916 m

a.s.l, respectively. In addition, the maximum lake time properties parameters were adjusted depending on the model state condition; the lake table section is filled depending on the maximum estimated lake capacity obtained in section 3.3.1.

3.6.2.2. Stream flow routing (SFR)

The SFR package is also one of the advanced stress packages in MODFLOW-6. SFR is applied to simulate the BR interaction with the groundwater. The SFR package calculates the flow across the streambed with two methods 1) specified stream depth (simple routing option) and 2) stream depth calculated (active reaches). This study used the active stream depth to simulate the BR interaction with GW.

Various parameters are required to simulate the interaction of streams with the groundwater. The reach width ($r_{wid}=W$), gradient ($r_{grd}=I_s$), streambed top ($r_{tp}=S_{top}$), streambed thickness ($r_{bth}=S_{thk}$) and streambed hydraulic conductivity ($r_{hk}=K_{sb}$) are assigned depending on the stream segments (reaches) and calibrated to get reasonable water balance. The following table provides the initial parameter set for setting the numerical model.

Table 3-3 Initial parameters for the SFR package

Reach number	Parameter	Range	Units	Remark
Reach 1	W	15	m	Adjusted by trial and error
	I_s	0.025		
	S_{top}	956.78 to 952	m a.s.l	
	S_{thk}	1	m	
	K_{sb}	2.5	m day ⁻¹	
Reach 2	W	15	m	Adjusted by trial and error
	I_s	0.03		
	S_{top}	952 to 937	m a.s.l	
	S_{thk}	0.5	m	
	K_{sb}	5	m day ⁻¹	
Reach 3	W	20	m	Adjusted by trial and error
	I_s	0.03		
	S_{top}	937 to 934	m a.s.l	
	S_{thk}	0.5	m	
	K_{sb}	3.75	m day ⁻¹	
Reach 4	W	25	m	Adjusted by trial and error
	I_s	0.035		
	S_{top}	934 to 922	m a.s.l	
	S_{thk}	0.5	m	
	K_{sb}	4	m day ⁻¹	

3.6.2.3. Unsaturated zone package (UZF)

The UZF package simulates the flow through the unsaturated flow zone and adds the resulting recharge to the aquifer (saturated zone). UZF estimates the vertical flow through the unsaturated zone using a kinematic wave approximation of the Richards equation (Langevin et al., 2017). The equation below describes the simplified form of Richard's equation, assuming that the negative pressure gradient is negligible

$$\frac{\delta\theta + \delta k(\theta)}{\delta t} + i_{ET} = 0 \quad \text{Equation 3-37}$$

where θ is the volumetric of water content [L^3L^{-3}], $K(\theta)$ is vertical unsaturated hydraulic conductivity as a function of water content [LT^{-1}], and i_{ET} is unsaturated zone ET rate per unit depth [$LT^{-1}L^{-1}$].

The UZF package has two main sections, steady and time-varying properties sections. The steady properties section includes surface depth (d_{surf}) in [L], vertical saturated hydraulic conductivity (K_{sat}) in [LT^{-1}], initial water content (θ_i) in [L^3L^{-3}], saturated water content (θ_{sat}) [L^3L^{-3}], residual water content (θ_{resid}) [L^3L^{-3}], and Brooks-Corey exponent (ϵ) [-]. The mentioned parameters are used to estimate the $K(\theta)$ by applying the hydraulic conductivity equation below (Brooks and Corey, 1966).

The time-varying property section is used to simulate the land surface driving forces (i.e., PET and infiltration rate), which are estimated in section 3.5.2. The extinction water content ($EXTWC = \theta_{ext}$) was assigned following the study by Lekula and Lubczynski (2019) as $\theta_r + 0.01$. However, the value of θ_r was assigned lower than the value used by Lekula and Lubczynski (2019) since θ_r is lower than specific retention in MODFLOW-6.

$$K(\theta) = K_{sat} \left(\frac{\theta - \theta_{resid}}{\theta_{sat} - \theta_{resid}} \right)^\epsilon \quad \text{Equation 3-38}$$

The extinction depth ($EXTDP = d_{ext}$) was defined based on the LULC map produced in section 2.3, and the range value for each class was assigned following the studies of Obakeng et al. (2007) and Lekula and Lubczynski (2019). The value assigned for each class is 0 m for water, built-up area, and bare soil; 2 m for crops, grass, and flood vegetation; 6 m for medium-size trees and shrubs and 25 m for large trees outside the river belt area. The following table provides the initial parameter values for the simulation of UZF.

Table 3-4 UZF initial parameters

MODFLOW Package	Parameters	Minimum value	Maximum value	Units	Reference
UZF1	d_{surf}	0.1	0.5	m	Literature
	d_{ext}	0	25	m	Fixed
	K_{sat}	0.019	3.1	$m \text{ day}^{-1}$	Calibrated
	θ_r	0.05	0.10	m^3m^{-3}	Literature
	θ_s	0.1	0.4	$m^3 m^{-3}$	Literature
	θ_i	0.05	0.15	$m^3 m^{-3}$	Literature
	ϵ	3.5	3.5	-	Fixed
	θ_{ext}	0.05	0.10	$m^3 m^{-3}$	Literature

While simulating the UZF package, considering the infiltration boundary is essential since the specified infiltration is converted to water content in the UZF package. Two conditions control the specified infiltration rate 1) if the specified infiltration rate is greater than or equal to K_{sat} , the water content is set to saturated water content (θ_{sat}) and 2). if the specified infiltration rate is greater than K_{sat} , then the difference between the specified infiltration rate and K_{sat} will be multiplied by the area of the model cell, and the volumetric water rate will be obtained; and the obtained water will be routed to a stream, lake and wells using water mover package (Langevin et al., 2017).

UZF also simulates the ground seepage to land surface (exfiltration) (Exf_{gw}) by defining d_{surf} . The exfiltrated groundwater (Exf_{gw}) is routed by a water mover (MVR) package to the nearest stream. A brief discussion can be found in the MODFLOW-6 manual by Langevin et al. (2017).

3.6.2.4. Water mover package (MVR)

The MVR package is a new package of MODFLOW, which enables a user to move the water provider package to the receiver package. This study used the MVR to move the rejected and exfiltrated water from the UZF package to the receiver package SFR. Moreover, the package connects the outflow from BR (provider) to LX (receiver).

The flow from providing to a receiver can be calculated in different ways. For this case, for both UZF to SFR and SFR to LAK package, the “FACTOR” option was used. Depending on the flow, the initial FACTOR was assigned 0.75 for both conditions and adjusted by trial and error. The following equation calculates the flow from the provider to the receiver using the FACTOR option.

$$Q_R = \beta \cdot Q_P \quad \text{Equation 3-39}$$

where Q_R is the rate of water that is received [L^3T^{-1}], β is the factor to convert the provider flow rate to receiver flow rate, and it ranges between (0-1) [-], and Q_P is the provider flow rate [L^3T^{-1}].

3.6.2.5. ZONEBUDGET

ZONEBUDGET is a separate post-processor program that simulates the water budget of a specific area of interest in the model. The program calculates the budget for the specific area of interest using the cell-by-cell flow option. This study used ZONEBUDGET to simulate budget in the model layers and a specific area of interest, such as LX.

The layer budget of the KSU aquifer (layer-1) can be calculated as

$$R_g + Q_{Lin} + q_{sg} + L_{LKin} + q_{vin} = ET_g + Q_{Lout} + q_{gs} + EXf_{gw} + q_{vout} \quad \text{Equation 3-40}$$

$$q_{vin} = q_{vin2-1} + q_{vin3-1} \quad \text{Equation 3-41}$$

$$q_{vout} = q_{vout2-1} + q_{vout3-1} \quad \text{Equation 3-42}$$

The layer budget of the SBA aquitard (layer-2) contains only vertical groundwater leakage between the layer-1 and layer-3 and can be calculated as

$$q_{vin1-2} + q_{vin3-2} = q_{vout2-1} + q_{vout2-3} \quad \text{Equation 3-43}$$

The layer budget of LA+EA aquifer (layer-3) contains both vertical and lateral groundwater flow from the boundaries and is calculated using the following equation.

$$Q_{Lin} + q_{vin1-3} + q_{vin2-3} = Q_{Lout} + q_{vout2-1} + q_{vout3-1} \quad \text{Equation 3-44}$$

where q_v indicates the vertical groundwater leakage through layers, subscripts 1, 2 and 3 represent the layer naming.

3.6.3. State variables

The instantaneous state variable that controls the model calibration in the steady-state phase is the static groundwater level obtained from available boreholes and average BR flow and LX volume.

3.6.4. Model calibration

For calibration of the steady-state model, the average long-term stresses (precipitation, PET, stream flow lake evaporation and lake volume) were used as model inputs from 1st October 2010 to 30th September 2020. The steady-state model was calibrated using the forward calibration (manual-trial and error) method to match the observed groundwater heads with simulated groundwater heads. There are different error assessment criteria for assuring acceptable model calibration; the mean error (ME), mean absolute error (MAE), and root mean square (RMSE) are the primary ones used for calibration of the groundwater heads.

The model percentage discrepancy was also used to calibrate the water balance of the groundwater model. The discrepancy error is the percentage determined by subtracting the total inflow or outflow from the total inflow or outflow. The model is considered converged and acceptable when the discrepancy percentage is below 1% (Anderson et al., 2015).

The steady-state model calibration initially was performed using the ModelMuse version 4.6.3; however, the LAK package has a bug which retard the calibration of the lake water balance. Later after personal contact with Dr Richard Winston (U.S.G.S), the new unreleased version of ModelMuse version 5.0.18 was used to simulate the model.

3.6.5. Error assessment and sensitivity analysis

3.6.5.1. Error assessment

The head calibration mentioned in section 3.6.4 ME, MAE, and RMSE were used to evaluate model calibration progress by the following equations.

$$ME = \sum (H_{obs} - H_{sim}) / N \quad \text{Equation 3-45}$$

$$MAE = \sum |H_{obs} - H_{sim}| / N \quad \text{Equation 3-46}$$

$$RMSE = \sqrt{\sum (H_{obs} - H_{sim})^2 / N} \quad \text{Equation 3-47}$$

Where H_{obs} , H_{sim} and N are observed, simulated, and the number of observation groundwater head, respectively, and N is a number of observations.

3.6.5.2. Sensitivity analysis

Sensitivity analysis is performed to identify the model's performance for specified parameter changes. All calibration parameters were retained at their calibrated values to determine the sensitivity of each parameter, except for the selected parameter, which was gradually changed with the percentage factor (Anderson et al., 2015). This study performed a sensitivity analysis for horizontal hydraulic conductivity of aquifer (K_h) lakebed leakance and stream bed hydraulic conductivity.

4. RESULTS

4.1. Lake assessment result

4.1.1. RS-based assessment result of LX Area-Volume-Elevation (AVE)

Depending on the steps mentioned in section 3.3.1, the AVE curve for each month has been produced. The maximum water extent month (November 2012) is selected to show the result and progress. The following figures show the AVE curve of LX for the selected maximum estimation record month of November 2012.

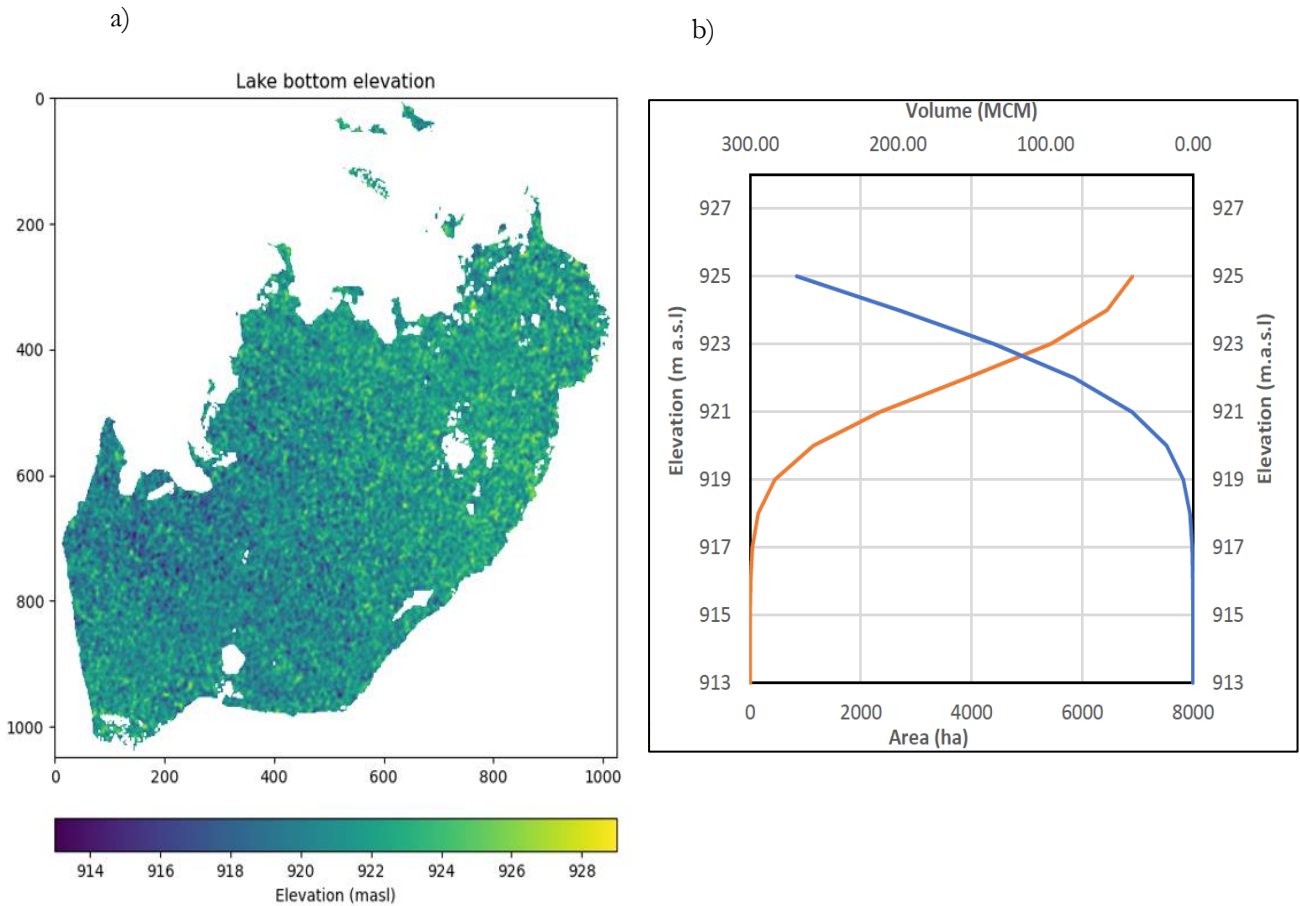


Figure 4-1 a) DEM within maximum extent of LX; combined with DEM b) hypsographic curves of cumulative lake volume and lake area versus lake stage

Depending on the above AVE curve estimation, a maximum volume of 562.54 MCM (million cubic meters) was estimated in November 2012 from the maximum extent of 7259.44 hectares, and water levels range from 913 to 929 m a.s.l. Finally, the historical monthly estimate of the LX area and volume changes are converted to the daily estimate using the linear interpolation method for both area and volume using the python script provided in Appendix-4. Figure 4-2 (a) and (b) below show the daily variability of the LX volume and area, respectively.

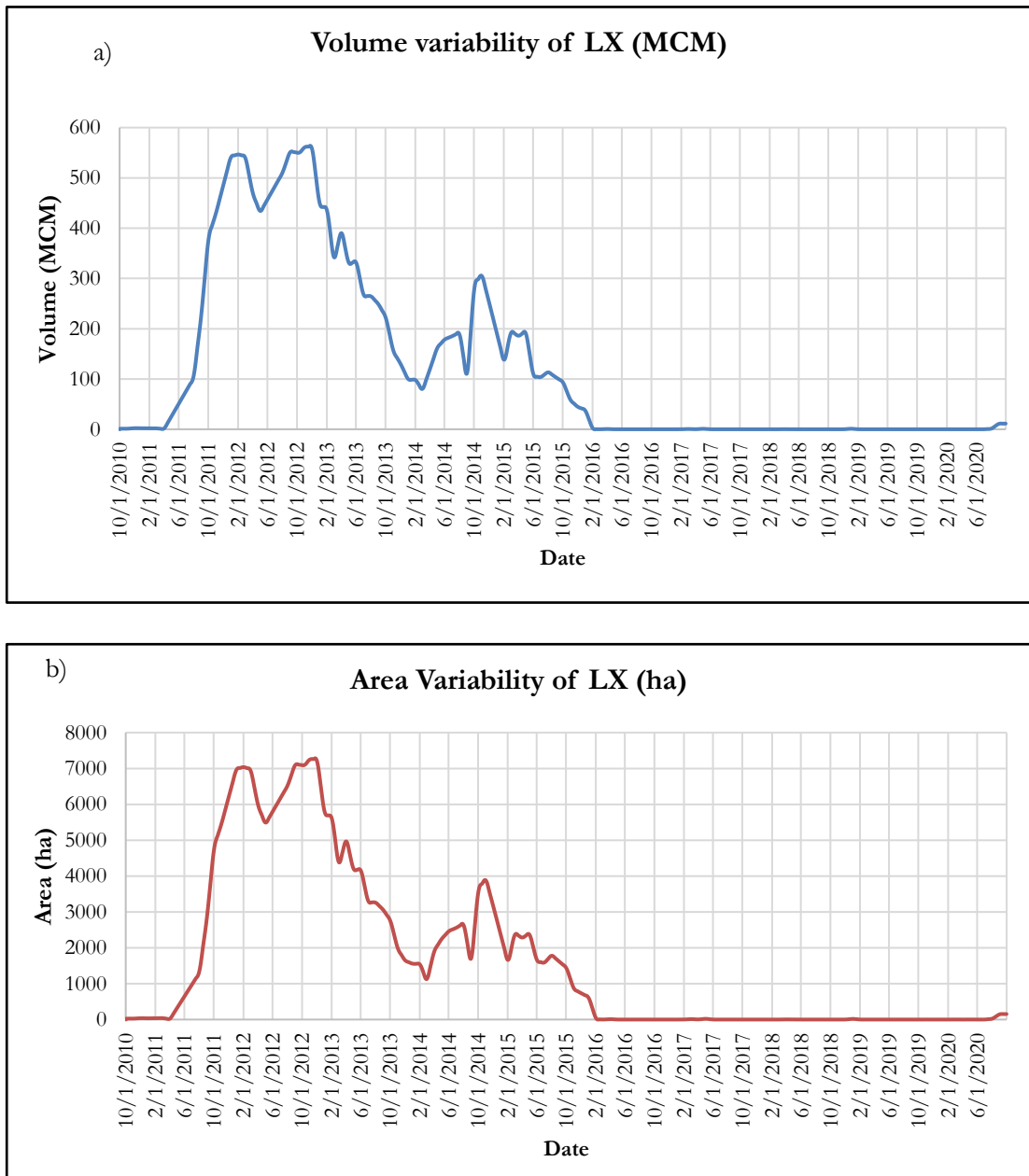


Figure 4-2 Daily volume variability of LX b) daily surface area variability of LX

In the preceding graphs, the general negative trend line equations show that the lake area and volume dropped after 2012, while in the year between 2010 and 2012, both lake area and volume grew. Figure 4-4 depicts the lake surface area for every rainy month of November from 2010 to 2019 and September 2020; this reveals that the surface area of LX rose from 2010 to 2012, then began to decline in 2013, eventually reaching zero in 2016, 2017 and 2018. As a result, LX can be categorized as a non-permanent lake that relies on incoming water through BR.

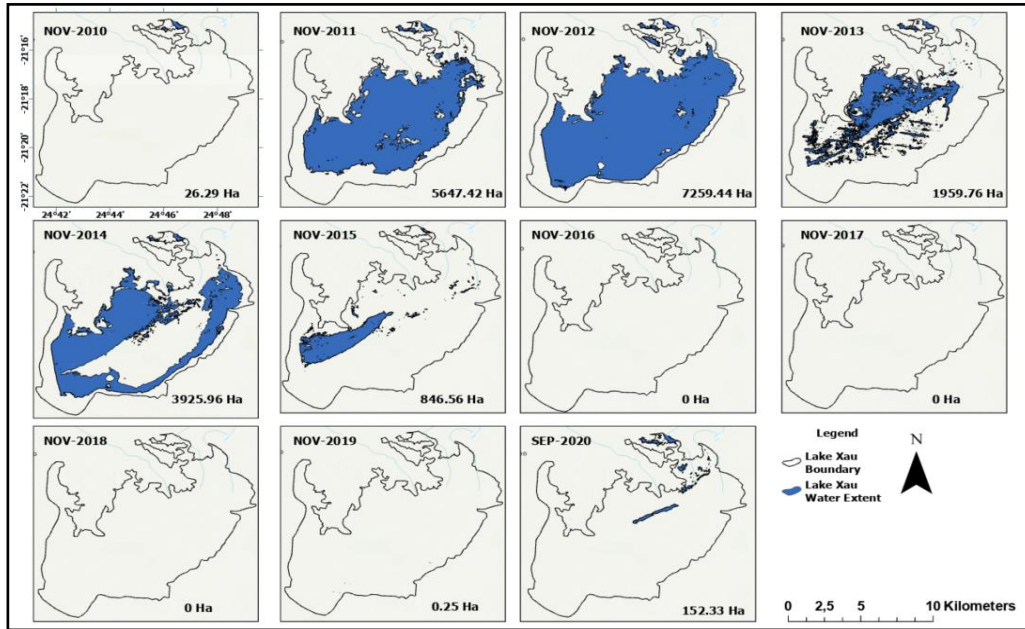


Figure 4-4 Lake Xau areal extent over time; November months are compared as these are yearly periods of typical maximum flows

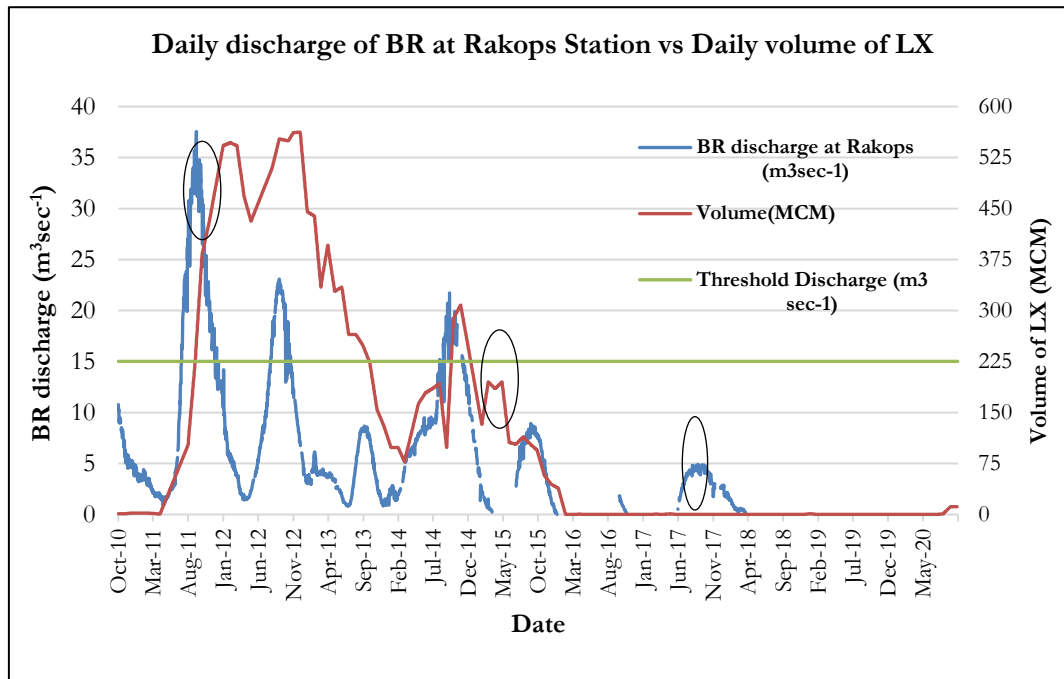


Figure 4-3 Daily discharge of BR at Rakops station vs daily volume of LX

In conclusion, the LX is highly dependent on the flow of BR. Figure 4-3 indicates that the volume of the LX starts to increase when the discharge in BR increases and vice versa. However, since the Rakops gauge station is located ~50 km from LX, the pattern match between the lake surface area and BR discharge has a miss-match, as shown by the oval-shaped circle. The river reaches LX when the discharge of BR at Rakops is above the approximate threshold discharge of 15 m³sec⁻¹. The BR reach peaks in July to November of the year which also affects the peaks of LX to be from July to November.

4.1.2. Lake evaporation

Volumetric evaporation was calculated by multiplying the lake's surface area by the evaporation rate described in Equation 3-18. Figure 4-7 (b) below depicts the daily average temporal variability of the surface area, evaporation rate of LX, and volume of evaporated water between September 2011 to January 2016 (i.e., significant lake extent period). The surface area shows an increase between September 2011 to November 2012; however, after 2012, the lake's surface area started to decrease due to the reduction in rainfall amount upstream of the BRB, which resulted in the reduction of the reduction inflow amount to LX.

Figure 4-5 below shows the instantaneous surface area, WST, net radiation, and daily evaporation of LX on 1st November 2012 (maximum lake extent). On this day, the estimated surface area is 72.48 km², with a WST range of 317.22 to 298.60 K, as shown in Figure 4-5 (a) and (b), respectively. The net radiation is calculated using Equation 3-11, and it ranges between 803.05 to 487.93 Wm⁻², as shown in Figure 4-5 (c). The evaporation rates range between 8.26 to 0.16 mm day⁻¹ Figure 4-5 (d). Appendix-5 also presents the result of DATTUDUT lake evaporation for a small extent of the lake during February 2014.

The daily temporal variability of the lake WST, area, volume and evaporation rate between September 2011 and January 2016 is presented in Figure 4-7.

The temporal variability of the evaporation rate is strongly affected by the annual cycle of WST, as shown in Figure 4-7 (a). The highest WST reaches a peak in the driest seasons of Botswana (May to October), implying the maximum evaporation rate in September (average 4.16 mm day⁻¹). The temporal variability of the volume of evaporated water is dependent on the surface area of the lake's evaporation. For instance, on 1st November 2012, the evaporated volume of water reached 0.35 km³/1000, resulting from an average evaporation rate of 4.78 mm day⁻¹ and surface area of 72.48 km² as indicated in Figure 4-6 below.

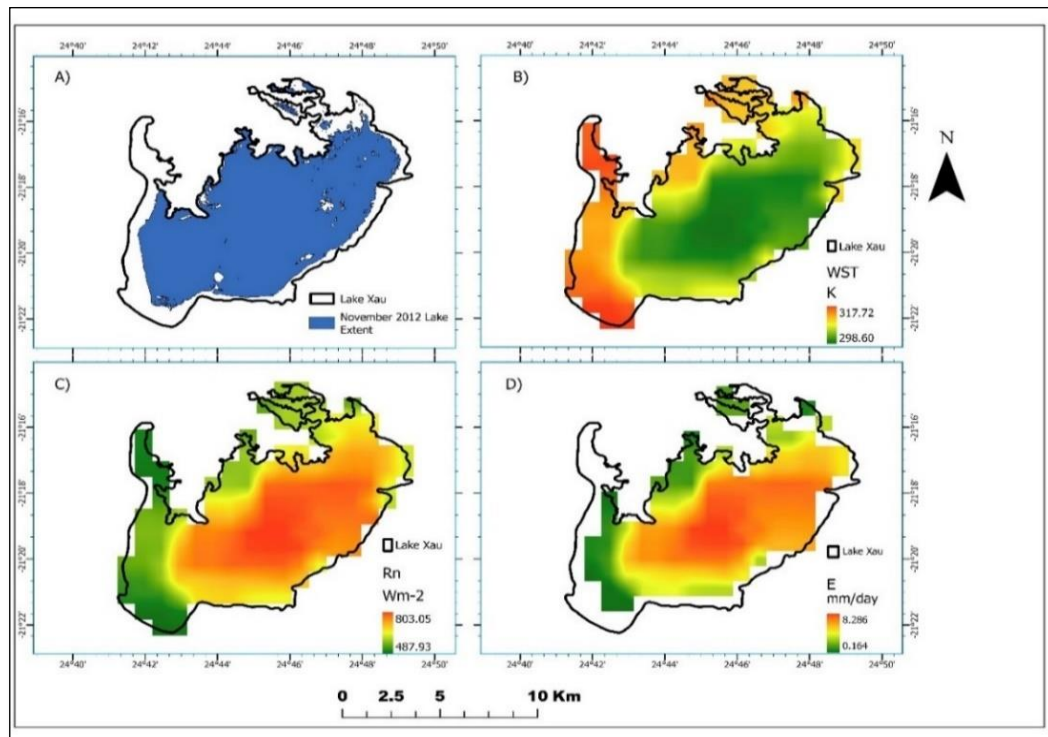


Figure 4-5 a) Surface area b) water surface temperature (WST) c) net radiation (Rn) d) evaporation rate of LX ($E_{L,K}$) on November 1st, 2012

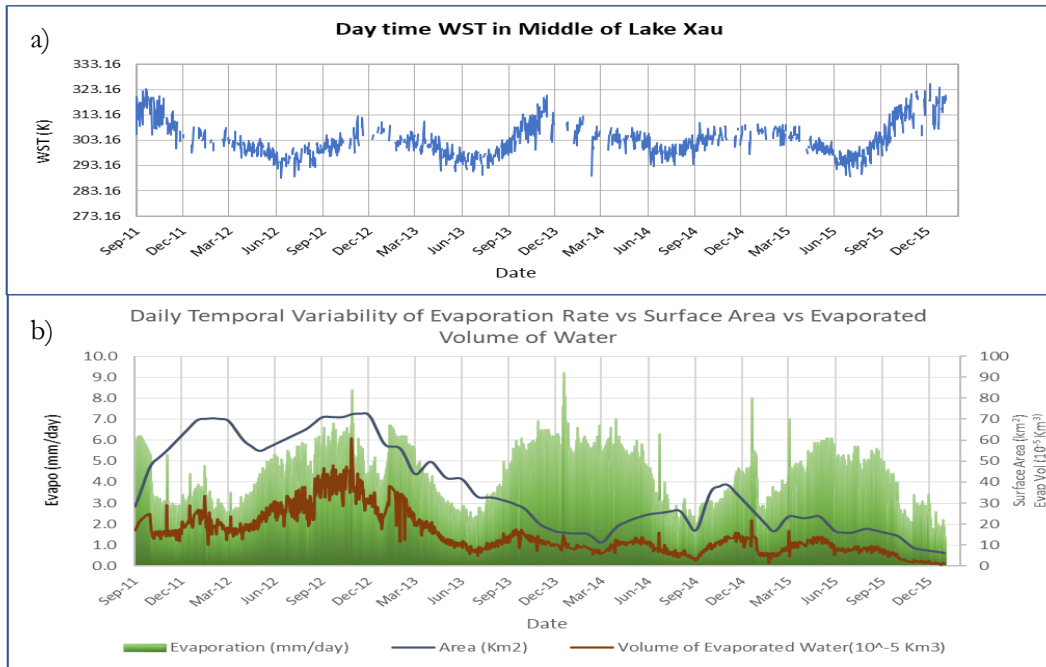


Figure 4-7 a) Daily WST variability in the middle of LX b) daily temporal variability of LX surface area, of evaporation rate and of volume evaporated water

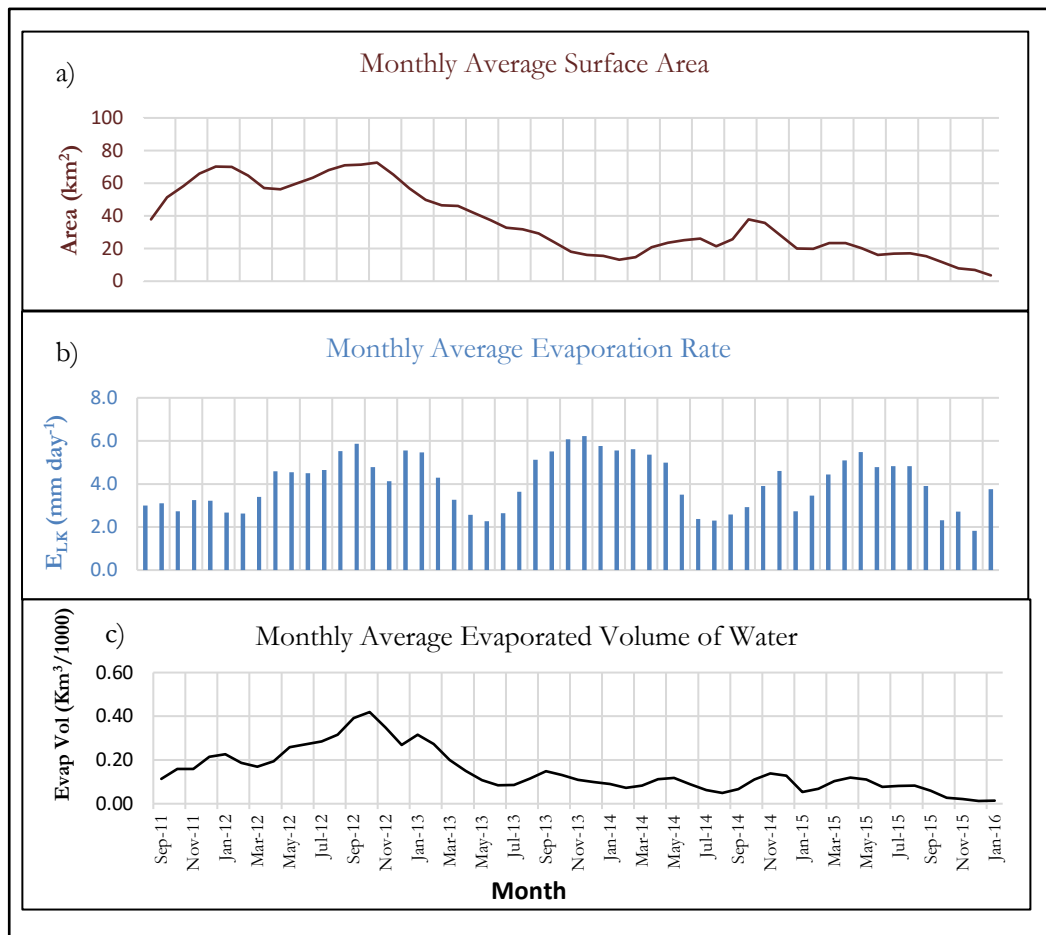


Figure 4-6 a) Monthly average of surface area variability b) daily average evaporation rate c) daily average evaporated volume of water

4.2. Conceptual model

4.2.1. Geological modelling and hydrostratigraphic units

The five-layered hydrostratigraphic units have been identified within the Karoo Super Group and the Pre-Karoo rocks based on stratigraphically analyzing available boreholes in Rockworks. The nomenclature of the five layers adopted from the neighbouring study of Lekula et al. (2018) as Kalahari Sand Unit (KSU), Stormberg Basalt Aquitard (SBA), Lebung Aquifer (LA), Ecça Aquifer (EA) and Ghanzi (GA) where latter in contrast to Lekula et al. (2018) is assumed in this study as impermeable basement. Figure 4-8 and presents spatial distribution of boreholes and of hydrostratigraphic cross-sections, while Figure 4-9 the 5 cross-sections themselves.

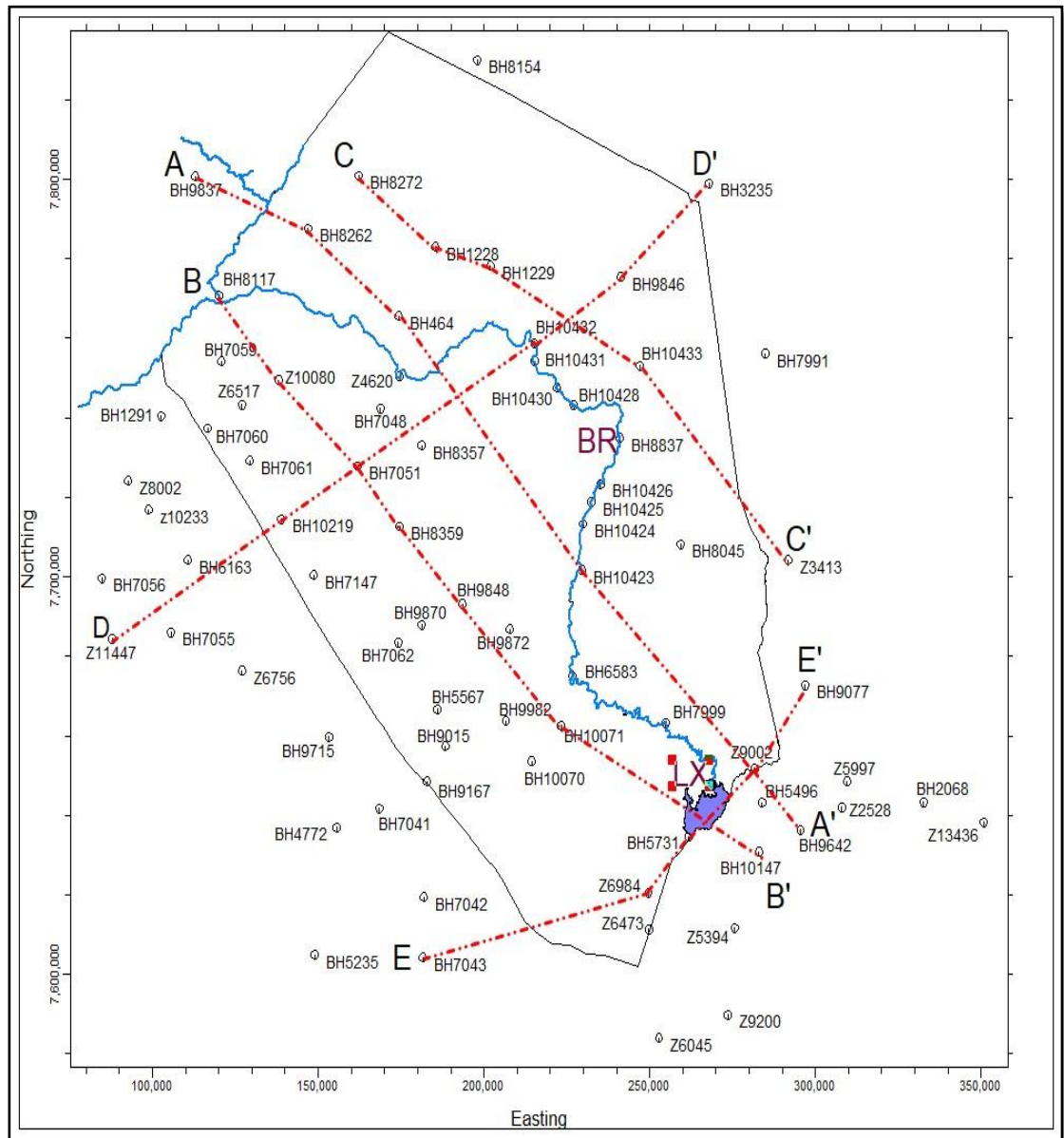


Figure 4-8 Spatial distribution of boreholes used in Rockworks and location of 5 selected hydrostratigraphic cross-sections in BRB

..

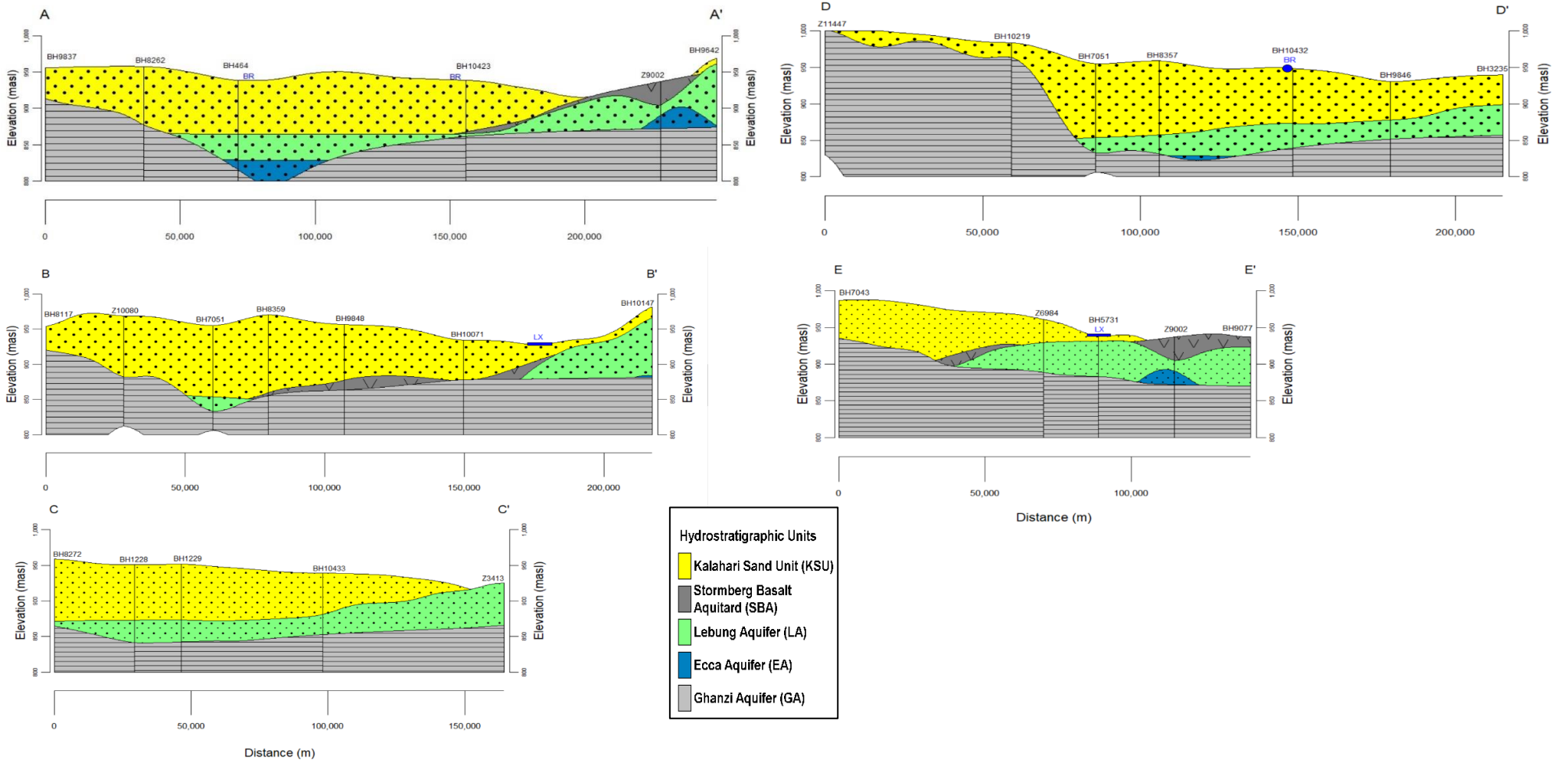


Figure 4-9 Hydrostratigraphic cross-sections locations presented in Figure 4-8 over BRB

From the hydro-stratigraphic cross-section in Figure 4-9, it can be concluded that the KSU and GA cover almost all the study area of BRB whereas the SBA, LA and EA are spatially variability are discontinuous. The SBA presented in cross-sections A-A', B-B' and E-E' is located in the southern and south-eastern part of BRB. The LA appears in all 5 cross-sections, but is present only in the central and eastern part of the study area. EA is the lowest spatially variable hydrostratigraphic unit in BRB. The evidence is that EA is only locally presented on limited amount of boreholes penetrating this unit i.e. BH-464, BH-8357 and Z-9002 only, (see, cross-sections A-A', D-D' and E-E'). As both, the EA and the LA are composed of similar sandstone rocks, and the two are in the direct contact with each other over the entire study area, the two are schematized together as one hydrostratigraphic unit referred as LA+EA.

4.2.2. 3-D hydrostratigraphic model and layer thickness map

3-D hydrostratigraphic model

Rockworks software can also produce a 3-D visualization of hydrostratigraphic layers (Figure 4-10), enabling users to visualize the hydrostratigraphic distribution across their study area. The 3-D model shown below indicates that KSU covers the topmost layer of the BRB area except in the nearby mining areas of Orapa and Lethalkane which located ~ 50 and 250 km, respectively south of Lake Xau. The spatial distribution of SBA, LA and EA is also limited in the 3-D hydrostratigraphic model, as in Figure 4-10. Whereas the bottom layer Ghanzi group fully cover the study area of BRB.

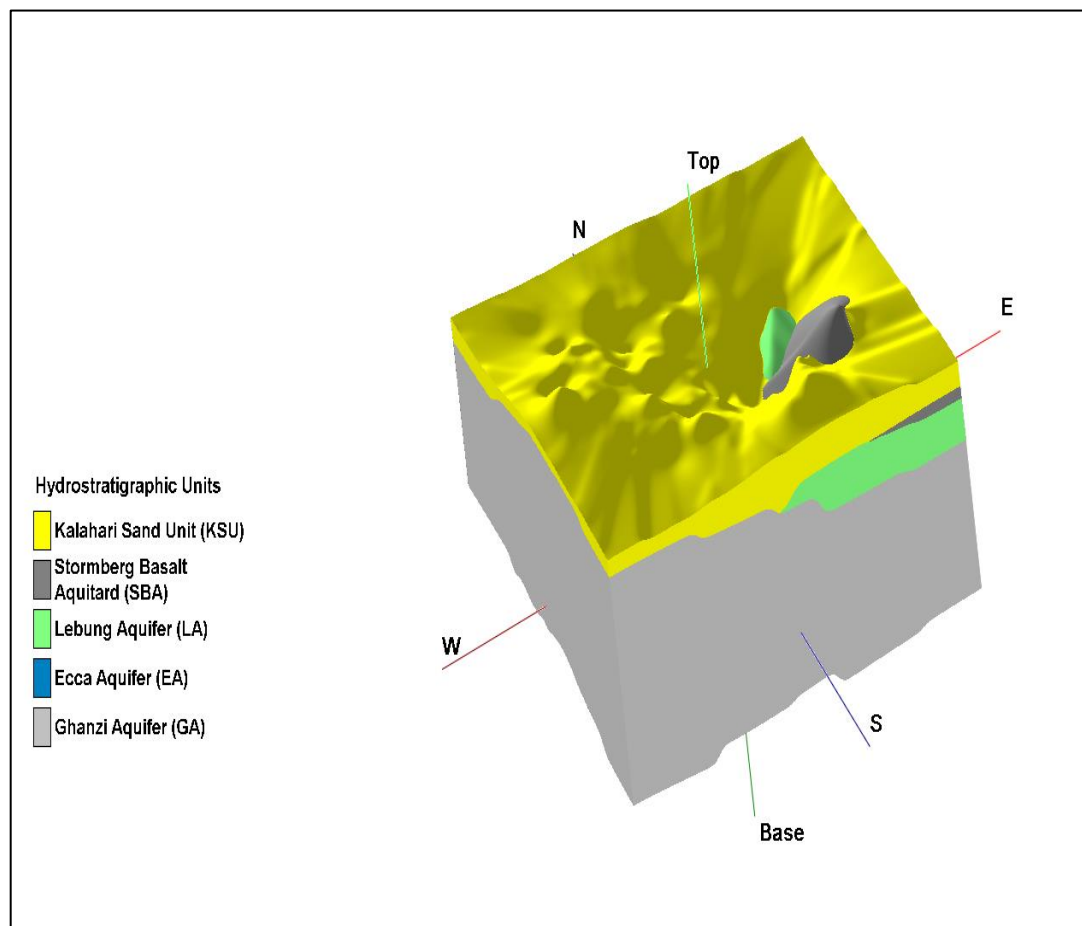


Figure 4-10 3-D-hydrostratigraphic model of BRB

Thickness of hydrostratigraphic layers

Figure 4-11 below shows the spatial distribution of thicknesses of the three hydrostratigraphic units in BRB.

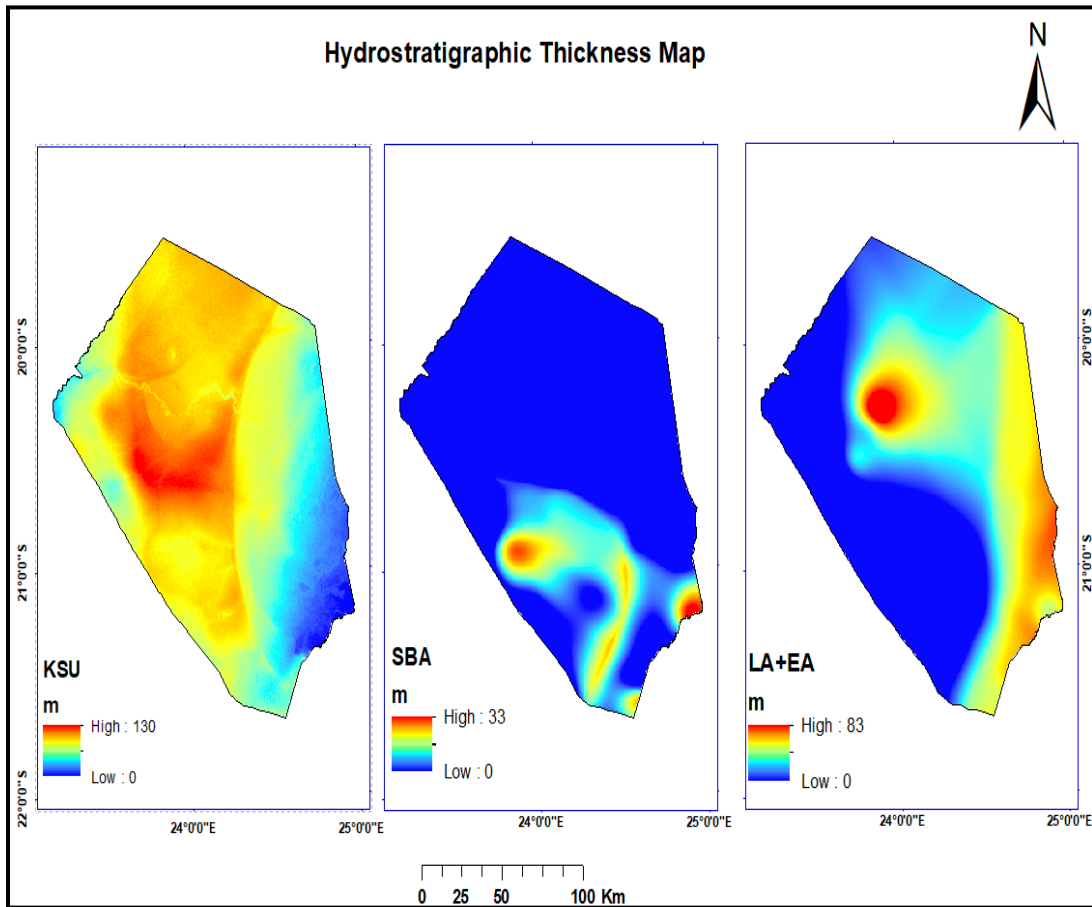


Figure 4-11 Hydrostratigraphic unit layer thickness distribution over BRB

KSU

The KSU is the first layer of BRB covering the whole study area with a maximum thickness of 130 m in the central part of BRB, gradually decreasing to 2 m in the southeast direction. The KSU represents the unsaturated zone aquifer and unconfined aquifer that consists of loose to fine grain sand.

SBA

The SBA is located in the southwest of the study area and its thickness is spatially variable, ranging from 0 to 33 m; due to its basaltic composition, it is considered as an aquitard with very low transmissivity.

LA+EA

The merged layer of LA+EA is the third sandstone layer considered as an aquifer, occurring mainly in the eastern part of the study area, its thickness ranges from 0 to 83 m.

4.2.3. Boundary condition of Boteti River sub-Basin

BRB's external and internal boundary conditions were defined based on the existing physical features and groundwater flow direction as described in section 3.4. For this study, the three-layer system was schematized and imported to the numerical model, as shown in the figure below. The first unconsolidated KSU aquifer and third layer (LA+EA) aquifer has external boundary conditions, whereas the second layer (SBA) was defined as a confined aquitard layer due to no incoming and outgoing water through the layer no flow boundary was assigned..

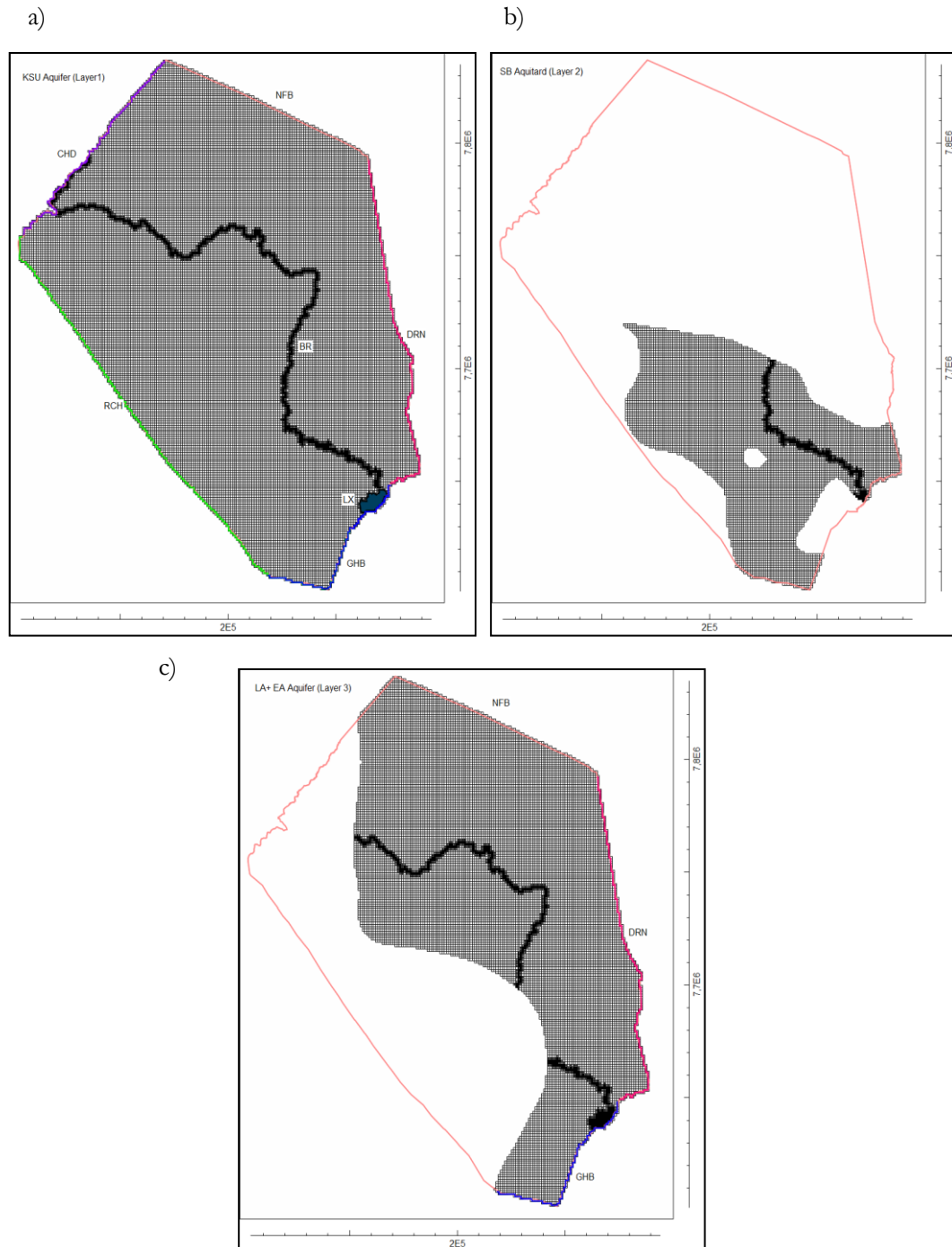


Figure 4-12 Active steady-state model boundary condition of the a) KSU b) SBA and c) LA+EA layer

Schematic diagram and hydrogeological conceptual model

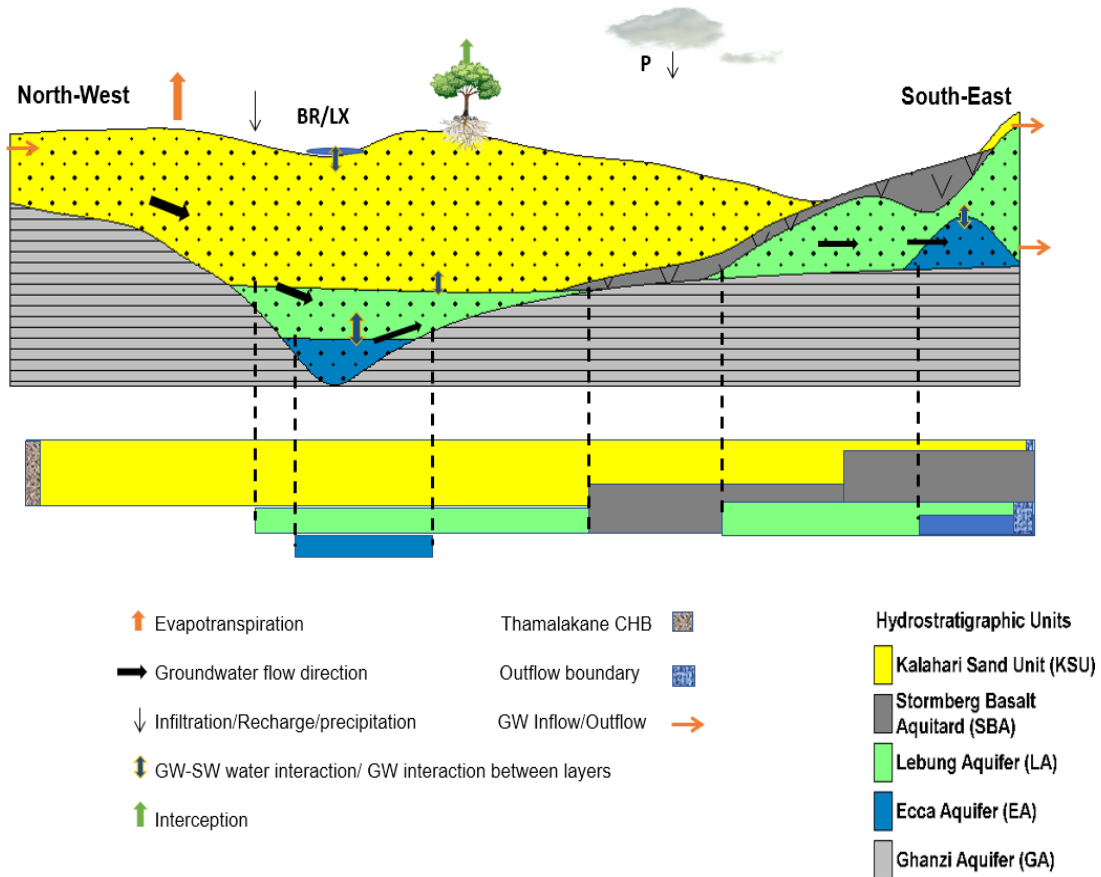


Figure 4-13 Schematic diagram of the hydrogeological conceptual model and numerical model schematization

A diagram above shows the hydrostratigraphic cross-section of the conceptual model and below, the schematic of the proposed into transition numerical model cross-section layout with boundary conditions, the GA is the impermeable basement layer not included in the numerical model.

4.3. Numerical model

4.3.1. Model forcing

4.3.1.1. Effective precipitation

Interception (E_i)

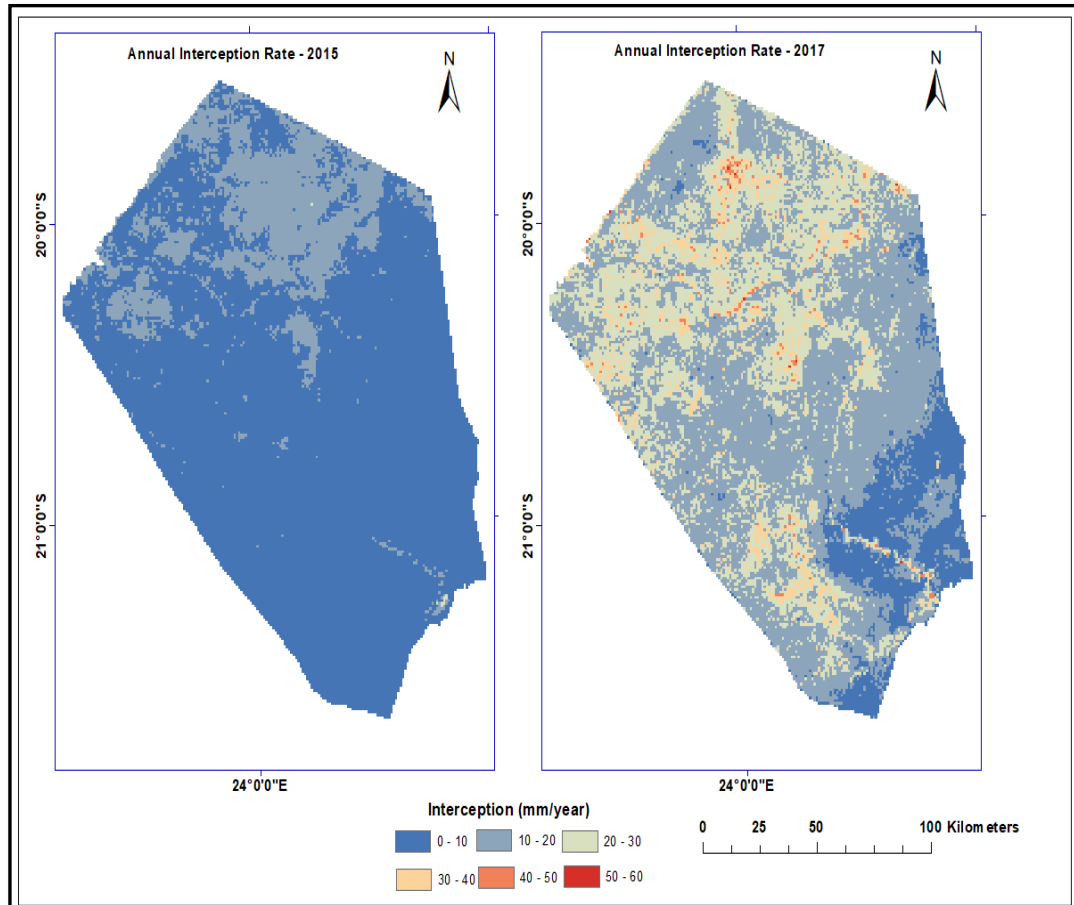


Figure 4-14 Dry and wet average annual interception rate of BRB units(mm yr^{-1})

As the study area is in a semi-arid region, interception is also spatially and temporally variable same as rainfall. Figure 4-14 shows the annual interception loss rate for the dry year of 2015 and the wet year of 2017. Based on visual observation, the interception loss rate is high around the river belt of BR and the northeast part of the study area, where the savannah and big trees are located, as shown in LULC in Figure 2-3. In contrast, the lowest interception rate is in the southeast, southwest, and central part of the study area, where shrubs and grassland are located.

The difference between the dry and the wet years' interception rate is mainly attributed to the annual rainfall difference. In the dry year of 2015, the annual rainfall was 326 mm yr^{-1} , and the respective interception loss ranges between $0\text{-}30 \text{ mm yr}^{-1}$. In contrast, in the wet year of 2017, the annual rainfall was 631 mm yr^{-1} , with a respective annual interception loss range between $0\text{-}60 \text{ mm yr}^{-1}$.

Precipitation (rainfall)

The total annual precipitation (P) rate in the study area over the modelling period ranges from 194 to 631 mm yr⁻¹, as described in Figure 4-16. 2011, 2013, 2014, and 2017 are relatively wet years compared to 2012, 2015, 2016, 2018, 2019, and 2020 since the estimated annual rainfall rate is above 400 mm yr⁻¹. The total annual average precipitation between the year 2010 to 2020 ranges from 272 to 473 mm yr⁻¹ (Figure 4-15). Figure 4-15 depicts that the maximum precipitation occurs in the northeast direction of BRB, whereas the southern part of BRB receives a relatively small amount of precipitation.

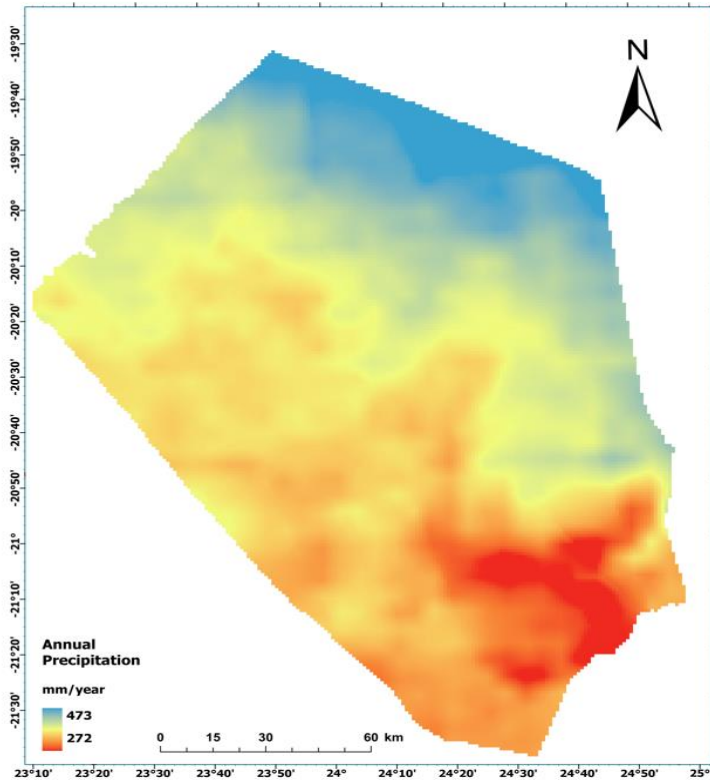


Figure 4-15 Average daily rainfall of BRB between 2010 to 2020 units (mm yr⁻¹)

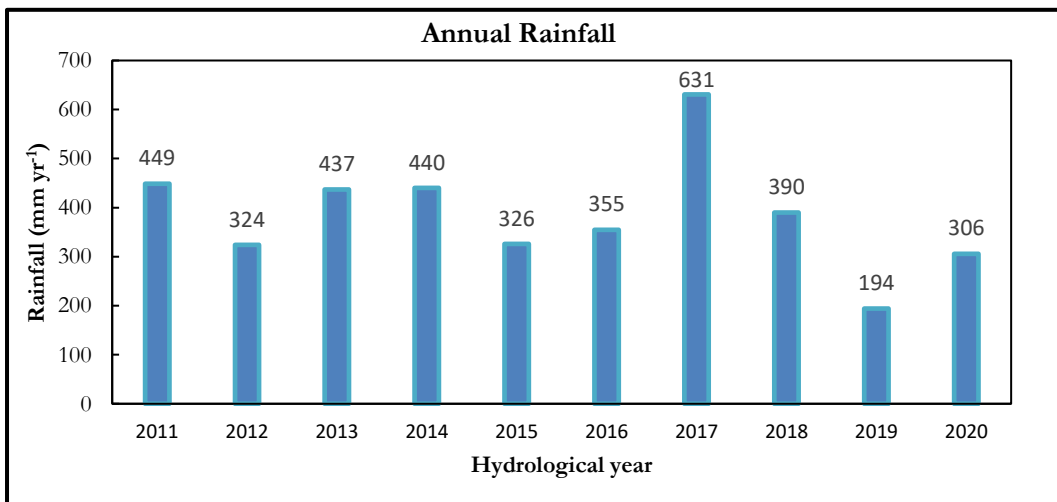


Figure 4-16 Annual rainfall rate over BRB

Effective precipitation (Infiltration rate)

To find the daily spatio-temporally variable effective precipitation (P_e), also known as infiltration rate, the interception loss map is subtracted from the precipitation (rainfall) map as described in section 3.5.3. Figure 4-18 and Appendix-6 shows the annual infiltration loss rate (E_i), daily precipitation (P) and effective precipitation for the selected dry year of 2015 and wet year of 2017. In 2015, the average annual (P) observed by CHIRPS was 252.39 mm yr⁻¹; the annual average annual (E_i) was 6.32 mm yr⁻¹, which resulted in an annual average (P_e) of 245.98 mm yr⁻¹. Whereas in 2017, the average annual P observed by CHRIPS was 562.07 mm yr⁻¹; the annual average (E_i) was 18.24 mm yr⁻¹, which resulted in an average annual (P_e) of 543.48 mm yr⁻¹.

Figure 4-17 shows BRB's annual average precipitation, interception, and effective precipitation rate of BRB over 10 years. The figure depicts that the annual interception rate over BRB is low, which is attributed to low vegetation cover. BRB's average precipitation rate is 369 mm yr⁻¹ (1.01mm day⁻¹). The average interception rate is 9 mm yr⁻¹ (0.025 mm day⁻¹), taking 2.43% of the total rainfall.

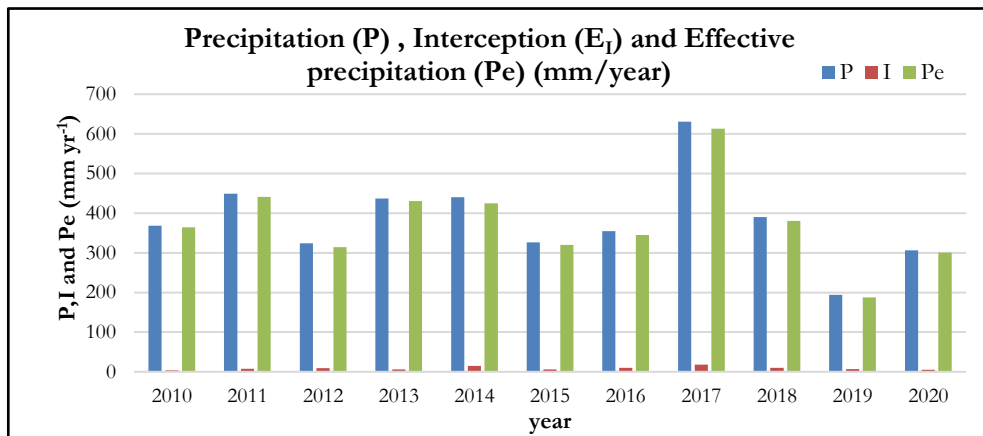


Figure 4-18 Annual precipitation(P), interception(E_i), and effective precipitation(P_e) units (mm yr⁻¹)

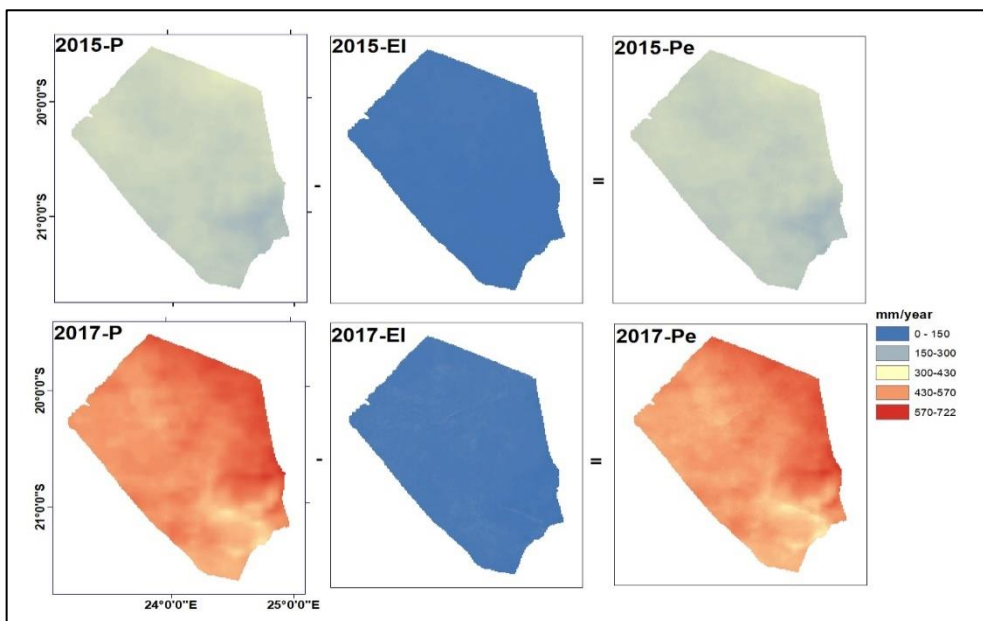


Figure 4-17 Annual precipitation(P), interception (E_i) and effective effective precipitation (P_e) in dry year of 2015 and wet year of 2017 units (mm yr⁻¹)

4.3.1.2. Potential evapotranspiration (PET)

Figure 4-20 below shows the annual PET of BRB over the modelling period of 1st October 2010 to 30th September 2020. The spatial variability of average annual PET in the study area is low (i.e., 3049 to 2362 mm yr⁻¹). The minimum, maximum and average PET plot in Figure 4-20 also suggests a small daily variability of PET. The maximum PET was recorded in December, and the 10-year average annual PET rate is 2819 mm yr⁻¹.

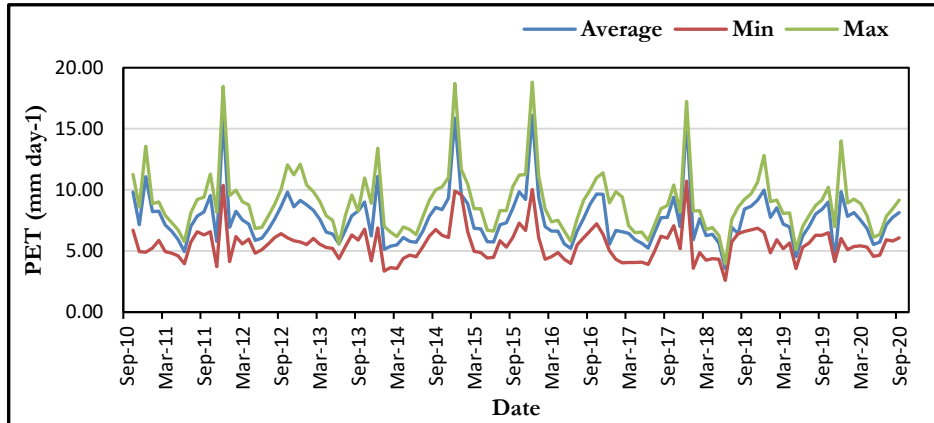


Figure 4-20 Monthly average minimum, maximum and average PET of BRB

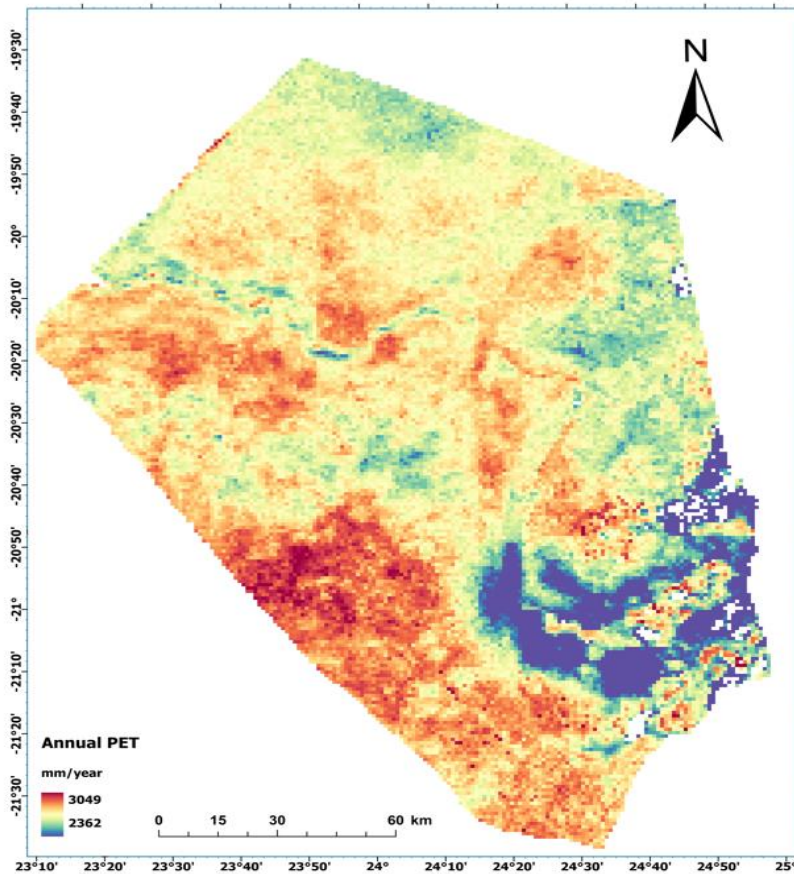


Figure 4-19 Average daily PET from 1st October 2010 to 30th September 2020 units (mm yr⁻¹)

4.3.2. Steady-state model calibration

The steady-state model calibration addresses the calibration of system parameters and boundary conditions of the model area.

4.3.2.1. Calibrated heads

Table 4-1 shows; the observed heads, the steady-state simulated heads, and calculated residuals of each observation point. The mean error (ME), mean absolute error (MAE), and root mean square errors (RMSE) are calculated by Equation 3-45, 3-48 and 3-49, respectively. The calculated values are -0.68, 0.77, and 0.96 m, respectively. The largest residual error is equal to -2.49 m at BH-7952. A scatter plot of the measured versus simulated heads for 25 observation points at the KSU layer is shown in Figure 4-22, with deviation points distributed evenly on either side with an R^2 value of 0.995. Figure 4-21 depicts a histogram showing the frequency of residual error for each of the residual classes. A conclusion that can be drawn from Figure 4-22 is that the maximum calibrated head residual head frequency occurs in the smaller residual errors value, indicating that the calibration was sufficient for matching the observed heads.

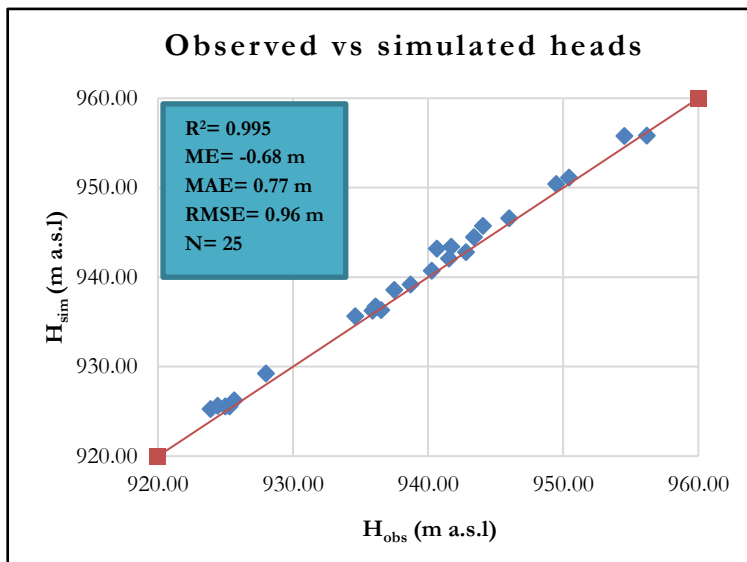


Figure 4-21 Steady state observed vs simulated heads

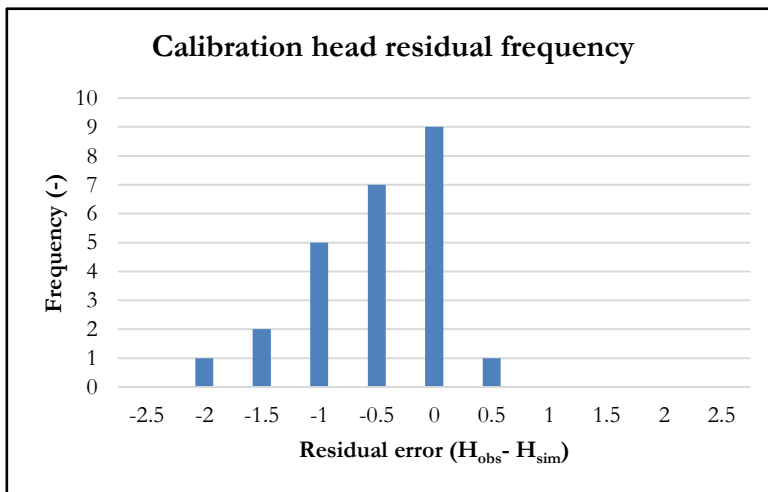


Figure 4-22 Residual frequency of observation points on steady-state model

Table 4-1 Error assessment of heads after steady-state model calibration in BRB

BH-ID	X	Y	DEM ALOS	H _{obs}	H _{sim}	H _{obs} - H _{sim}	Absolute error	Squared error
	m	m	m (a.m.s.l)	m (a.m.s.l)	m (a.m.s.l)	m	m	m ²
BH-1317	156165.31	7818211.82	960	935.90	936.23	-0.33	0.37	0.11
BH-1403	144846.67	7803855.95	959	949.50	950.36	-0.86	0.91	0.73
BH-1757	241681.40	7737846.35	944	937.50	938.52	-1.02	1.25	1.04
BH-8272	162210.99	7800871.29	964	956.20	955.32	0.88	0.16	0.78
BH-9025	173413.46	7752380.28	952	944.06	945.69	-1.63	0.97	2.67
BH-9542	254062.97	7662994.06	929	923.90	925.29	-1.39	1.60	1.92
BH-9576	247249.03	7664387.05	929	925.66	926.24	-0.58	0.80	0.34
BH-9616	259965.37	7650491.65	930	925.30	925.54	-0.24	0.57	0.06
BH-8045	259414.58	7708231.17	932	928.00	929.21	-1.21	1.52	1.48
BH-8019	213698.35	7761805.85	947	936.10	936.69	-0.59	0.33	0.35
BH-8281	136820.94	7772096.63	958	950.45	951.10	-0.65	1.62	0.42
BH-7952	192826.18	7759231.81	947	940.65	943.14	-2.49	0.84	6.21
BH-8549	106967.17	7761928.91	956	946.00	946.10	-0.10	0.23	0.01
BH-2534	125832.61	7785292.35	948	943.40	944.09	-0.69	0.95	0.47
BH-1758	231237.72	7764025.64	949	942.80	942.78	0.02	0.28	0.00
BH-8117	120022.02	7770705.09	954	940.27	940.64	-0.37	0.32	0.14
Phudu-BH	230837.34	7768887.08	947	941.55	942.08	-0.53	0.83	0.29
BH-9849	186478.98	7750964.29	949	941.72	943.38	-1.66	0.71	2.76
BH-9544	254058.18	7662781.24	928	924.99	925.52	-0.53	0.79	0.28
BH-9545	254009.53	7662944.24	928	924.43	925.58	-1.15	1.41	1.33
BH-10423	229502.00	7701659.00	940	934.62	935.63	-1.01	1.68	1.02
BH-10424	229998.00	7713322.00	942	936.53	936.32	0.21	0.18	0.05
BH-10425	232361.00	7718824.00	942	936.18	936.62	-0.44	1.20	0.19
BH-10428	227046.00	7743274.00	944	938.71	939.20	-0.49	0.37	0.24
Z-1959	213171.13	7730775.21	963	954.54	954.76	-0.22	0.51	0.05
Sum						-17.07	19.30	22.93
Numerical Statistics						-0.68	0.77	0.96
						ME	MAE	RMSE

The potentiometric map IHM steady-state simulation result is presented below in Figure 4-23. The higher values begin on the north and west sides of the research area, where the terrain elevation is relatively highest a. The southwest corner of the research area contained the lowest groundwater heads, where the ground elevation is relatively lower. As a result, the flow direction shown in Figure 2-6 is consistent with the outcome of the steady-state model.

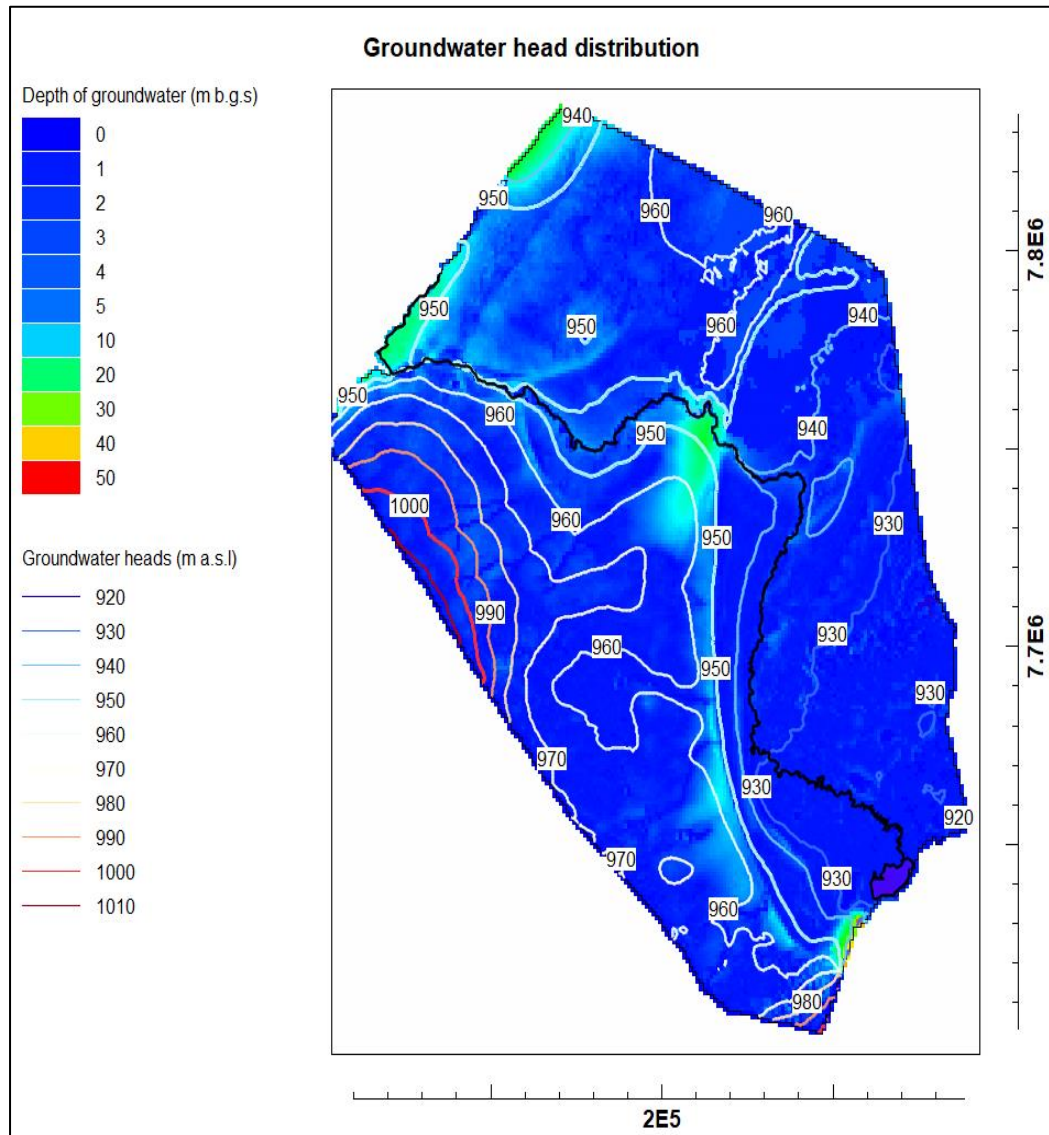


Figure 4-23 Groundwater potentiometric and groundwater table depth map after steady-state model calibration

The colors in Figure 4-23 indicate the groundwater table depth below the ground surface, defined by subtracting the groundwater head from the DEM. The light green spark (i.e., north and middle of BRB) indicates physical features such as the Thamalakane river channel and Gidiwike Ridge. The BR also influenced the groundwater head contours showing there is recharge from the stream to groundwater and discharge from groundwater to streams.

The sharp V-shaped contour lines opposing the river flow while crossing the river indicate the groundwater is moving to the stream channel. In contrast, a U-shaped contour line in the river flow direction indicates the river is recharging water to groundwater. From the visual inspection, the river is recharging water in most of the study, while groundwater discharges near Gidiwike Ridge and the beginning of the river.

4.3.2.2. Calibrated system parameters and boundary conditions

Calibrated hydraulic conductivities

Each layer's horizontal hydraulic (K_h) conductivities were simulated using manual trial and error to attain a sufficient groundwater head match between the observed and simulated heads. After calibration, it is found that upper KSU aquifer layer K_h ranges between 0.01 to 180 $m\ day^{-1}$. Figure 4-24 a) depicts the highest K_h values located in the bright, red-coloured area northeast and southeast of BR. In contrast, the lowest K_h values are located in the green to the yellow colour ranged part, specifically in the western parts of the river and under the lakebed. The river channel of K_h ranges from 25 to 35 $m\ day^{-1}$ from upstream to downstream direction.

The second layer (SBA) K_h distribution value is relatively lower than the first and third layers ranging from $3.1E-05$ to $1E-04\ m\ day^{-1}$. The highest value of K_h is presented in light blue colour with a value of $1E-04\ m\ day^{-1}$. The lowest K_h is presented by blue to dark blue, with a value range of $2.1E-05$ to $3.1E-05\ m\ day^{-1}$. The bottom layer (LA+EA) aquifer ranges from 0.8 to 70 $m\ day^{-1}$ with blue colour for lower K_h and red colour for higher K_h .

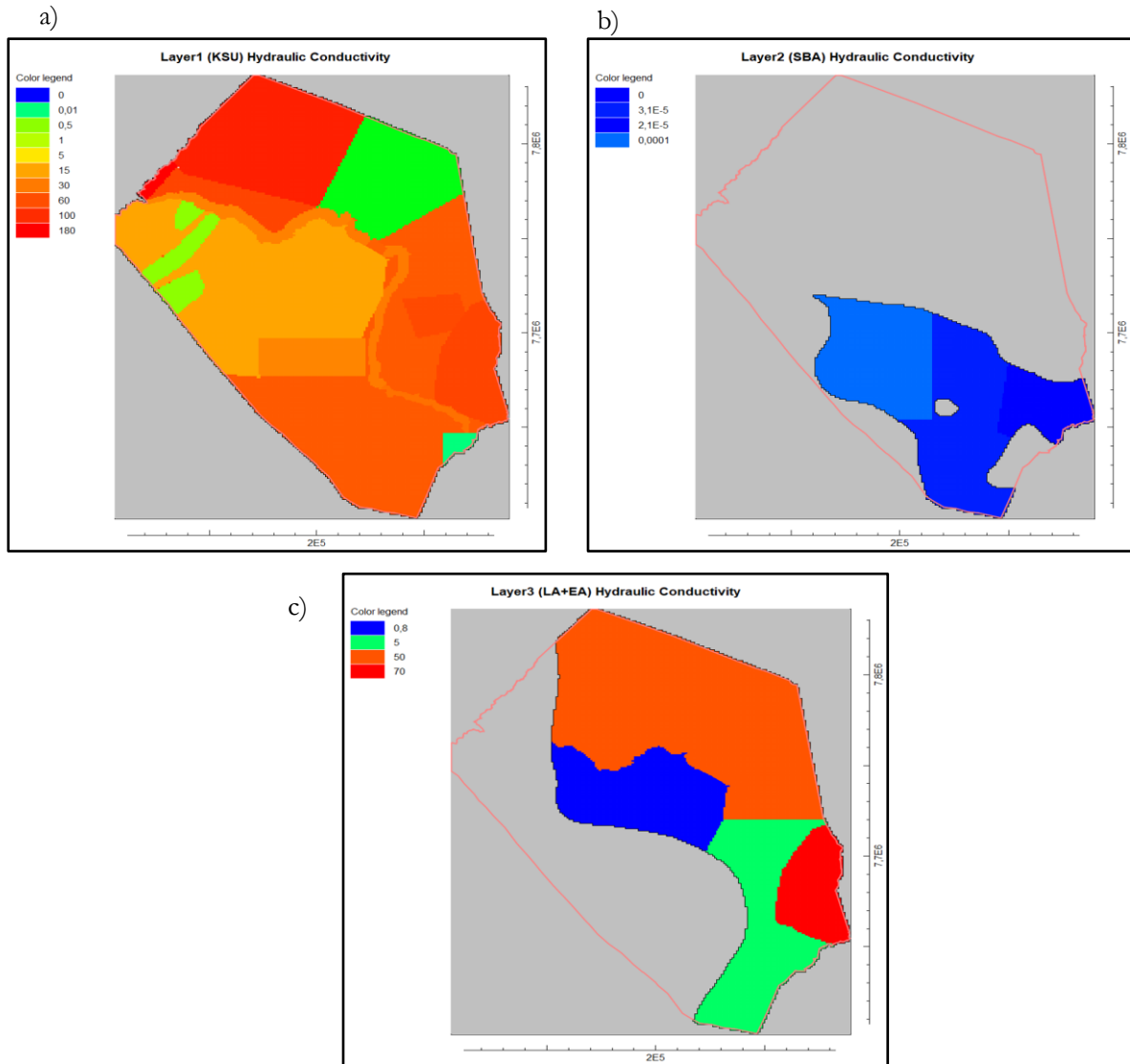


Figure 4-24 Horizontal hydraulic conductivity of a) KSU layer, b) SBA layer, and c) LA+EA layer unit ($m\ day^{-1}$)

Calibrated parameters

The table below shows the calibrated internal and external boundary conditions and the used parameters for simulating the steady state model of BRB.

Table 4-2 Calibrated model parameters

Model package	Parameter	Min	Max	Unit
NPF	K_h	3.1×10^{-5}	180	m day^{-1}
	K_v	$K_h/10$	$K_h/10$	m day^{-1}
GHB	C	0.1	8.1	$\text{m}^2 \text{day}^{-1}$
DRN	C	0.005	0.075	$\text{m}^2 \text{day}^{-1}$
RCH	Specified flux	0.3	0.3	m day^{-1}
SFR	W	10	15	m
	S	1E-04	9E-05	-
	S_{thk}	0.5	1	m
	K_{Sb}	1	1.4	m day^{-1}
	S_{top}	922	956.78	m a.s.l
UZF	d_{surf}	0.2	0.2	m
	K_{sat}	0.09	3.1	m day^{-1}
	θ_{resid}	0.05	0.05	$\text{m}^3 \text{m}^{-3}$
	θ_{sat}	0.35	0.35	$\text{m}^3 \text{m}^{-3}$
	θ_i	0.15	0.15	$\text{m}^3 \text{m}^{-3}$
	θ_{ext}	0.06	0.06	$\text{m}^3 \text{m}^{-3}$
	ε	3.5	3.5	-
	d_{ext}	0	25	m
LAK	K_{Lb}	0.01	0.05	m day^{-1}
	L_{thk}	0.2	0.5	m
	L_{hint}	920	920	m a.s.l
	L_{hbot}	913	913	m a.s.l
	Leakance	0.05	0.1	day^{-1}
MVR	β	1.0	1.0	-

Calibration of stream measurement

The calibration of stream flow was performed by taking the average 10-year measurement of the daily stream discharge record of the Rakops gauging station and comparing it with the observation result assigned on the model. However, comparing the simulated discharge ($191887.28 \text{ m}^3 \text{ day}^{-1}$) with the average discharge measurement at the gauging station ($374565.36 \text{ m}^3 \text{ day}^{-1}$), the simulated model result underestimated observed discharge reached 51.2 % of the observed flow. However, since the developed model is in a steady state, the stream flow calibration is challenging to achieve a high percentage of match between simulated and observed discharge rates.

4.3.2.3. Spatial variability of groundwater recharge and evapotranspiration

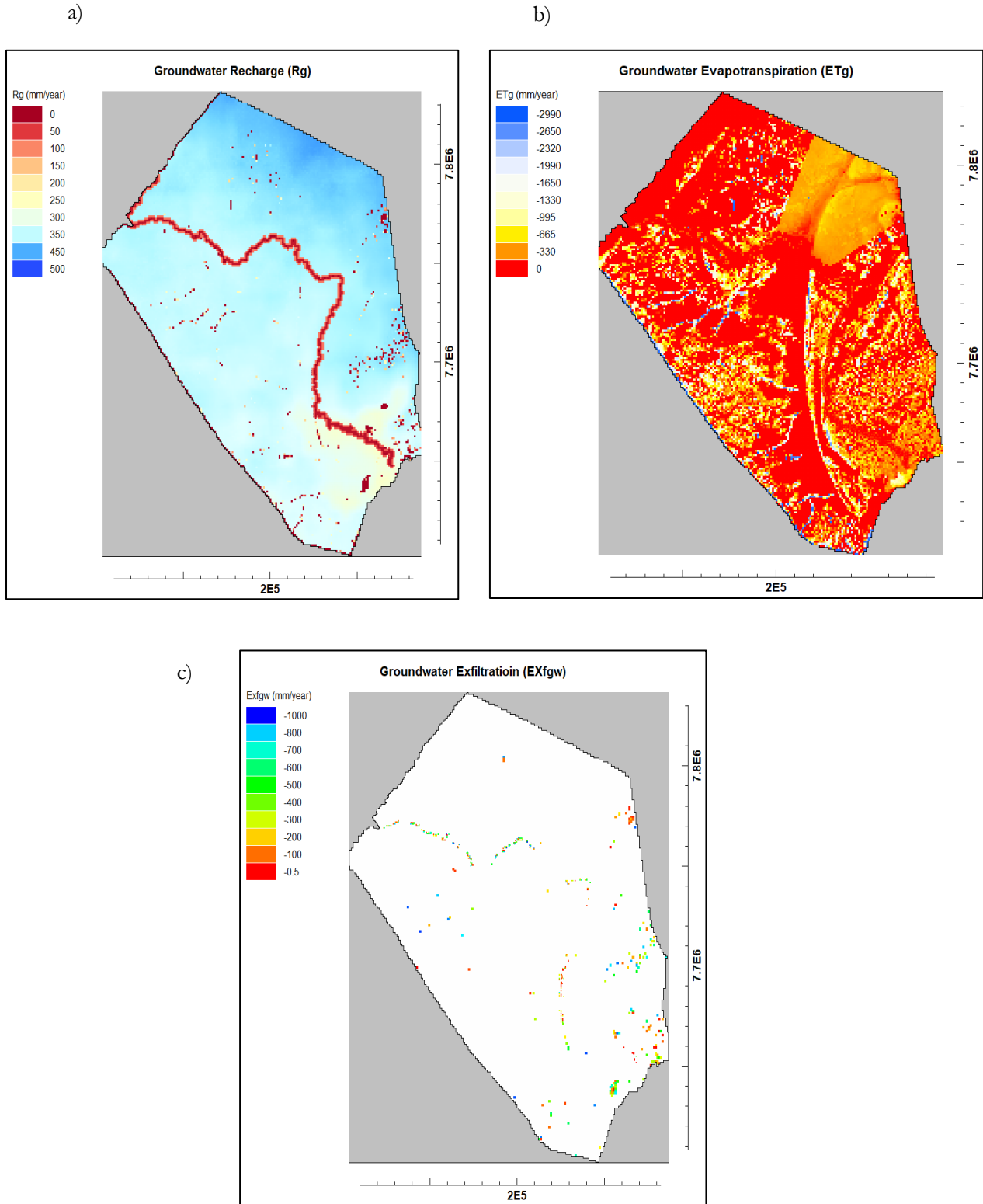


Figure 4-25 Spatially variable maps of a) groundwater recharge (R_g), b) groundwater evapotranspiration (ET_g), and c) groundwater exfiltration (EX_{fgw}) for steady-state IHM in BRB units (mm yr^{-1})

The spatial variability of groundwater fluxes mainly consists of groundwater recharge (R_g) and groundwater evapotranspiration (ET_g), and groundwater exfiltration (Exf_{gw}). Figure 4-25 and above presents the spatial variability of R_g , ET_g and Exf_{gw} over the steady-state model calibration.

Figure 4-25 a) represents the gross groundwater recharge (R_g). The maximum R_g (440 mm yr^{-1}) is higher in the north-eastern part of the study area, where there is high rainfall, as shown in Figure 4-15. The lower R_g value is found in some cells and the riverbed area, in small cells with a recharge boundary, general head boundary and water table near the land surface exist.

Figure 4-25 b) shows the spatial variability of ET_g calculated by the UZF package. The value of ET_g ranges from 0 to $-2990 \text{ mm day}^{-1}$. The negative value indicates that water is subtracted from the groundwater budget. Compared to Figure 4-19, the model ET_g shows a similar representation of evapotranspiration of BRB. The minimum value of ET_g is shown in bare soil and water areas with small extinction depths. The higher value is found in higher extinction depth areas with big trees and forests.

Figure 4-25 c) shows the spatial variability of Exf_{gw} calculated by the UZF package. The value ranges from -0.5 to -1000 mm yr^{-1} . The negative value indicates the water is exfiltrating from the groundwater.

The steady-state model's net recharge (R_n) can be calculated by adding the R_g with ET_g groundwater exfiltration (Exf_{gw}) as per Equation 3-26. Figure 4-26 shows the spatial distribution of R_n ranging from -900 mm yr^{-1} to 900 mm yr^{-1} .

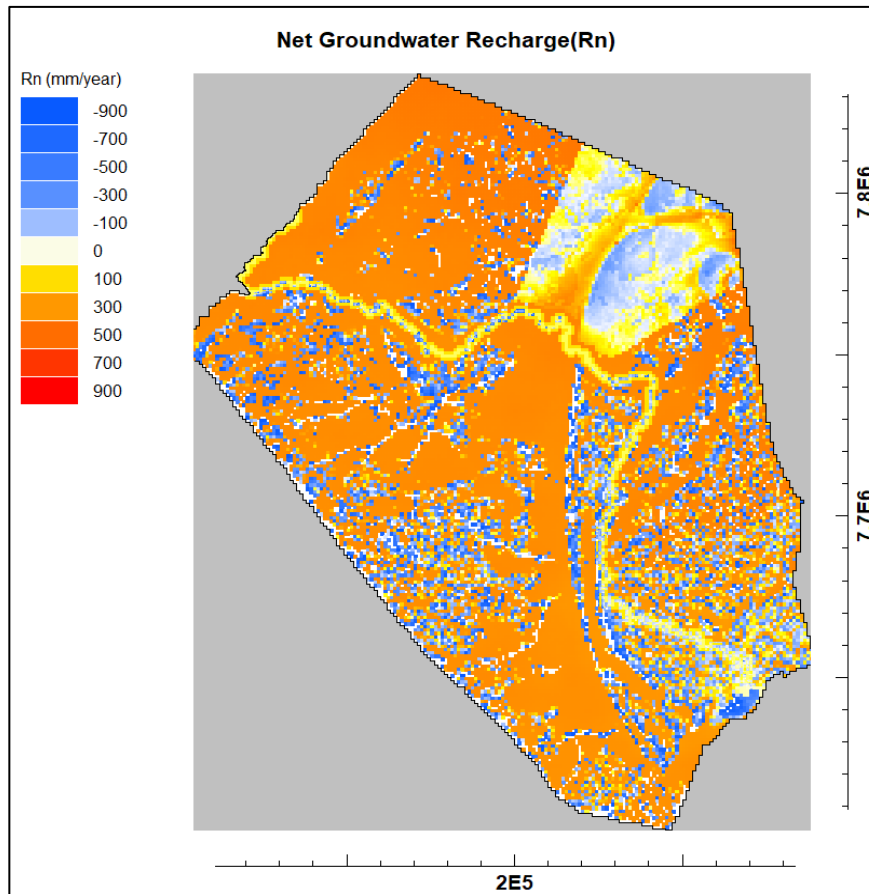


Figure 4-26 Spatial distribution of net groundwater (R_n) units (mm yr^{-1})

4.3.2.4. Water balance of the steady-state model

The water balance of the BRB is presented below in three different ways: 1) water balance of the entire model, 2) water balance of land surface and unsaturated zone, and 3) water balance of saturated (groundwater) zone.

Water balance of the entire model

The yearly average entire water balance of BRB was calculated based on Equation 3-17 to 3-22, and the result is presented in Table 4-3. The percentage contribution of each outflow component in terms of total outflow is groundwater evapotranspiration (ET_g) 84.98%, lateral groundwater outflow (Q_{Lout}) 12.72%, canopy interception loss (E_I) 1.72 % and lake evaporation (E_{Lk}) 0.39%. Whereas the percent contribution of each inflow component as a percentage of total inflow to the entire system is precipitation (P) 69.87%, lateral groundwater inflow (Q_{Lin}) 27.68%, and stream inflow (q_{in}) 2.45 %.

Table 4-3 Total water balance of BRB at steady-state IHM

Inputs Components	In (m^3day^{-1})	% Total	Output components	Out (m^3day^{-1})	%Total
Precipitation (P)	26473034.91	69.87	Groundwater evapotranspiration (ET_g)	31907141.69	84.98
Stream inflow (q_{in})	924314.70	2.45	Canopy interception loss (E_I)	645683.78	1.72
			Evaporation of lake (E_{Lk})	144734.435	0.39
			Total ET	32697559.90	86.3
Lateral groundwater inflow (Q_{Lin})	$Q_{GHBin} = 44773.27$	0.12	Lateral groundwater outflow (Q_{Lout})	$Q_{DRNout} = 711788.71$	1.90%
	$Q_{CHDin} = 815032.06$	2.15		$Q_{CHDout} = 1932430.45$	5.14
	$Q_{RCHin} = 9630000.00$	25.41		$Q_{GHBout} = 2202256.05$	5.87
	Total $Q_{Lin} = 10489805.33$	27.68		Total $Q_{Lout} = 4846475.21$	12.91
Total	$37887154.93 = 528.10 \text{ mm yr}^{-1}$			$37544035.11 = 523.31 \text{ mm yr}^{-1}$	
Inflow-Outflow					343119.83
% Discrepancy					0.905%

Water balance of land surface and unsaturated (vadose) zone

The water balance of the unsaturated zone and land surface of BRB was calculated by Equation 3-23. Table 4-4 below presents the average yearly water balance of the unsaturated zone and land surface. The effective precipitation (P_e) contributes 100% of the total inflow to the unsaturated zone of BRB, 98.04% turn to gross recharge (R_g), and 1.98% is rejected infiltration (RI).

Table 4-4 Water balance of land surface and unsaturated zone

Inflow	In ($mm \text{ yr}^{-1}$)	%Total	Outflow	$mm \text{ yr}^{-1}$	% Total
Effective precipitation (P_e)	360.00	100%	Gross recharge (R_g)	352.96	98.26
			Rejected infiltration	6.33	1.74
Total	360.00			359.29	
In-Out					0.71
% Discrepancy					0.19%

Water balance of groundwater (saturated) zone

The average yearly groundwater (saturated) water balance was calculated based on Equation 3-25. The percentage of each water balance component as percent of total inflow to the saturated zones is 67.53% gross recharge (R_g); 27.98% lateral groundwater (Q_{Lin}); 4.20% stream leakage to groundwater (q_{sg}); and 0.29% lake leakage to groundwater (L_{LKin}). Whereas the percentage of outflow components as percent of total outflow from the saturated zone are 61.44% groundwater evapotranspiration (ET_g); 23.65% groundwater exfiltration (Exf_{gw}); 12.92% lateral groundwater outflow (Q_{Lout}); and 1.99 % groundwater leakage to stream (q_{gs}). The table below describes the inflow and outflow of the groundwater budget of BRB.

Table 4-5 Water balance of groundwater (saturated) zone

Inflow components	In (mm yr ⁻¹)	% Total	Outflow components	Out (mm yr ⁻¹)	%Total
Gross recharge (R_g)	352.96	67.53			
Lateral groundwater inflow (Q_{Lin})	146.28	27.98	Lateral groundwater outflow (Q_{Lout})	67.55	12.92
			Groundwater evapotranspiration (ET_g)	321.14	61.44
Lake leakage to groundwater (L_{LKin})	1.43	0.29	Groundwater leakage to the lake (L_{LKout})	0	
			Groundwater exfiltration (Exf_{gw})	123.61	23.65
Stream leakage to groundwater (q_{sg})	21.97	4.20	Groundwater leakage to stream (q_{gs})	10.34	1.99
Total	522.64			522.64	
In - Out					0
(%) Discrepancy					0

4.3.2.5. Lake budget

Table 4-6 shows the total water balance in LX over the steady-state IHM and calculated based on Equation 3-24. The table assessment error and percentage discrepancy value indicate that the model is within an acceptable limit (< 1%). In this water balance, all the input values for simulating the lake were taken as average as described in the LAK package in section 3.6.2.1. The evaporation of the lake ($E_{L,k}$) extracts a larger portion (60%) of lake volume. The lake leakage also takes out 40% of lake volume. The final simulated lake stage is 919.68 m a.s.l which is relatively close to the average lake stage imported to the whole model period (920 m a.s.l). The maximum lake surface area (A_L) of 69 km² was used to convert the simulated volume-based water balance of the lake into annual average fluxes.

Table 4-6 Water balance of Lake Xau at steady-state IHM

Lake budget components	In (mm yr ⁻¹)	Out (mm yr ⁻¹)
Precipitation (P)	490.33	
Lake evaporation ($E_{L,k}$)		766.15
inflow to the lake(q_L)	820.26	
Groundwater seepage ($L_{L,k}$)		544.45
Total	1310.59	1310.60
In-Out		
	-0.013	
Percentage Discrepancy (%)	0	

4.3.2.6. Lake seepage

Figure 4-27 shows the spatial distribution of lake seepage across the bottom of LX. All the positive values indicate that the LX is seeping water into the groundwater aquifer. The highest seepage rate is in the central and southwestern parts of LX, where the lake is relatively deep and groundwater is shallow. In contrast, the lake entrance and boundary have a lower seepage rate since the lake is shallow and the groundwater is relatively deep in this area.

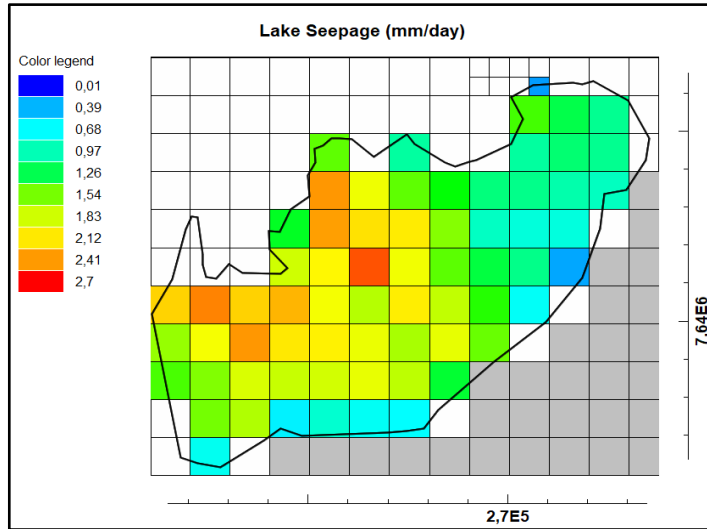


Figure 4-27 Distribution of lake seepage units (mm day^{-1})

4.3.2.7. Layer budget

ZONEBUDGET package can also produce the groundwater budget for selected areas of interest. The water balance was subdivided for each layer by defining three zones for each model layer (KSU aquifer = Zone1, SBA aquitard = Zone2 and LA+EA aquifer = Zone3). Table 4-7, Table 4-8 and Table 4-9 are the final water budget for layer-1, layer-2, and layer-3, as calculated by Equation 3-40 to 3-44. El-Zehairy et al. (2018) reported that the ZONEBUDGET software results are slightly different from the total water budget presented by MODFLOW since the ZONEBUDGET uses only cell-by-cell flow to calculate the budget.

Table 4-7 KSU aquifer (layer-1) groundwater budget

WB components	In (mm yr^{-1})	WB components	Out (mm yr^{-1})
Gross recharge (R_g)	352.96	Groundwater evapotranspiration (ET_g)	321.14
Lateral groundwater inflow (Q_{Lin})	147.07	Lateral groundwater outflow (Q_{Lout})	55.14
Lake leakage (L_{Lkin})	1.43		
		Groundwater exfiltration (Exf_{gw})	123.61
Stream leakage (q_{sg})	21.97	Stream leakage (q_{gs})	10.34
q_{v2-1}	0.004	q_{v1-2}	0.16
q_{v3-1}	26.96	q_{v1-3}	39.97
Total	550.394	Total	550.36
In - Out			0.03
% Discrepancy			0.01

Table 4-8 SBA aquitard (layer-2) groundwater budget

WB components	In (mm yr ⁻¹)	WB components	Out (mm yr ⁻¹)
q_{v1-2}	0.16	q_{v2-1}	0.004
q_{v3-2}	0.004	q_{v2-3}	0.16
Total	0.164	Total	0.164
In - Out			0.00
(%) Discrepancy			0.00

Table 4-9 LA+EA aquifer (layer-3) groundwater budget

WB components	In (mm yr ⁻¹)	WB components	Out (mm yr ⁻¹)
Lateral groundwater inflow (Q_{Lin})	0.46	Lateral groundwater outflow (Q_{Lout})	13.65
q_{v1-3}	39.97	q_{v3-1}	26.96
q_{v2-3}	0.16	q_{v3-2}	0.004
Total	40.29	Total	40.61
In - Out			-0.324
(%) Discrepancy			0.8

The following schematic block diagram shows the inflow and outflow water balance in the BRB aquifer system as calculated by Equation 3-40 to Equation 3-44.

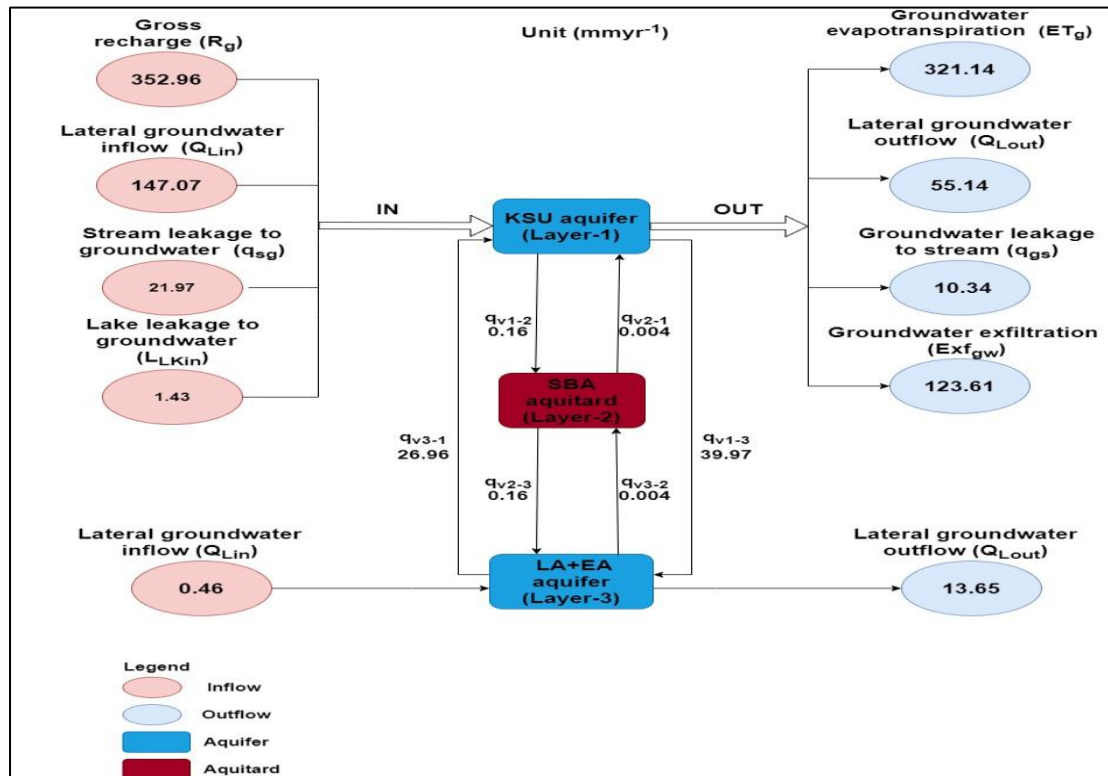


Figure 4-28 Schematic block diagram of water balance exchange between layers within BRB, presented in mm yr⁻¹ as 10-year average steady-state IHM presents

The 10-year annual net recharge value was calculated by Equation 3-26, and it is found that the annual R_n is -91.79 mm yr⁻¹.

4.3.2.8. Sensitivity analysis results

Sensitivity analysis was performed to test the response of the simulated head to the change of horizontal hydraulic conductivity (K_h) of the KSU layer, lakebed leakance ($K/\Delta x$), and hydraulic conductivity of stream beds. Figure 4-29 to 4-31 and Tables 4-10 to 4-12 show the effect of changing K_h , lakebed leakance, and stream bed hydraulic conductivity. From the figures, it can be concluded that the horizontal hydraulic conductivity (K_h) is the most sensitive parameter than the stream bed hydraulic conductivity and lakebed leakance.

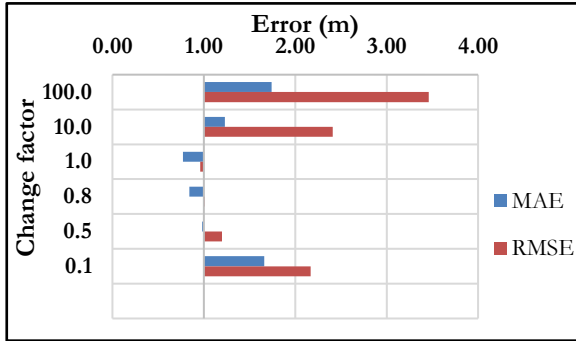


Figure 4-29 Effect of changing K_h on simulated heads

Table 4-10 Changing K_h with factor

Factor	MAE	RMSE
100	1.740	3.46
10	1.23	2.41
1	0.77	0.96
0.75	0.84	1.01
0.5	0.98	1.2
0.1	1.66	2.17

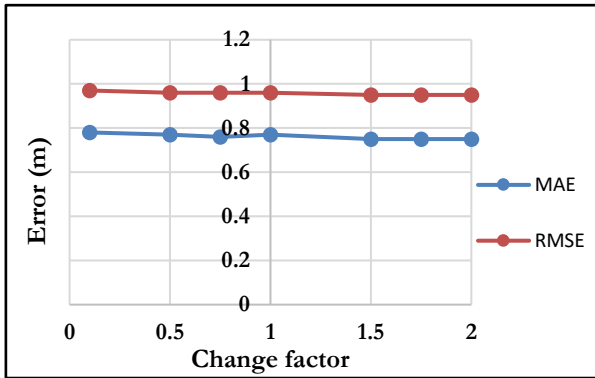


Figure 4-30 Effect of changing lakebed leakance on simulated heads

Table 4-11 Changing leakance with factor

Factor	MAE	RMSE
100	0.71	0.91
75	0.71	0.9
50	0.71	0.9
10	0.71	0.94
1	0.77	0.96
0.750	0.78	0.97
0.500	0.79	0.97
0.100	0.86	1.04

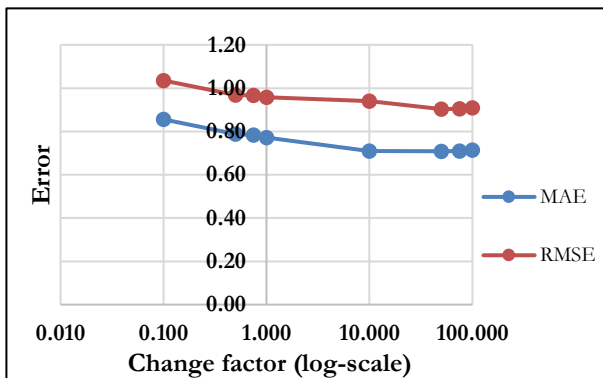


Figure 4-31 Effect of changing streambed K_h on simulated heads

Table 4-12 Changing streambed K_h with factor

Factor	MAE	RMSE
0.1	0.78	0.97
0.5	0.77	0.96
0.75	0.76	0.96
1	0.77	0.96
1.5	0.75	0.95
1.75	0.75	0.95
2	0.75	0.95

5. DISCUSSION

5.1. Hydrogeological conceptual model

One of the most crucial elements in creating a multi-layered groundwater model is the hydrogeological conceptual model (HCM) (Lekula et al., 2018). In BRB, the HCM was developed by analysing the available geological and hydrogeological information using Rockworks software. The developed HCM of BRB identified five hydrostratigraphic units: Kalahari Sand Unit Aquifer (KSU), Stormberg Basalt Aquifer (SBA), Lebung Aquifer (LA), Ecca Aquifer (EA), and Ghazi impermeable layer (GA). However, due to low permeability in the study area, the GA was considered as impermeable basement while the two neighbouring sandstone layers, i.e. LA and EA, were combined together as one aquifer. Finally, the three-layer system consisting of KSU (layer1), SBA (layer2), and LA+ EA (layer3) was converted into the numerical model.

Uncertainty in altitude referencing affects hydrostratigraphic units' development and groundwater heads' interpolation. Since the boreholes are used for measuring the depth of stratigraphic units and groundwater level, high accuracy of reference altitude is essential. For this study, the ALOS PALSAR DEM was used with a reference accuracy of 12.5 m; this affected both the results of hydrostratigraphic units and groundwater head interpolation. When comparing the interpolated groundwater in Figure 2-6 with model output in Figure 4-23, there is a deviation in matching the contour pattern; this indicates that a high certainty altitude reference is needed for interpolating the groundwater heads.

5.2. Remote sensing contribution to IHM

For the development of IHM of BRB, remote sensing (RS) provides daily spatio-temporal data of precipitation, potential evapotranspiration, lake evaporation and AVE curve of Lake Xau (LX).

The CHIRPS data was used for the spatio-temporal data demand of IHM development over BRB. CHIRPS was selected mainly because the Maun rainfall station was used as a blending station to increase the accuracy of CHIRPS. Mitiku (2019) also found out that the uncorrected CHIRPS product has a good correlation with the in-situ measurement of Sexaxa (ORI) station for the selected rainfall value > 0 in the year between 2014 to 2017, as depicted in Figure 3-11. Even though the uncorrected CHIRPS is in good correlation with in-situ measurement, bias correction and validation of CHIRPS are necessary for increasing the accuracy of the IHM model result.

IHM requires PET as the driving force for this study, and the MODIS 8-day lumped PET was used as an input for the IHM. As compared to precipitation, PET is less variable in the area; moreover, the IHM of the study area is less sensitive to changes in PET than precipitation, as reported by Lekula and Lubczynski, (2019).

Evaporation and AVE of the lake were also retrieved from RS to prepare input data for the lake (LAK) package. The DATUTDUT model was able to estimate the evaporation of LX using the water surface temperature input data from MODIS. The AVE of LX was also developed by combining a different source of RS data (Landsat 5, 7 and 8 and ALOS PALSAR DEM), which was used to calculate the historical lake property records as an input for the LAK package in IHM.

As a result, the RS was useful for developing an IHM where there is a scarcity of finding spatio-temporal in-situ measurements.

5.3. Water resources in Boteti River sub-Basin

The Boteti River sub-Basin (BRB) extends across the arid and semi-arid climatic regions where the annual evapotranspiration is much higher than the annual precipitation. Closing the water balance of the study area requires a deep understanding of the water resources of BRB. Applying for that, an integrated hydrological model (IHM), enabled to close the BRB's water balance. This study used remote sensing-based data sets with hydrological and hydrogeological in-situ data to develop a realistic IHM of BRB, which quantitatively assessed the water resource of BRB.

The steady-state model calibration was performed to match the simulated variables (10-year mean groundwater heads and 10-year mean stream discharges) with observed variables; however, there is some discrepancy between the simulated and observed variables. The possible causes of head discrepancy might be due to: 1) errors in model parametrization, 2) errors in the conceptual model, 3) uncertainty in observation of groundwater head measurements, and 4) limitation in DEM spatial resolution to represent the actual elevation (e.g., ALOS PALSAR ± 12.5 m). The developed steady-state model could not provide a good match between observed and simulated stream discharge. The main reasons are 1) inaccuracy in the stream discharge measurement, 2) data gap in stream discharge recording, and 3) error in conceptualization and parametrizing of the model.

The entire water balance of the model showed that the inflow to the basin is mainly from precipitation (69.87%) and lateral groundwater inflow (27.68%), with a small contribution of stream inflow to the system (2.45%). In contrast, the main outflows are groundwater evapotranspiration (85%), later outflow to lateral groundwater outflow (12.92%), with a small contribution from interception (1.69%) and lake evaporation (0.39%).

The 10-year average annual net recharge (R_n) estimated by the steady-state model was -91.79 mm yr⁻¹. The negative value of R_n characterizes the basin climate as an arid climate condition. Since the groundwater evapotranspiration and exfiltration took almost 85% of all the incoming water, the net recharge results in a negative value. The spatial distribution of the R_n map indicated in Figure 4-26 depends on the spatial distribution of R_g , Exf_{gw} and ET_g . The positive R_n (Recharge areas) are mainly found in areas with high rainfall, while the negative R_n values are located in shallow groundwater (Figure 4-23) and low rainfall areas (Figure 4-16). Moreover, comparing the 10-year average precipitation (P) with average potential evapotranspiration (PET) by subtracting P from PET, as shown in Figure 5-1, the PET demand is very high, which restricts gross R_g resulting in a negative annual value of R_n .

The BRB also receives groundwater lateral groundwater inflow (Q_{Lin}) from the neighbouring areas, which amounts to 146.28 mm yr⁻¹. The study area's main incoming flow directions are from the western boundary (RCH), across the Thamalakane Riverside (CHD), and southwest (GHB) boundaries, with estimated percentage inflows of 91.76%, 7.76%, and 0.48%, respectively. At the same time, the total lateral groundwater outflow (Q_{Lout}) from the system consists of 67.55 mm yr⁻¹, which is composed of 19.68% in the south-eastern (DRN) boundary, 45.45% southwest (GHB) boundary, and 39.87% in the northwest (CHD) boundary.

The steady-state model also simulated the amount of surface water bodies (i.e., BR and LX) discharged to groundwater and recharged from groundwater quantitatively, and it was found that the hypotheses made in section 1.4.5 were found to be true. The net leakage to groundwater of BR is positive ($q_{sg} - q_{gs} > 0$), meaning that the BR discharges (leakes) to surface water to groundwater of BRB. Likewise, the net leakage groundwater of LX ($L_{LKnet} = L_{LKin} - L_{LKout}$) is positive. Table 4-6, which indicates, that aquifer gains water from

the LX. Table 4-6 also shows that the total inflow of LX is highly dependent on BR (62.58%) flow and precipitation (37.24%). In contrast, the main outflow of the lake is by lake evaporation (prove of the hypothesis made in section 1.4.5), which is 60% of the total outflow while the remaining 40% seeps to groundwater.

Analysing the lakebed seepage enables quantifying the leakage between the lake and groundwater. In this study, the lakebed seepage components, including the lake leakage to groundwater ($L_{L,kin}$), the groundwater leakage into the lake ($L_{L,Kout}$) and the net leakage ($L_{L,knet}=L_{L,kin}-L_{L,Kout}$), were used to identify the lake characteristics as used by El-Zehairy et al. (2018). The $L_{L,kin}$ ranges from 0.01 to 2.7 mm day⁻¹. The $L_{L,Kout}$ is zero, which results in the $L_{L,knet}$ range between 0.01 to 2.7 mm day⁻¹, which indicates that the lake is losing water to the underlying aquifer. The lakebed leakance is the main parameter that controls the lake's interaction with groundwater. The leakance of Lake Xau ranges (0.05 - 0.1 day⁻¹), which is higher compared to the artificial lake leakance of Lake Turawa (0.0007-0.0015 day⁻¹) (El-Zehairy et al., 2018), which is understandable because the Lake Turawa is the artificial reservoir with thick (~2-4m) compacted anthropogenic sediment. Compared to the natural lake leakance of Viridi et al. (2013) 0.059 – 0.077 day⁻¹ and Hampen et al. (2011) 0.26 day⁻¹, with LX leakance (0.05 -0.1 day⁻¹) strongly agrees with natural lake leakance range.

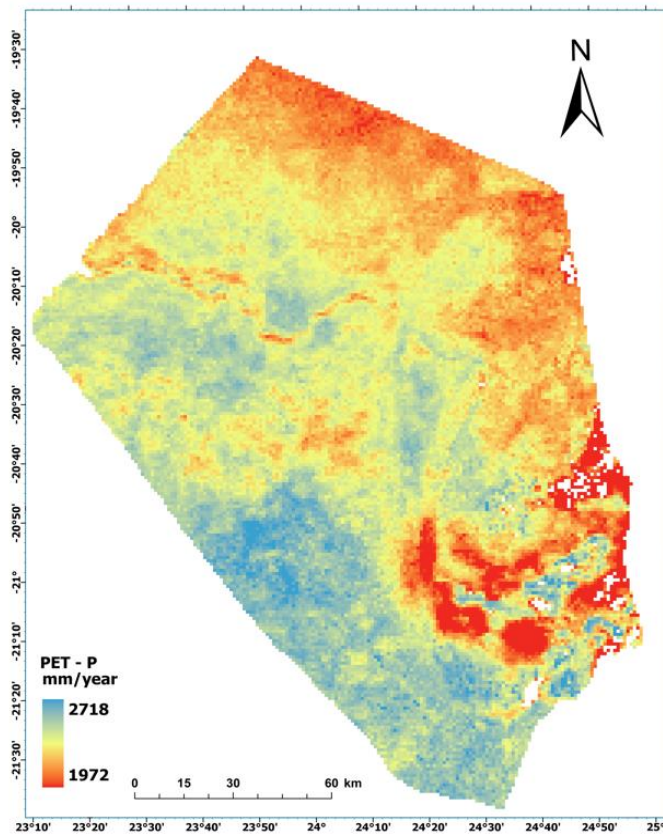


Figure 5-1 Spatial distribution of PET- P map of BRB

6. CONCLUSION AND RECOMMENDATION

6.1. Conclusion

In order to evaluate the water resources of the Boteti River sub-Basin (BRB), this study created an integrated hydrological model (IHM). Remote sensing (RS), as well as in-situ hydrological and hydrogeological data, were used to develop a steady-state IHM of BRB using data of ten hydrological years (1st October 2010 to 30th September 2020). The key conclusions of this study are outlined below.

- ❖ Developing a hydrogeological conceptual model (HCM) is vital for developing a multi-layered conceptual model of BRB. The result of BRB identified the three hydrostratigraphic units (KSU aquifer, SBA aquitard and LA+EA aquifer), to be used in the IHM
- ❖ By developing RS-based time series analysis of LX area, volume, elevation, and evaporation, it was possible to prepare an input data set for developing a representative model which can simulate the lake water balance.
- ❖ The property of surface water and groundwater (SW-GW) interaction was identified by steady-state IHM, where both Boteti River (BR) and Lake Xau (LX) were positively interacting with groundwater. The average annual river BR leakage to groundwater is 21.97 mm yr⁻¹ and the groundwater leakage to BR is 10.34 mm yr⁻¹. Whereas the LX leakage to groundwater is 1.43 mm yr⁻¹, there is no groundwater leakage to LX.
- ❖ The simulated steady-state model generally produced groundwater distribution heads with MAE and RMSE values of 0.77 m and 0.96 m, respectively.
- ❖ The total gross recharge and lateral groundwater inflow account for 67.53 % and 27.98% of the total inflow to the system, respectively. Stream and lake leakage to the groundwater accounts for 4.2% and 0.29% of the total inflow to the system, respectively. At the same time, groundwater evapotranspiration and exfiltration account for 61.44% and 23.65% of the total outflow. The lateral groundwater outflow and groundwater leakage to stream account for 12.92% and 1.99% of the total outflow, respectively.
- ❖ The entire water balance of BRB has different components; the percentage of each component is described as a total inflow (528.10 mm yr⁻¹); precipitation (P) 69.87%, stream inflow (q_{in}) 2.44%, lateral groundwater inflow (Q_{Lin}) 27.58%. Whereas the outflows are described as a percentage of total outflow (523.31 mm yr⁻¹); groundwater evapotranspiration (ET_g) 84.98 %, lateral groundwater outflow (Q_{Lout}) 12.91%, interception loss (E_i) 1.72%, and lake evaporation (E_{LK}) 0.39%.
- ❖ The findings of the sensitivity analysis showed that the model was less sensitive to changes of stream bed hydraulic conductivity and lake bed leakance than to changes of horizontal hydraulic conductivity.

6.2. Recommendations

- ❖ This study used multiple remote sensing (RS) products to develop IHM. These products need to be calibrated and validated with insitu measurements
- ❖ Groundwater heads need to be adjusted with the field piezometric measurements of the water table and corresponding altitudes; the latter should be done with high precision (+/- 2cm) GPS; the same way also Boteti river stages should be defined to define river gradient and flow rates
- ❖ Install two adjacent piezometers in the center of the Lake Xau, one for shallow groundwater and the other open to the surface water inflow, survey altitudes of both and in both install automated water level recorders
- ❖ The northwestern boundary of the study area nearby the Thamalakane River should be examined in the field but also in the model using different boundary conditions because the current model was inclined to loose groundwater instead of gaining from Okavango Delta
- ❖ Run transient IHM; transient models are more reliable than steady state; unfortunately due to time limitation, the transient model was not completed therefore is not part of this document

LIST OF REFERENCES

- Adamowski, K., Feluch, W., 2011. Application of nonparametric regression to groundwater level prediction. <https://doi.org/10.1139/L91-073> 18, 600–606. <https://doi.org/10.1139/L91-073>
- Anderson, M.P., Woessner William W., Hunt, R.J., 2015. Applied Groundwater Modeling Simulation of Flow and Advective Transport, Elsevier. <https://doi.org/10.1016/C2009-0-21563-7>
- Anibas, C., Buis, K., Verhoeven, R., Meire, P., Batelaan, O., 2011. A simple thermal mapping method for seasonal spatial patterns of groundwater-surface water interaction. *Journal of Hydrology* 397, 93–104. <https://doi.org/10.1016/j.jhydrol.2010.11.036>
- Bastiaanssen, W.G.M., Menenti, M., Feddes, R.A., Holtslag, A.A.M., 1998. A remote sensing surface energy balance algorithm for land (SEBAL). 1. Formulation. *Journal of Hydrology* 212–213, 198–212. [https://doi.org/10.1016/S0022-1694\(98\)00253-4](https://doi.org/10.1016/S0022-1694(98)00253-4)
- Bastiaanssen, W.G.M., Noordman, E.J.M., Pelgrum, H., Davids, G., Thoreson, B.P., Allen, R.G., 2005. SEBAL Model with Remotely Sensed Data to Improve Water-Resources Management under Actual Field Conditions. *Journal of Irrigation and Drainage Engineering* 131, 85–93. [https://doi.org/10.1061/\(ASCE\)0733-9437\(2005\)131:1\(85\)](https://doi.org/10.1061/(ASCE)0733-9437(2005)131:1(85))
- Breyer, J., 1983. Soils in the Lower Boteti Region, Central District, Republic of Botswana. National Institute of Development Research and Documentation, University of Botswana.
- Brooks, R.H., Corey, A.T., 1966. Properties of Porous Media Affecting Fluid Flow. *Journal of the Irrigation and Drainage Division* 92, 61–88. <https://doi.org/10.1061/JRCEA4.0000425>
- Burrige, D.M., A.J.Gadd, 1974. The Meteorological Office operational 10-level numerical weather prediction model (December 1974). *British Meteorological Office* 57.
- Carney, J.N., Aldiss, D.T., Lock, N.P., 1994. The Geology of Botswana. Director of Geological Survey Department 1–119.
- Daoud, M.G., Lubczynski, M.W., Vekerdy, Z., Francés, A.P., 2022. Application of a novel cascade-routing and reinfiltration concept with a Voronoi unstructured grid in MODFLOW 6, for an assessment of surface-water/groundwater interactions in a hard-rock catchment (Sardon, Spain). *Hydrogeology Journal* 30, 899–925. <https://doi.org/10.1007/s10040-021-02430-z>
- de Wit, P., Nachtergaele, F., 1990. Soil Map of the Republic of Botswana. Soil Mapping and Advisory Services Project FAO/BOT/85/011. Map 2 of 2. - ESDAC - European Commission.
- El-Zehairy, A.A., Lubczynski, M.W., Gurwin, J., 2018. Interactions of artificial lakes with groundwater applying an integrated MODFLOW solution. *Hydrogeology Journal* 26, 109–132. <https://doi.org/10.1007/s10040-017-1641-x>
- Esri, 2020. Esri 2020 Land Cover-overview [WWW Document]. Esri Inc. URL https://tiledimageservices.arcgis.com//services/Esri_2020_Land_Cover_V2/ImageServer (accessed 5.14.22).
- FAO, 2020. WaPOR database methodology. FAO 2, 1–90. <https://doi.org/10.4060/CA9894EN>
- Farquharson F.A.K., Gash J.H.C., Roberts J.M., 1990. Report on a review of evaporation estimation for the Okavango Delta. Wallingford.
- Funk, C., Peterson, P., Landsfeld, M., Pedreros, D., Verdin, J., Shukla, S., Husak, G., Rowland, J., Harrison, L., Hoell, A., Michaelsen, J., 2015. The climate hazards infrared precipitation with stations—a new environmental record for monitoring extremes. *Scientific Data* 2015 2:1 2, 1–21. <https://doi.org/10.1038/sdata.2015.66>
- Gao, H., Birkett, C., Lettenmaier, D.P., 2012. Global monitoring of large reservoir storage from satellite remote sensing. *Water Resources Research* 48. <https://doi.org/10.1029/2012WR012063>

- Gash, J.H.C., 1979. An analytical model of rainfall interception by forests. *Quarterly Journal of the Royal Meteorological Society* 105, 43–55. <https://doi.org/10.1002/qj.49710544304>
- Guerink, J., Trout, K., Ross, M.A., 2006. Introduction to the Integrated Hydrological Model(IHM). Federal Interagency Hydrologic Modeling Conference 1–8.
- Hampen, L., Denmark, W., Engesgaard, P., Looms, M., Kidmose, J., Nilsson, B., Laier, T., Kidmose, Jacob, Engesgaard Bertel Nilsson Troels Laier Majken Looms, P.C., 2011. Spatial Distribution of Seepage at a Flow-Through Lake: Lake Hampen, Western Denmark. *Vadose Zone Journal* 10, 110–124. <https://doi.org/10.2136/VZJ2010.0017>
- Hassan, S.M.T., Lubczynski, M.W., Niswonger, R.G., Su, Z., 2014. Surface-groundwater interactions in hard rocks in Sardon Catchment of western Spain: An integrated modeling approach. *Journal of Hydrology* 517, 390–410. <https://doi.org/10.1016/j.jhydrol.2014.05.026>
- Heyns Hubert HG Savenije and Arjen, 2009. Water conservation in arid and semi-arid regions. *eolss.net* 1–37.
- Howard S., W., Simon A., M., Xin Li, 2010. Groundwater modelling arid and semi-arid areas, Hydrology, hydrogeology and water resources Cambridge University Press.
- Langevin, C.D., Hughes, J.D., Banta, E.R., Niswonger, R.G., Panday, S., Provost, A.M., 2017. Documentation for the MODFLOW 6 Groundwater Flow Model . U.S. Geological Survey Techniques and Methods book 6-chap.A55,197P.
- Langevin, C.D., Provost, A.M., Panday, S., Hughes, J.D., 2022. Documentation for the MODFLOW 6 Groundwater Transport Model. Techniques and Methods. <https://doi.org/10.3133/TM6A61>
- le Maitre, D.C., Scott, D., Colvin, C., 1999. Review of information on interactions between vegetation and groundwater. *water Research Commission* 25, 137–152.
- Lekula, M., Lubczynski, M.W., 2019. Use of remote sensing and long-term in-situ time-series data in an integrated hydrological model of the Central Kalahari Basin, Southern Africa. *Hydrogeology Journal* 27, 1541–1562. <https://doi.org/10.1007/S10040-019-01954-9/FIGURES/11>
- Lekula, M., Lubczynski, M.W., Shemang, E.M., 2018. Hydrogeological conceptual model of large and complex sedimentary aquifer systems – Central Kalahari Basin. *Physics and Chemistry of the Earth* 106, 47–62. <https://doi.org/10.1016/j.pce.2018.05.006>
- Li, Y., Gao, H., Allen, G.H., Zhang, Z., 2021. Constructing reservoir area-volume-elevation curve from TanDEM-X DEM data. *IEEE Journal of Selected Topics in Applied Earth Observations and Remote Sensing* 14, 2249–2257. <https://doi.org/10.1109/JSTARS.2021.3051103>
- Li, Y., Gao, H., Jasinski, M.F., Zhang, S., Stoll, J.D., 2019. Deriving high-resolution reservoir bathymetry from ICESat-2 prototype photon-counting lidar and landsat imagery. *IEEE Transactions on Geoscience and Remote Sensing* 57, 7883–7893. <https://doi.org/10.1109/TGRS.2019.2917012>
- Linn, F., Masie, M., Rana, A., 2003. The impacts on groundwater development on shallow aquifers in the lower Okavango Delta, Northwestern Botswana. *Environmental Geology* 44, 112–118. <https://doi.org/10.1007/s00254-002-0706-9>
- McCarthy, T.S., 2006. Groundwater in the wetlands of the Okavango Delta, Botswana, and its contribution to the structure and function of the ecosystem. *Journal of Hydrology* 320, 264–282. <https://doi.org/10.1016/J.JHYDROL.2005.07.045>
- McDonald, M.G., Harbaugh, A.W., 1988. A modular three-dimensional finite-difference ground-water flow model. *Techniques of Water-Resources Investigations*. <https://doi.org/10.3133/TWRI06A1>
- Merriam, R.A., 1960. A note on the interception loss equation. *Journal of Geophysical Research* 65, 3850–3851. <https://doi.org/10.1029/JZ065I011P03850>

- Merritt, M.L., Konikow, L.F., 2000. Documentation of a computer program to simulate lake-aquifer interaction using the MODFLOW ground water flow model and the MOC3D solute-transport model. Water-Resources Investigations Report. <https://doi.org/10.3133/WRI004167>
- Mitiku, A., 2019. Integrated hydrological modelling of river-groundwater interactions in the Boteti River Area, Botswana. University of Twente 72.
- Modie, L.T., Kenabatho, P.K., Stephens, M., Mosekiemang, T., 2022. Investigating groundwater and surface water interactions using stable isotopes and hydrochemistry in the Notwane River Catchment, South East Botswana. *Journal of Hydrology: Regional Studies* 40, 101014. <https://doi.org/10.1016/J.EJRH.2022.101014>
- Mokgedi, L., Nobert, J., Munishi, S., 2019. Assessment of lake surface dynamics using satellite imagery and in-situ data; case of Lake Ngami in North-West Botswana. *Physics and Chemistry of the Earth, Parts A/B/C* 112, 175–186. <https://doi.org/10.1016/J.PCE.2018.12.008>
- Mphinyane, W.N., Akanyang, L.K., Mulale, K., Deventer, F. van, Magole, L., Perkins, J.S., Sebege, R.J., Athlapheng, J.R., Chanda, R., 2018. Firewood Utilisation and Its Implication on Trees around Mopipi Village in Boteti Sub-District of Botswana. *Asian Journal of Environment & Ecology* 7, 1–10. <https://doi.org/10.9734/AJEE/2018/42471>
- Nelms, D.L., Jr., G.E.H., Hayes, D.C., 1995. Base-flow characteristics of streams in the Valley and Ridge, Blue Ridge, and Piedmont physiographic provinces of Virginia. Open-File Report. <https://doi.org/10.3133/OFR95298>
- Newman, B.D., Vivoni, E.R., Groffman, A.R., 2006. Surface water-groundwater interactions in semiarid drainages of the American southwest. *Hydrological Processes* 20, 3371–3394. <https://doi.org/10.1002/HYP.6336>
- Nicholson, S.E., Farrar, T.J., 1994. The influence of soil type on the relationships between NDVI, rainfall, and soil moisture in semiarid Botswana. I. NDVI response to rainfall. *Remote Sensing of Environment* 50, 107–120. [https://doi.org/10.1016/0034-4257\(94\)90038-8](https://doi.org/10.1016/0034-4257(94)90038-8)
- Obakeng O.T., de Vries J.J., Lubczynski M.W., 2007. Soil moisture dynamics and evapotranspiration at the fringe of the Botswana Kalahari, with emphasis on deep rooting vegetation. (PhD). Vrije Universiteit Amsterdam, Amsterdam. accessed from <http://www.itc.utwente.nl/library/papers/2007/phd/obakeng.pdf>.
- Pekel, J.F., Cottam, A., Gorelick, N., Belward, A.S., 2016. High-resolution mapping of global surface water and its long-term changes. *Nature* 540, 418–422. <https://doi.org/10.1038/NATURE20584>
- Penman, H.L., 1948. Natural evaporation from open water, bare soil and grass. *Proceedings of the Royal Society of London. Series A. Mathematical and Physical Sciences* 193, 120–145. <https://doi.org/10.1098/RSPA.1948.0037>
- Rahm, D., Swatuk, L., Matheny, E., 2006. Water Resource Management in Botswana: Balancing Sustainability and Economic Development*. *Environment, Development and Sustainability* 2006 8:1 8, 157–183. <https://doi.org/10.1007/S10668-005-2491-6>
- Roussouw, N., Bird, M.S., Perissinotto, R., 2018. Microalgal biomass and composition of surface waterbodies in a semi-arid region earmarked for shale gas exploration (Eastern Cape Karoo, South Africa). *Limnologica* 72, 44–56. <https://doi.org/10.1016/J.LIMNO.2018.03.003>
- Sattel, D., Kgotlhang, L., 2003. Groundwater exploration with AEM in the Boteti Area, Botswana. ASEG Extended Abstracts 2003, 1–5. <https://doi.org/10.1071/ASEG2003AB155>
- Scaramuzza, P., Micijevic, E., Gyanesh, C., 2019. SLC Gap-Fill Methodology. USGS Landsat Mission 1–5.
- Seaber, P.R., 1988. Hydrostratigraphic units. *Hydrogeology* 9–14. <https://doi.org/10.1130/DNAG-GNA-O2.9>

- Sebege, R.J., Athlopheng, J.R., Chanda, R., Mulale, K., Mphinyane, W., 2017. Land use intensification and implications on land degradation in the Boteti area: Botswana. *African Geographical Review* 38, 32–47. <https://doi.org/10.1080/19376812.2017.1284599>
- Senay, G.B., Budde, M., Verdin, J.P., Melesse, A.M., 2007. A Coupled Remote Sensing and Simplified Surface Energy Balance Approach to Estimate Actual Evapotranspiration from Irrigated Fields. *Sensors* 2007, Vol. 7, Pages 979-1000 7, 979–1000. <https://doi.org/10.3390/S7060979>
- Smith, R.A., 1984. The lithostratigraphy of the Karoo Supergroup in Botswana. Department of Geological Survey.
- Sophocleous, M., 2002. Interactions between groundwater and surface water: The state of the science. *Hydrogeology Journal* 10, 52–67. <https://doi.org/10.1007/s10040-001-0170-8>
- Spanoudaki, K., Stamou, A.I., Nanou-Giannarou, A., 2009. Development and verification of a 3-D integrated surface water–groundwater model. *Journal of Hydrology* 375, 410–427. <https://doi.org/10.1016/J.JHYDROL.2009.06.041>
- Swatuk, L.A., Motsholapheko, M., 2008. Communicating integrated water resources management: From global discourse to local practice – Chronicling an experience from the Boteti River sub-Basin, Botswana. Elsevier, *Physics and Chemistry of the Earth* 881–888.
- Timmermans, W.J., Kustas, W.P., Andreu, A., 2016. Utility of an Automated Thermal-Based Approach for Monitoring Evapotranspiration. *Acta Geophysica* 2015 63:6 63, 1571–1608. <https://doi.org/10.1515/ACGEO-2015-0016>
- Todd, R.W., Evett, S.R., Howell, T.A., 2000. The Bowen ratio-energy balance method for estimating latent heat flux of irrigated alfalfa evaluated in a semi-arid, advective environment. *Agricultural and Forest Meteorology* 103, 335–348. [https://doi.org/10.1016/S0168-1923\(00\)00139-8](https://doi.org/10.1016/S0168-1923(00)00139-8)
- Trabelsi, F., Tarhouni, J., Mammou, A. ben, Ranieri, G., 2013. GIS-based subsurface databases and 3-D geological modeling as a tool for the set up of hydrogeological framework: Nabeul-Hammamet coastal aquifer case study (Northeast Tunisia). *Environmental Earth Sciences* 70, 2087–2105. <https://doi.org/10.1007/S12665-011-1416-Y>
- Vanderpost, C., 1995. Population change and environmental problems in the Mid-Boteti region of Botswana. *GeoJournal* 1995 35:4 35, 521–529. <https://doi.org/10.1007/BF00824368>
- VanderPost, C., McFarlane, M., 2007. Groundwater investigation in semi-arid developing countries, using simple GIS tools to facilitate interdisciplinary decision making under poorly mapped conditions: The Boteti area of the Kalahari region in Botswana. *International Journal of Applied Earth Observation and Geoinformation* 9, 343–359. <https://doi.org/10.1016/J.JAG.2006.11.002>
- Villa Nova, N.A., de Miranda, J.H., Pereira, A.B., da Silva, K.O., 2006. Estimation of the potential evapotranspiration by a simplified Penman method. *Engenharia Agrícola* 26, 713–721. <https://doi.org/10.1590/S0100-69162006000300007>
- Virdi, M.L., Lee, T.M., Swancar, A., Niswonger, R.G., 2013. Simulating the Effect of Climate Extremes on Groundwater Flow Through a Lakebed. *Groundwater* 51, 203–218. <https://doi.org/10.1111/J.1745-6584.2012.00969.X>
- Wan, Z., 2013. Collection-6 MODIS Land Surface Temperature Products Users' Guide.
- Water Surveys Botswana (Pty) Ltd, 2006. Groundwater Resources Investigation in the Boteti River Area, REPUBLIC OF BOTSWANA Ministry of Minerals , Energy & Water Resources Department of Water Affairs.
- Weare, P.R., Yalala, A., 1971. Provisional Vegetation Map of Botswana. Botswana Society. accessed from <http://www.jstor.org/stable/40979284> .
- Winter, T.C., 1995. Recent advances in understanding the interaction of groundwater and surface water. *Reviews of Geophysics* 33, 985–994. <https://doi.org/10.1029/95RG00115>

- Winter, T.C., Harvey, J.W., Franke, O.L., Alley, W.M., 1998. Ground Water and Surface Water - A single Resource - U.S. Geological Survey Circular 1139. USGS Publications Circular 1, 79.
- Woessner, W.W., 2000. Stream and fluvial plain ground water interactions: Rescaling hydrogeologic thought. *Ground Water* 38, 423–429. <https://doi.org/10.1111/J.1745-6584.2000.TB00228.X>
- Yang, J., Yu, Z., Yi, P., Frappe, S.K., Gong, M., Zhang, Y., 2020. Evaluation of surface water and groundwater interactions in the upstream of Kui river and Yunlong lake, Xuzhou, China. *Journal of Hydrology* 583, 124549. <https://doi.org/10.1016/j.jhydrol.2020.124549>
- Yue, H., Liu, Y., 2019. Variations in the lake area, water level, and water volume of Hongjiannao Lake during 1986–2018 based on Landsat and ASTER GDEM data. *Environmental Monitoring and Assessment* 191. <https://doi.org/10.1007/s10661-019-7715-6>
- Zhao, G., Gao, H., Cai, X., 2020. Estimating lake temperature profile and evaporation losses by leveraging MODIS LST data. *Remote Sensing of Environment* 251, 112104. <https://doi.org/10.1016/J.RSE.2020.112104>

APPENDICES

Appendix 1

GEE script for obtaining the monthly history of LX

```

var datasurface = ee.ImageCollection("JRC/GSW1_3/MonthlyHistory")
    .filterDate('2010-10-1', '2020-10-18').filterBounds(AOI);

// get the size of the collection and cast collection to a list
var length = datasurface.size();
var list = datasurface.toList(length);

// run a for loop to export images
for (var i = 1; i < 61; i++){
  var image = ee.Image(list.get(i));
  var name1 = 'Monthwater' + i;
  print(name1)
  Export.image.toDrive({
    image: image,
    description: name1,
    scale: 250,
    maxPixels: 1e13,
    region: AOI
  });
}

```

Appendix 2

Python script for AVE curve calculation

Created on Thu Jan 27 11:55:44 2022

@Author: Wondimagegn Abebe Demissie(S2446588)

#Import required libraries

import rasterio

import numpy as np

import pandas as pd

import matplotlib.pyplot as plt

from mpl_toolkits.axes_grid1 import make_axes_locatable

Open Raster

lakeRst = rasterio.open('D:\Lake_Xau\WAM\WAM26.tif')

lakeRst.count

Raster resolution

lakeRst.res

#all raster crs info

lakeRst.crs.wkt

Get Raster values as Numpy

lakeBottom = lakeRst.read(1)

```

# raster sample
lake Bottom[12:491272455081228,12:491272455081228]
# Replace value for np.nan
noDatavalue = np.copy(lakeBottom[0,0])
lakeBottom[lakeBottom==noDatavalue] = np.nan
# Plot raster
plt.figure(figsize=(12,12))
plt.imshow(lakeBottom)
plt.show()
# Lake Volume Calculation
# get raster minimum and maximum
minElev = np.nanmin(lakeBottom)
maxElev = np.nanmax(lakeBottom)
print('Min bottom elevation %.2f m., max bottom elevation %.2f m.%(minElev,maxElev))
# steps for calculation
nSteps = 16
# lake bottom elevation intervals
elevSteps = np.round(np.linspace(minElev,maxElev,nSteps),0)
elevSteps
# definition of volume function
def calculateVol(elevStep,elevDem,lakeRst):
    tempDem = elevStep - elevDem[elevDem<elevStep]
    tempVol = tempDem.sum()*lakeRst.res[0]*lakeRst.res[1]
    return tempVol
# calculate volumes for each elevation
volArray = []
for elev in elevSteps:
    tempVol = calculateVol(elev,lakeBottom,lakeRst)
    volArray.append(tempVol)
# print output
print("Lake bottom elevations %s"%elevSteps)
volArrayMCM = [round(i/1000000,2) for i in volArray]
print("Lake volume in million of cubic meters %s"%volArrayMCM)
# plot values
fig, ax = plt.subplots(figsize=(12,5))
ax.plot(volArrayMCM,elevSteps,label='lake Xau(LX)')
ax.grid()
ax.legend()
ax.set_xlabel('Volume MCM')
ax.set_ylabel('Elevation (masl)')
plt.show()
# plot values
fig, [ax1, ax2] = plt.subplots(1,2,figsize=(20,8),gridspec_kw={'width_ratios': [2, 1]})
ax1.set_title('Lake bottom elevation')
botElev = ax1.imshow(lakeBottom)
divider = make_axes_locatable(ax1)
cax = divider.append_axes('bottom', size='5%', pad=0.5)
fig.colorbar(botElev, cax=cax, orientation='horizontal', label='Elevation (masl)')
ax2.plot(volArrayMCM,elevSteps,label='Lake Xau(LX)')
ax2.grid()

```

```

ax2.legend()
ax2.set_xlabel('Volume MCM')
ax2.set_ylabel('Elevation (masl)')
plt.show()
#definig AVE curve data
df=pd.read_csv("D:\Lake_Xau\WAM\AVE26(Maximum_LX).csv")
df.head()
# plotting AVE curve
fig, ax1 = plt.subplots(figsize=(10,6))
ax1.plot(df['Volume (MCM)'], df['Level (m)'],color="orange")
ax1.set_title('AVE Curve for LX in September 2012')
ax1.set_xlabel('Volume (MCM)')
ax1.set_ylabel('Elevation (m)')
ax1.grid()
ax2 = ax1.twinx()
ax2.plot(df['Area (ha)'], df['Level (m)'])
ax2.set_xlabel('Area (ha)')
plt.gca().invert_xaxis()
plt.show()
plt.legend()

```

Appendix 3

DATTUDAT ILWIS script for calculating lake evaporation

Source: (Timmermans et al., 2016)

```

// begincomment

lati%1 {dom=VALUE.dom;vr=-
180.0000:180.0000:0.00001}:=iff(LST_Day_1km_doy%1_u,crdy(transform(mapcrd(LST_Day_1km_doy%1_u),latlo
n)),0)
long%1 {dom=VALUE.dom;vr=-
180.0000:180.0000:0.00001}:=iff(LST_Day_1km_doy%1_u,crdx(transform(mapcrd(LST_Day_1km_doy%1_u),latlo
n)),0)
// endcomment
om%1ega {dom=VALUE.dom;vr=-180.00000:180.00000:0.00001}:=((12-((%2)+long%1/15+et(da(%1))/60))*15
co%1zen {dom=VALUE.dom;vr=-
1.0000:1.0000:0.00001}:=sin(de(da(%1))/57.29577951)*sin(lati%1/57.29577951)+cos(de(da(%1))/57.29577951)*cos
(lati%1/57.29577951)*cos(om%1ega/57.29577951)
ir%1toa {dom=VALUE.dom;vr=-500000.0000:500000.0000:0.00001}:=1367*eo(da(%1))*co%1zen
// Calculati%1on of the net radiation albedo map - instantaneous
// r%1n.mpr {dom=VALUE.dom;vr=-5000.00000:5000.00000:0.00001}:= 0.85*0.75*ir%1toa+0.8*5.6697E-
8*(mapmin(LST_Day_1km_doy%1_u.mpr))^4-0.95*5.6697E-8*(LST_Day_1km_doy%1_u)^4
r%1n.mpr {dom=VALUE.dom;vr=-5000.00000:5000.00000:0.00001}:= (1-(0.05+(LST_Day_1km_doy%1_u-
mapmin(LST_Day_1km_doy%1_u.mpr))/(mapmax(LST_Day_1km_doy%1_u.mpr)-
mapmin(LST_Day_1km_doy%1_u.mpr))*0.2))*0.7*ir%1toa+0.8*5.6697E-
8*(mapmin(LST_Day_1km_doy%1_u.mpr))^4-1.0*5.6697E-8*(LST_Day_1km_doy%1_u)^4

// Calculati%1on of the soil heat flux map - instantaneous
g%1s.mpr {dom=VALUE.dom;vr=-5000.00000:5000.00000:0.00001}:= (0.05+(LST_Day_1km_doy%1_u-
mapmin(LST_Day_1km_doy%1_u.mpr))/(mapmax(LST_Day_1km_doy%1_u.mpr)-
mapmin(LST_Day_1km_doy%1_u.mpr))*0.4)*r%1n

```

```
// Calculation of turbulent fluxes
h%1:=iff(LST_Day_1km_doy%1_u<mapmin(LST_Day_1km_doy%1_u.mpr),0,iff(LST_Day_1km_doy%1_u>map
max(LST_Day_1km_doy%1_u.mpr),r%1n-g%1s,(r%1n-g%1s)*(LST_Day_1km_doy%1_u-
(mapmin(LST_Day_1km_doy%1_u.mpr)))/(mapmax(LST_Day_1km_doy%1_u.mpr)-
mapmin(LST_Day_1km_doy%1_u.mpr))))
le%1:=r%1n-g%1s-h%1

// Daily values:

lambda%1.mpr{dom=VALUE.dom;vr=-1.00000:1.00000:0.00000}:=le%1/(le%1+h%1)

// Calculation of daily totals (assuming n/N equal to 1):
om%1egasr.mpr{dom=VALUE.dom;vr=-180.00000:180.00000:0.00001}:=acos(-
1*tan(lati%1/57.29577951)*tan(de(da%1))/57.29577951))
ir%1toaday.mpr{dom=VALUE.dom;vr=-
5000.00000:5000.00000:0.00001}:=24/3.141592*1367*0.0036*eo(da%1))*cos(lati%1/57.29577951)*cos(de(da%1))
/57.29577951)*(sin(om%1egasr)-om%1egasr*cos(om%1egasr))

qn%1day.mpr{dom=VALUE.dom;vr=-5000.00000:5000.00000:0.00001}:=((0.25+0.5*1)*(1-
1.1*(0.05+(LST_Day_1km_doy%1_u-
mapmin(LST_Day_1km_doy%1_u.mpr))/(mapmax(LST_Day_1km_doy%1_u.mpr)-
mapmin(LST_Day_1km_doy%1_u.mpr))*0.2))*ir%1toaday-110*(0.7)/11.5741
// qn%1daydtd.mpr{dom=VALUE.dom;vr=-5000.00000:5000.00000:0.00001}:=((0.25+0.5*1)*(1-
1.1*ro%1sur)*ir%1toaday-110*(mapmax(LST_Day_1km_doy%1_u.mpr)/ir%1toa)/11.5741

et%1day.mpr{dom=VALUE.dom;vr=-5.00000:50.00000:0.001}:=lambda%1*qn%1day/2.47
```

Appendix 4

Interpolating monthly data to daily data using python script

```
# -*- coding: utf-8 -*-
Created on Tue Jun 29 12:48:23 2021
@author: Wondimagegn Abebe Demissie (S2446588)

import os
import pandas as pd
from scipy.signal import savgol_filter
import numpy as np
root = r'G:\AVE For Lake Xau\120 images of LX'
#root = os.path.join('.')
# 1. import the data
AVE = pd.read_csv('ALL LAKE XAU AVE.csv')
# 2. For linear interpolation
# method can be" (linear, time, index, pad, nearest, krough, from_derivatives)
AVE_linear = AVE.interpolate(method = 'linear', axis = 0) # axis = 0 to work on the column axis
# 3. Smooth the data (after interpolation)
AVE_linear = AVE_linear.drop(columns = ["Date"])
AVE_filtered = savgol_filter(AVE_linear, window_length = 101, polyorder = 3, axis = 0)
AVE_filtered = pd.DataFrame(AVE_filtered, columns = AVE_linear.columns)
# 4. export the output
output1 = root + 'AVE_filled_gap.csv'
output2 = root + 'AVE_filtered.csv'
AVE_linear.to_csv(output1, sep = ',', index = False, float_format = '%.5f')
AVE_filtered.to_csv(output2, sep = ',', index = False, float_format = '%.5f')
```

Appendix 5

Lake evaporation during February 2010

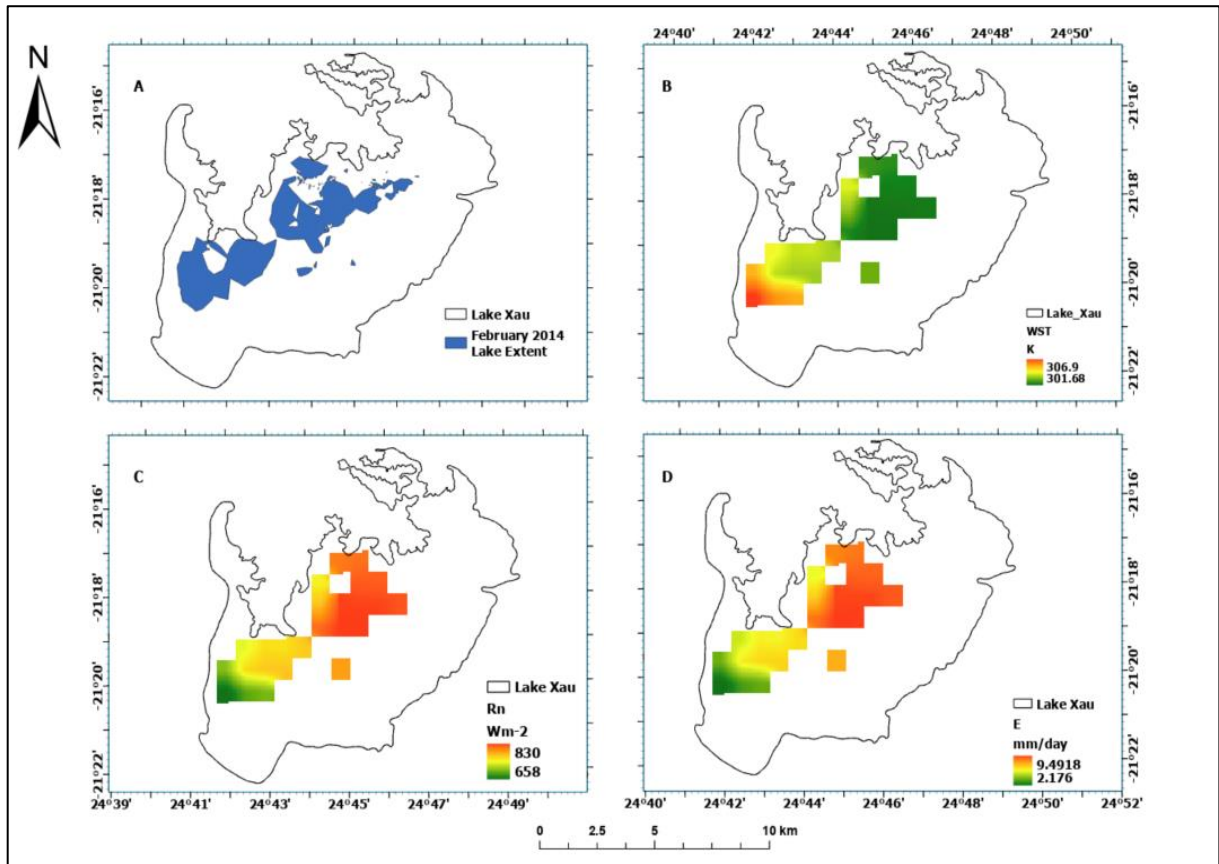


Figure a) Surface area b) water surface temperature (WST) c) net radiation (Rn) d) evaporation rate of LX (E_{LX}) on February 1st, 2014

Figure above shows the instantaneous surface area, WST, net radiation, and daily evaporation of LX on 1st February 2014. On this day, the estimated surface area is 12.85 km², with a WST range of 306.90 to 301.68 K, as shown in Figure (a) and (b), respectively. The net radiation is calculated using Equation 3-11, and it ranges between 830 to 658 Wm^{-2} , as shown in Figure (c). The evaporation rates range between 9.49 to 2.17 $mm\ day^{-1}$ Figure (d).

Appendix 6

Effective precipitation ($P_e = P - E_I$)

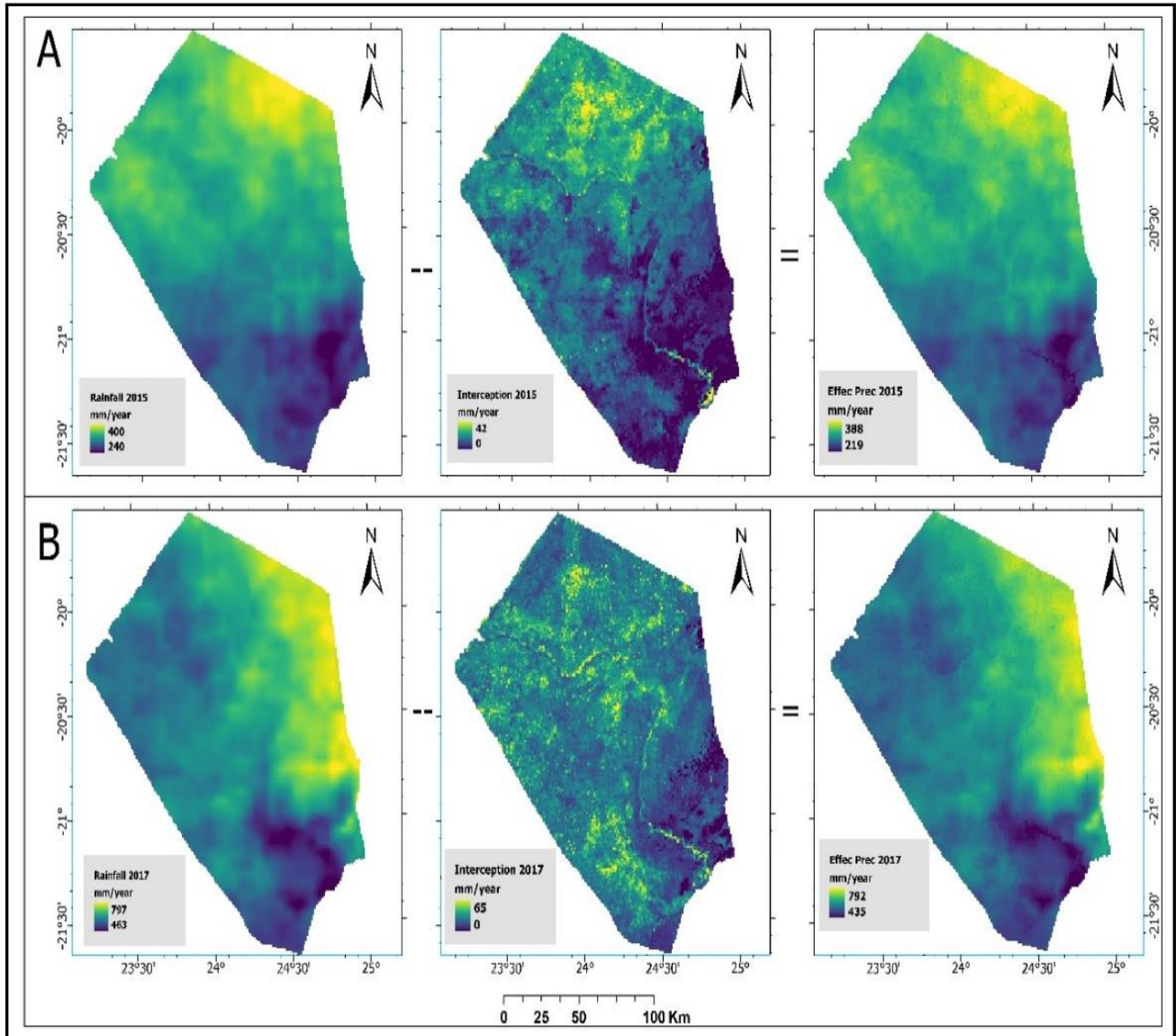


Figure Effective precipitation calculation ($P_e = P - E_I$) a) dry year of 2015 b) wet year of 2017 units (mm yr^{-1})